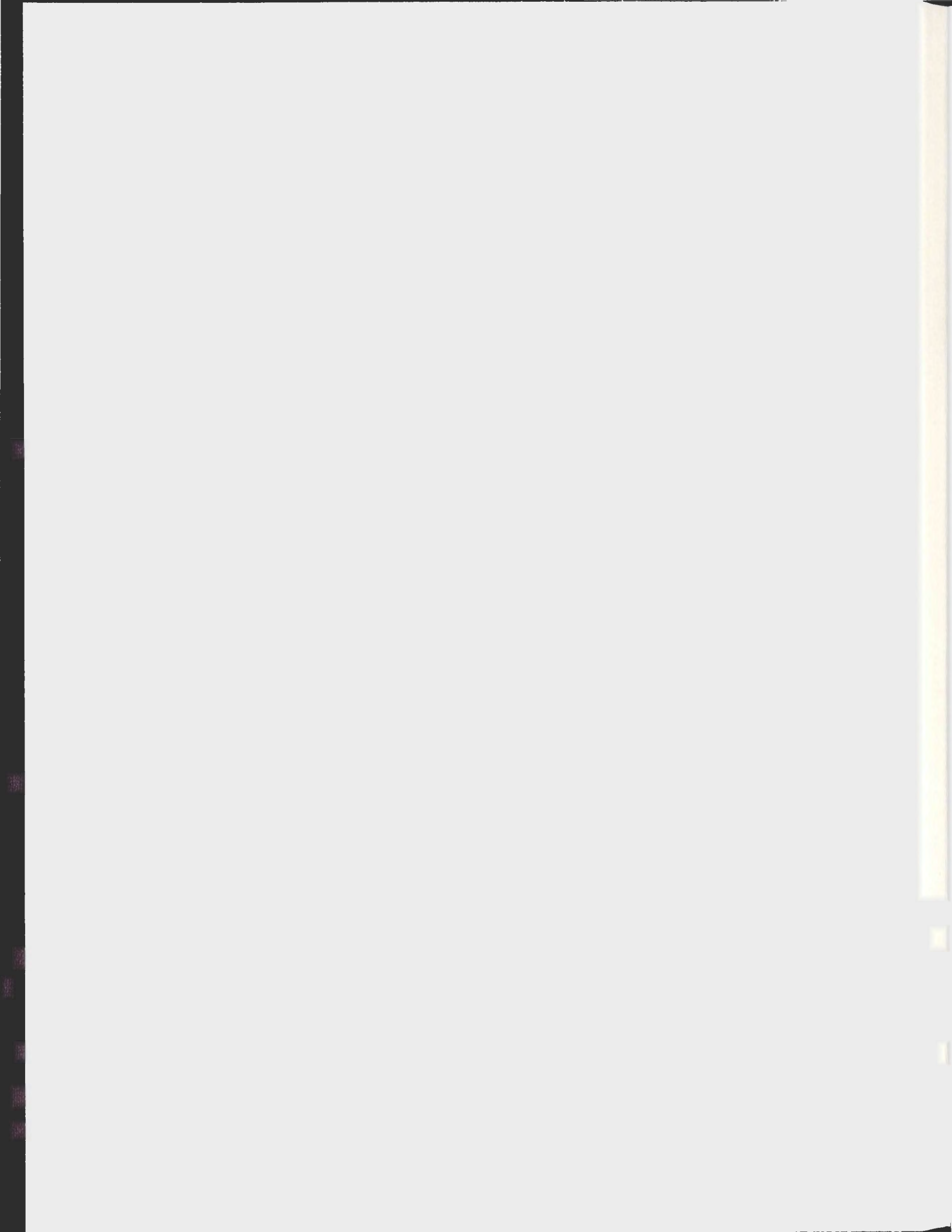


REGIONAL ATMOSPHERIC DYNAMIC DOWNSCALING  
OVER THE SUBPOLAR NORTH ATLANTIC

YING ZHANG





**Regional Atmospheric Dynamic Downscaling over the  
Subpolar North Atlantic**

by

**©Ying Zhang**

A thesis submitted to the

School of Graduate Studies

in partial fulfillment of the requirements for the degree of

**Master of Science**

Department of Physics and Physical Oceanography

Memorial University of Newfoundland

July 07, 2010

St John's

Newfoundland

## **Abstract**

This study will present results from model simulations of high-resolution atmospheric seasonal and interannual variability in the subpolar North Atlantic from 1980 to 2005. A regional atmospheric model, the Weather Research and Forecasting (WRF) Model, is used in this study to downscale the NCEP/NCAR reanalysis for the subpolar North Atlantic Ocean. The WRF simulations represent realistically small-scale patterns in the surface water and heat fluxes in the central Labrador Sea and atmospheric variability related to the so-called Greenland tip jets.

In the second part of this study the WRF model simulations are used to force an ocean coupled sea-ice model. The ocean model results are compared with the ocean simulation forced with the NCEP/NCAR reanalysis. It is shown that the winter deep convection and ocean subpolar circulation are improved in the simulations forced with the WRF atmospheric fields. In particular, the results show that severe winter events related to Greenland tip jets force intense winter convection in the Irminger Sea. The deep convection in the Labrador Sea and the Labrador Sea Water Mass properties are also more realistic in the ocean simulation force with the WRF results than in the simulation forced with the NCEP/NCAR reanalysis.

## **Acknowledgements**

First of all, I would like to thank my supervisor, Dr. Entcho Demirov, for his guidance, patience and encouragement during my Master's studies. He has instructed and supported me to be able to work out this thesis. I would also like to thank Dr. Len Zedel for instruting me as well as for serving on my committee.

I thank Chris Steveson for his constant support in computer and technique. I also want to thank the other staff of Department of Physics and Physical Oceanography for their assistance in every aspect of my Master's program.

In addition, thanks go to the fellow graduate students for their encouragement, friendship and the happy times we have spent together: Julio Salcedo, Jeremy Dillon, Kentaro Kato, Sarah Lundrigan, Mark Kavanagh, Tristan Hauser, Sheilagh O'Leary, Kevin Le Morzadec, Robert Briggs, Andrew Keats, Sara Best, and William Fowler, Zhaoshi Lu, Zhimin Ma.

At last but not least, I want to thank my husband for accompanying, supporting, and encouraging me at all times. Thanks to my parents and my little brother for their continuous support and comprehension.

# Contents

<b>Abstract</b> .....	<b>ii</b>
<b>Acknowledgements</b> .....	<b>iii</b>
<b>Contents</b> .....	<b>iv</b>
<b>List of Tables</b> .....	<b>vi</b>
<b>List of Figure</b> .....	<b>vii</b>
<b>List of Acronyms</b> .....	<b>xii</b>
<b>Chapter 1: Introduction</b> .....	<b>1</b>
1.1 Atmospheric variability over the subpolar North Atlantic Ocean.....	1
1.2 Oceanic variability in the subpolar North Atlantic .....	6
1.3 Regional Downscaling .....	11
1.4 Objectives and Outline of the Present Study.....	12
<b>Chapter 2: Numerical Models and Experimental Design</b> .....	<b>14</b>
2.1 The Regional Fine-Resolution Atmospheric Model .....	14
2.1.1 Governing equations .....	15
2.1.2 Sub-scale physical parameterizations.....	22
2.1.3 Model setup and implementation .....	25
2.2 The Ocean Model .....	27
2.2.1 Governing equations .....	27
2.2.2 Model setup and implementation .....	29
2.3 Experimental Design.....	31
<b>Chapter 3: Model Simulations of Climatological Characteristics and Interannual Variability of Subpolar North Atlantic Atmosphere</b> .....	<b>35</b>
3.1 Climatological Features of Atmosphere.....	36
3.2 Dominant Modes of Atmospheric Variability.....	45
3.3 Discussion .....	62

<b>Chapter 4: Orographic effects of Greenland on the Atmospheric Flow: Greenland Tip Jets .....</b>	<b>64</b>
4.1 The Forward Greenland Tip Jet: Case study, February 14-15, 2000 .....	64
4.2 Discussion .....	79
<b>Chapter 5: Modeling Interannual Variability in the Subpolar North Atlantic Ocean .....</b>	<b>81</b>
5.1 Simulations of Interannual Variability of North Atlantic Subpolar Gyre.....	83
5.2 Impacts of High-Resolution Atmospheric Forcing on Subpolar North Atlantic Simulations.....	90
5.3 Discussion .....	97
<b>Chapter 6: Conclusion .....</b>	<b>99</b>
6.1 Major findings.....	99
6.2 Future work .....	100
<b>References .....</b>	<b>101</b>

## List of Tables

Table 2.1	The WRF physics parameterizations that are chosen in the WRF simulation.	22
Table 2.2	The NEMO model parameters used in the ocean simulation.....	30
Table 2.3	Numerical experiments. ....	32
Table 3.1	Variances of the first and second EOF spatial patterns of atmospheric fields averaged in the winter months (JFM) during the 26 years from the NCEP/NCAR reanalysis data and the WRF outputs.....	46
Table 5.1	Variances of the first and second EOF spatial patterns of oceanic fields averaged in winter months (JFM) during the 26 years from the old and new experiments. ....	95

## List of Figure

Figure 1.1	Topography of the Sub-polar Atlantic regions (height in meters).....	4
Figure 1.2	Circulation of the main water masses in the North Atlantic from Rhein (2000). .....	7
Figure 2.1	WRF system components (Skamarock, et al., 2008).....	15
Figure 2.2	ARW $\eta$ coordinate. (Skamarock, et al., 2008) .....	16
Figure 2.3	Horizontal and vertical grids of the ARW. (Skamarock, et al., 2008).....	19
Figure 2.4	A Specified lateral boundary condition for a real-data case. ....	20
Figure 2.5	Schematic showing the data flow and program components in the WPS, and how the WPS feeds its outputs to the ARW. Letters in the rectangular boxes indicate program names. (Skamarock, et al., 2008).....	25
Figure 2.6	The WRF simulation domain.....	27
Figure 2.7	The NEMO simulation domain covering the entire North Atlantic Ocean. ...	33
Figure 2.8	A schematic figure of the first three runs of the atmospheric experiment.....	34
Figure 3.1	Precipitation (mm/day) from the NCEP/NCAR reanalysis data and the WRF outputs averaged in the winter months (JFM) and summer months (JAS) during the whole experimental time (1980-2005) and differences between the two datasets in the two seasons. ....	37
Figure 3.2	Same as Figure 3.1, but for 2-m relative humidity. ....	39
Figure 3.3	Same as Figure 3.1, but for 2-m air temperature (K). ....	40

Figure 3.4	Same as Figure 3.1, but for surface zonal wind stress ( $N/m^2$ ).....	42
Figure 3.5	Same as Figure 3.1, but for surface meridional wind stress ( $N/m^2$ ).....	43
Figure 3.6	Same as Figure 3.1, but for 10-m wind speed (m/s).....	44
Figure 3.7	The first EOF mode of precipitation averaged in the winter months (JFM) during the 26 years from the NCEP/NCAR reanalysis data and the WRF outputs.....	47
Figure 3.8	The second EOF mode of precipitation averaged in the winter months (JFM) during the 26 years from the NCEP/NCAR reanalysis data and the WRF outputs.....	48
Figure 3.9	The first EOF mode of 2-m relative humidity averaged in the winter months (JFM) during the 26 years from the NCEP/NCAR reanalysis data and the WRF outputs.....	50
Figure 3.10	The second EOF mode of 2-m relative humidity averaged in the winter months (JFM) during the 26 years from the NCEP/NCAR reanalysis data and the WRF outputs.....	51
Figure 3.11	The first EOF mode of 2-m air temperature averaged in the winter months (JFM) during the 26 years from the NCEP/NCAR reanalysis data and the WRF outputs.....	52
Figure 3.12	The second EOF mode of 2-m air temperature averaged in the winter months (JFM) during the 26 years from the NCEP/NCAR reanalysis data and the WRF outputs.....	54

Figure 3.13	The first EOF mode of surface zonal wind stress averaged in the winter months (JFM) during the 26 years from the NCEP/NCAR reanalysis data and the WRF outputs.....	55
Figure 3.14	The second EOF mode of surface zonal wind stress averaged in the winter months (JFM) during the 26 years from the NCEP/NCAR reanalysis data and the WRF outputs.....	56
Figure 3.15	The first EOF mode of surface meridional wind stress averaged in the winter months (JFM) during the 26 years from the NCEP/NCAR reanalysis data and the WRF outputs.....	57
Figure 3.16	The second EOF mode of surface meridional wind stress averaged in the winter months (JFM) during the 26 years from the NCEP/NCAR reanalysis data and the WRF outputs. ....	58
Figure 3.17	The first EOF mode of 10-m wind speed averaged in the winter months (JFM) during the 26 years from the NCEP/NCAR reanalysis data and the WRF outputs. ....	60
Figure 3.18	The second EOF mode of 10-m wind speed averaged in the winter months (JFM) during the 26 years from the NCEP/NCAR reanalysis data and the WRF outputs. ....	61
Figure 4.1	A forward Greenland tip jet during February 14-15, 2000.....	67
Figure 4.2	Meteorological features at 00:00 February 13, 2000.....	71
Figure 4.3	Same as Figure 4.2, but at 12:00 February 13, 2000.....	73
Figure 4.5	Same as Figure 4.2, but at 12:00 February 14, 2000.....	77
Figure 4.6	Same as Figure 4.2, but at 18:00 February 15, 2000.....	79

Figure 4.7	Sea ice coverage in February, 2000.....	79
Figure 5.1	Map of the sub-polar North Atlantic.....	82
Figure 5.2	Potential temperature (°C, left panel) and salinity (psu, right panel) averaged in May and June of 1993 along the AR7W section from the results of the Exp_SPNCEP (upper panel) and Exp_SPWRF (lower panel) experiments (Table 2.3), respectively.....	84
Figure 5.3	Same as the Figure 5.2, but in 2005.....	85
Figure 5.4	Mixed layer depth (m) at the end of March in 1993 (left panel) and 2005 (right panel).....	87
Figure 5.5	Potential temperature (°C, left panel) and salinity (psu, right panel) averaged in May and June of each year during 1980-2005 over the central Labrador Sea from the results of the Exp_SPNCEP (upper panel) and the Exp_SPWRF (lower panel) experiments (Table 2.3), respectively.....	88
Figure 5.6	Yearly barotropic stream function (BSF, Sv) from averaged over the ocean area in (46.05°N – 65.70°N, 72.75°W – 22.25°W).....	89
Figure 5.7	Sea surface temperature (SST, °C).....	91
Figure 5.8	Barotropic stream function (Sv) in 1993.....	92
Figure 5.9	Yearly barotropic stream function (Sv) difference between 1995 and 1999.....	94
Figure 5.10	The first EOF mode of net downward heat flux averaged in winter month (JFM) during the 26 years from the results of the Exp_SPNCEP and the EXP_SPWRF experiments.....	96

Figure 5.11 The second EOF mode of net downward heat flux averaged in winter month (JFM) during the 26 years from the results of the Exp\_SPNCEP and the Exp\_SPWRF experiments.....97

## List of Acronyms

<b>AABW</b>	Antarctic Bottom Water
<b>ARW</b>	Advanced Research WRF
<b>BC</b>	Baffin Island Current
<b>BSF</b>	Barotropic Stream Function
<b>CERSAT</b>	Centre ERS d'Archivage et de Traitement
<b>CFL</b>	Courant-Friedrichs-Lewy condition
<b>CGFZ</b>	Charlie-Gibbs Fracture Zone
<b>DSOW</b>	Denmark Strait Overflow Water
<b>EA</b>	East Atlantic pattern
<b>ECMWF</b>	European Centre for Medium-Range Weather Forecasts
<b>EGC</b>	East Greenland Current
<b>EOF</b>	Empirical Orthogonal Function
<b>ERA-40</b>	ECMWF reanalysis data for 45 years
<b>FASTEX</b>	Fronts and Atlantic Storm-Track Experiment
<b>FBC</b>	Faroe Bank Channel
<b>IC</b>	Irminger Current
<b>ISOW</b>	Iceland-Scotland Overflow Water
<b>JAS</b>	July, August and September
<b>JPL</b>	Jet Propulsion Laboratory

<b>JFM</b>	January, February and March
<b>LC</b>	Labrador Current
<b>LIM2</b>	Louvain-la-Neuve Ice Model
<b>LSM</b>	Land-Surface Model
<b>LSW</b>	Labrador Sea Water
<b>MEDAR</b>	Mediterranean Data Archeology and Rescue data
<b>MMM</b>	Mesoscale and Microscale Meteorology division
<b>MM5</b>	Fifth-Generation NCAR/Penn State Mesoscale Model
<b>MOC</b>	Meridional Overturning Circulation
<b>MW</b>	Mediterranean Water
<b>NAC</b>	North Atlantic Curren
<b>NADW</b>	North Atlantic Deep Water
<b>NAO</b>	North Atlantic Oscillation
<b>NCAR</b>	National Center for Atmospheric Research
<b>NCEP</b>	National Center for Environmental Prediction
<b>NEMO</b>	Nucleus for European Models of the Ocean modeling system
<b>NOAA</b>	National Oceanic and Atmospheric Administration
<b>NWP</b>	Numerical Weather Prediction
<b>OBC</b>	Open Boundary Conditions
<b>OSU</b>	Oregon State University
<b>PC</b>	Principle Component
<b>PBL</b>	Planetary Boundary Layer
<b>QuikSCAT</b>	Quick Scatterometer

<b>RK3</b>	Third-order Runge-Kutta time integration scheme
<b>RR</b>	Reykjanes Ridge
<b>RRTM</b>	Rapid Radiative Transfer Model
<b>SODA</b>	Simple Ocean Data Assimilation data
<b>SPMW</b>	Subpolar Mode Water
<b>SST</b>	Sea Surface Temperature
<b>WGC</b>	West Greenland Current
<b>WOA05</b>	World Ocean Atlas 2005 dataset
<b>WPP</b>	WRF Post-processing verification
<b>WPS</b>	WRF Preprocessing System
<b>WRF</b>	Weather Research and Forecasting model
<b>WSF</b>	WRF Software Framework
<b>WSM3</b>	WRF single- moment 3-class scheme
<b>YSU</b>	Yonsei university

## **Chapter 1: Introduction**

The subpolar North Atlantic Ocean is the region north of 45°N, south of the Greenland-Scotland Ridge and bordered to the east by the European continental shelf and to the west by the Davis Strait, Hudson Strait and the Canadian continental shelf. Over this region, a large number of important atmospheric and oceanic processes influence the weather and climate conditions of the subpolar North Atlantic.

### **1.1 Atmospheric variability over the subpolar North Atlantic Ocean**

The subpolar Ocean has its unique climate conditions. Over the boundary of cold polar air transported by the polar cell and warm air transported by the atmosphere Ferrel cell in the Northern Hemisphere, there exists the polar front. Hence, a sharp atmospheric temperature gradient occurs off the coast of eastern North America. The polar front is a quasi-stationary front extending for thousands of miles. The average position of the polar front is about 30°N during winter and 60°N in summer. Most extratropical cyclones are generated along the front. The Icelandic Low, a semi-permanent center of atmospheric action, is a low pressure zone between Iceland and southern Greenland in winter. It forms due to the thermal contrast between the continent and the ocean. It is a dominant pattern of sea level pressure in mid-high latitudes (Serreze et al., 1997) and determines the atmospheric circulation and high winds over the subpolar North Atlantic.

The climatological mean surface air temperature over the subpolar North Atlantic region is determined by many factors: absorbed solar radiation, ocean surface temperature, and local surface processes. In winter, the lowest temperature is observed over the Labrador Sea and the highest temperature is near the British Isles over the Northeast Atlantic Ocean. In summer, the entire subpolar North Atlantic Ocean near surface atmosphere has more homogenous moderate temperature around 281-285 °K. The largest seasonal differences appear over the Labrador Sea, the Northwest Atlantic and the smallest seasonal differences occur over the Northeast Atlantic Ocean. This distribution is associated with the impacts of the cold Labrador Current (LC) and North Atlantic Current (NAC) in the subpolar North Atlantic.

The North Atlantic Oscillation (NAO) is the dominant pattern of climate variability over the North Atlantic (Hurrell, 1995). It is characterized by the climate north-south fluctuations in atmospheric sea-level pressure differences between the Icelandic Low and the Azores high in the North Atlantic Ocean (Walker, 1924). Having a typical meridional dipolar pattern, it can exist in two phases: the positive and negative phase. The positive (negative) NAO phase is characterized by the stronger-(weaker-) than-average and further north (south) located Icelandic Low and Azores high (Angell and Korshover, 1974). Observational, theoretical and modeling studies suggest that the fluctuation of the NAO notably and widely affects the atmosphere and the North Atlantic Ocean. It has evident impacts on air temperature, precipitation, mean wind field, the transport of heat and moisture, and storms over the North Atlantic and surrounding continents (Walker and Bliss, 1932; Hurrell, 2003). It also influences sea surface temperature (SST), the ocean circulation and sea-ice cover over the North Atlantic Ocean (Hurrell et al., 2003).

During the positive phase of the NAO, the deeper-than-normal Icelandic Low brings stronger-than-normal northerlies over Greenland and northeastern Canada. The cold air transported southward by the strong northerlies cools surface temperature over the Northwest Atlantic Ocean (Hurrell et al., 2003). Storms are more intense and frequent in the vicinity of Iceland and in the Norwegian Sea (Hurrell et al., 2003). Meanwhile, less-than-normal precipitation falls over much of Greenland and more-than-normal precipitation over Iceland (Hurrell, 1995). During the negative NAO phase, patterns of pressure anomalies are opposite to the positive phase: the weaker-than-normal and further south located Icelandic Low and Azores High. The cold northerly wind from the polar area is weaker than normal and thus less cold air from the polar area, more-than-normal precipitation in Western Greenland, and drier-than-normal in Iceland.

Greenland, the largest island in the world, is located over the subpolar North Atlantic Ocean. The topography (Figure 1.1) of Greenland is a gradually sloping ice-covered plateau exceeding 3000 m with an extremely steep mountainous coast (Doyle and Shapiro, 1999). This multi-scale terrain complicates the atmospheric processes and impacts the weather and climate of the North Atlantic (Petersen et al. 2003). Greenland tip jets, low-level and intermittent high winds blowing near Greenland, are convincing examples of the influence of the Greenland high topography (Doyle and Shapiro, 1999).

Greenland tip jets, which periodically form and usually sustain couple of days in the vicinity of Cape Fare (the red dot on Figure 1.1), the southernmost point of Greenland, are currently categorized into two classes: forward tip jets and reverse tip jets. These two classes of tip jets have distinct characteristics. The forward Greenland tip jet, firstly identified by Dolye and Shapiro in 1999 (Doyle and Shapiro, 1999), is characterized by

intense westerly/northwesterly winds with a jet core at northeast of Cape Farewell, the southernmost point of Greenland. It is always associated with a strong synoptic-scale cyclone situated to the northeast of Cape Farewell over the Irminger Sea. It typically spans around 200 km north to south and about 1000 km east to west. The surface wind speeds of the forward tip jet usually exceed 25 m/s and the wind directions along the streamline tend to exhibit a cyclonic turning (Doyle and Shapiro, 1999; Moore and Renfrew, 2005).

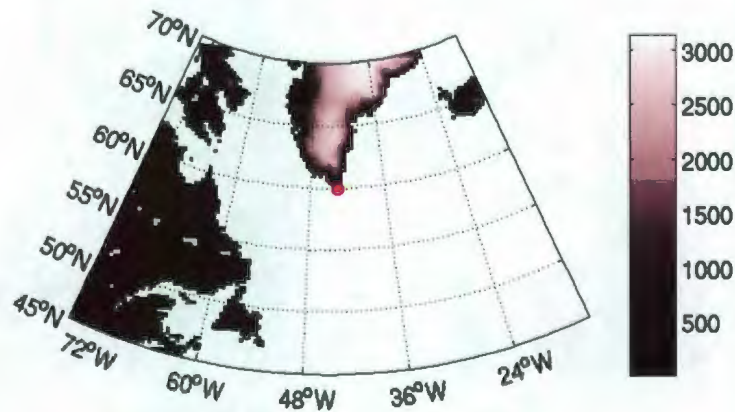


Figure 1.1 Topography of the Sub-polar Atlantic regions (height in meters)  
(The red dot over the southern Greenland indicates the location of Cape Farewell)

On the contrary, the reverse Greenland tip jet, a newly found phenomenon by Moore (2003) using the 10-m wind field from the NCEP/NCAR reanalysis data for the period 1948-2000 (Kalnay et al., 1996), is featured by strong easterly winds near Cape Farewell. It also relates to a deep cyclonic system which is usually located over the south of Cape Farewell. Compared with the more zonal spanning of the forward tip jet, the reverse tip

jet has a larger meridional extent of hundreds kilometres. The peak wind speed of the reverse tip jet can also be in excess of 25 m/s and wind directions along the streamline has a anticyclonic turning (Ohigashi and Moore, 2009).

Both classes of tip jets form and develop arising from the interaction of synoptic-scale cyclonic system with the high topography of Greenland (Doyle and Shapiro, 1999; Moore and Renfrew, 2005; Vage et al., 2009). Based on climatological QuikSCAT surface wind fields, both classes of tip jets most commonly occur during the winter, with highest 10% probability of occurrence in winter and almost 0% probability in summer (Moore, 2003). The frequency of forward (reverse) tip jets is positively correlated with the positive (negative) phase of the NAO. Moore (2003) indicated that in the winter with the positive phase of the NAO, forward tip jets have a 14% probability of occurrence, which is 8% higher than reverse tip jets do. In contrast, reverse tip jets have a 12% probability during the winter with the negative phase of the NAO, versus only 5% for forward tip jets. Later, Vage et al. (2009) further investigated the frequency of forward tip jets using the ECMWF reanalysis data (ERA-40) and found that the latitude of the Icelandic Low is another comparable important factor which modulates the frequency of forward tip jets.

High westerly and easterly winds of Greenland tip jets produce strong wind stress curl and large air-ocean heat flux which result in intense air-sea interaction over the subpolar North Atlantic Ocean. Dolye and Shapiro (1999) found that cold and dry polar air is advected around Cape Farewell by forward tip jets and thus create large heat flux in the jet core from the model simulation. Pickart et al. (2003) suggested that large heat flux and strong wind stress curl caused by Greenland forward tip jets force deep oceanic

mixing and contributes to convection in the Irminger Sea. Martin and Moore (2007) simulated evident high surface sensible and latent heat fluxes and heavy precipitation associated with a reverse tip jet in December, 2000 and indicated that reverse tip jets could be important in the deepening of the mixed layer and deep convection in the region to the west of Cape Farwell.

The Greenland tip jets are presented in the QuikSCAT observation (Moore and Renferew, 2005). At the same time, they are considerably underestimated in either detailed structure or peak magnitude in the relatively low-resolution global meteorological analysis (e.g. NCEP/NCAR reanalysis data) (Moore, 2003). Hence, downscaling is needed to obtain fine-resolution meteorological data, which would properly represent the dynamics of Greenland tip jets.

## **1.2 Oceanic variability in the subpolar North Atlantic**

Various oceanic currents and water masses are involved in the dynamics and circulation of the subpolar North Atlantic Ocean. The main currents and water masses in this region are shown on Figure 1.2 from the work of Rhein (2000).

The bathymetry of the subpolar North Atlantic is characterized by the coexistence of the Laurentian Abyss off the eastern coast of Canada and the submarine Mid-Atlantic Ridge from Iceland to the South Atlantic. The water in the Laurentian Abyss is about 6000 m in depth and the water at the peak of the Mid-Atlantic Ridge is less than 2700 m in depth. Hence, the subpolar North Atlantic is deep in the western part and shallower in the east.



Figure 1.2 Circulation of the main water masses in the North Atlantic from Rhein (2000). (Red (warm and saline water) and green (cold and fresh water) indicate circulation in the upper 500 m; the switch from red to orange indicates cooling of warm subtropical water masses in the subpolar North Atlantic. White shows circulation at intermediate (500–2,000 m) depths; this is the Labrador Sea water (LSW) tracked by Lavender et al. (2000). Blue is circulation below 2,000 m. FC, Flemish Cap; CGFZ, Charlie-Gibbs Fracture Zone; FBC, Faroe Bank Channel; RR, Reykjanes Ridge; C, the region in the Labrador Sea where LSW forms.)

The Subpolar North Atlantic is occupied by six main water masses from the surface to the bottom: Subpolar Mode Water (SPMW), Labrador Sea Water (LSW), Mediterranean Water (MW), Iceland-Scotland Overflow Water (ISOW), Denmark Strait Overflow Water (DSOW) and Antarctic Bottom Water (AABW).

SPMW is distributed over a large area in the subsurface (upper 1000m) Subpolar North Atlantic and characterized by very low static stability and low potential vorticity. It originates as a warm (14-15 °C) and thick layer in the NAC loop. There, it is advected south of the NAC to the eastern Atlantic, and becomes colder and denser. SPMW with a temperature of 11-12 °C then splits into a southward and a northward flow. The latter warm surface water flows into the subpolar gyre. SPMW is thought to split once more into a branch that exits into the Nordic Seas. Another branch circulates into the Irminger Sea and then into the Labrador Sea where it provides the source water for LSW production (Talley and McCartney, 1982).

The surface current system of the Subpolar North Atlantic is dominated by a large-scale cyclonic gyre with warm and saline subtropical waters entering the northeastern Atlantic and subsequently recirculating to the north and west, where they interact with cold and fresh waters of Arctic origin (red and green arrows in Figure 1.2). The Gulf Stream is the main source of warm and saline water for the Subpolar North Atlantic. It enters the Subpolar North Atlantic at about 50°W, hence called the NAC. The water of the NAC is divided into several branches. One crosses the Iceland-Scotland Ridge and enters the Nordic Seas. Another branch returns in a big cyclonic loop to the Irminger Sea, hence termed the Irminger Current (IC). In the western coast of the Irminger Basin, the warm and salty surface waters interact with the currents of Arctic origin transport cold and fresh

waters. The East Greenland Current (EGC) enters the Subpolar North Atlantic at Denmark Strait, and flows south along the coast of Greenland. Then, the EGC turns west, and feeds the West Greenland Current (WGC). The WGC flows northwest along the west coast of Greenland, when near its end it flows west, and feeds the Baffin Island Current (BC) through combining with the outflow from the Arctic Ocean. As a continuation of the BC, the Labrador Current (LC) flows southwest along the coast of Labrador.

The mid-depth (nominally 1000-3000m) subpolar North Atlantic is occupied by LSW as well as MW. LSW is formed by deep winter convection in the Labrador Sea. It is often taken to have a temperature between 3 °C and 4 °C and a salinity less than 34.94 psu (Worthington, 1976), and may vary interannually (Yashayaev, 2007). Its formation is seasonal and occurs not every year. LSW is considered to be the lightest constituent of NADW. The other influential mid-depth subpolar water mass is MW. Pure MW overflows into the eastern North Atlantic through the Strait of Gibraltar at a temperature near 11.9 °C and salinity 36.50 psu (Wüst, 1935), and is diluted with ambient water during descent into the deep sea then spreads out as a high salinity water mass with temperature above about 3 °C.

At depth, the subpolar North Atlantic gyre is dominated by the circulation of LSW (white arrows in Figure 1.2). Talley and McCartney (1982) identified three main mid-depth transport pathways for LSW. Some LSW enters the Deep Western Boundary Current (DWBC) and flows into the subtropics (namely DWBC pathway). Some LSW crosses the mid-Atlantic Ridge into the West European Basin (namely Eastern Basin pathway). Some LSW flows into the Irminger Sea (Irminger pathway). In addition, a

fourth pathway, i.e., the interior pathway, was indentified by RAFOS floats-based studies (Bower et al., 2009).

At the deep and abyssal basins (nominally, deeper than 2,500 m), there are three main water masses: DSOW, ISOW and AABW. The formation of DSOW and ISOW are both related to water masses that have their origin in the Nordic Seas. AABW is also an important component of the abyssal water mass structure from the south. McCartney (1992) has shown AABW enters the subpolar domain along the eastern slopes of both the Newfoundland and West European Basins.

The deep circulation of the North Atlantic is fed by the cold and dense overflow water masses, i.e., DSOW and ISOW (Blue arrows in Figure 1.2), as well as AABW. DSOW passes across the 600 m deep saddle between Greenland and Iceland, entraining water from its surrounding. Leaving the Greenland Sea with 2.5 Sv its flow increases to 10 Sv south of Greenland. It is cold and relatively fresh, flowing below 3500 m in the DWBC and spreading inward the deep Atlantic basins. ISOW crosses the 850 m saddle point in the Faroe Bank Channel and flows along the eastern flank of the Reykjanes Ridge and then passes through the 3,600 m deep Charlie-Gibbs Fracture Zone into the Irminger Basin. While flowing, it also entrains water from surrounding areas. DSOW and ISOW joint together at the west of Irminger basin and follow the western sides of Irminger, Labrador and Newfoundland Basins as pronounced Deep Western Boundary Current (DWBC).

### 1.3 Regional Downscaling

As aforementioned, Greenland tip jets, which may play an important role in the variability of the subpolar North Atlantic Ocean, are usually underestimated in global reanalysis data. This is because the spatial resolution of global reanalysis is about 200 km. They represent only large- and synoptic-scale atmospheric features and under-represent some localized phenomena. A possible solution for studying regional processes is “downscaling”, in which dynamical or statistical models are used to relate large-scale information to local parameters. Each dynamical or statistical approach has its own disadvantage and advantage (Von Storch, 1995).

Statistical downscaling utilizes a statistical model which relates large-scale climate state to regional and local variables (Von Storch, 1995). One of the primary advantages of these statistical procedures is computationally efficiency and thus easy implementation. The application of downscaling techniques varies widely with respect to regions, spatial and temporal scales, and climate statistics. Statistical downscaling is based on the empirical links between large-scale and local variables that have been observed in the past. However, these links may vary and may not be suitable for variable climate conditions. In addition, it ignores possible systematic changes in regional forcing conditions or feedback processes (Giorgi et al., 2001).

Dynamical downscaling employs a numerical model based on the complete meteorological equations needed to simulate weather and climate. Unlike statistical downscaling, it does not use local observed data but does have the potential to outperform statistical methods. However, it requires high computational facilities and large data

storage if the regional model has very fine resolution (Diez et al., 2005). At present, dynamical downscaling can only be used for small areas or in event case studies.

In this thesis, the dynamic downscaling method, based on a higher-resolution regional model, is chosen to estimate atmospheric conditions over the subpolar North Atlantic and their impacts on the ocean simulation.

## **1.4 Objectives and Outline of the Present Study**

The objectives of this thesis are as follows:

- (1) to setup a high-resolution regional atmospheric model to dynamically downscale a reanalysis data and obtain fine-resolution atmospheric data;
- (2) to test the validity of the atmospheric model;
- (3) to investigate the advantages of the fine-resolution atmospheric data and important local processes;
- (4) and to use an ocean model to examine the improvements of the ocean responses to fine-resolution atmospheric data.

The thesis includes the following chapters. The numerical models used in this study are described in Chapter 2. The comparative analysis of the seasonal mean quantities and dominant modes of the regional atmospheric model results and the NCEP/NCAR reanalysis data (Kalnay et al., 1996) are presented in Chapter 3. To investigate the dynamic features of Greenland tip jets, a typical case of forward Greenland tip jets is studied in Chapter 4. The results of the ocean simulation forced with high-resolution

regional data are presented in Chapter 5. Conclusion and possible future extension of the present study are discussed in Chapter 6.

## **Chapter 2: Numerical Models and Experimental Design**

Two numerical tools are used in this study: (1) a regional atmospheric model and (2) an ocean general circulation model. This chapter describes the model equations, numerical schemes of these two models, and their implementations to the subpolar North Atlantic Ocean.

### **2.1 The Regional Fine-Resolution Atmospheric Model**

A next-generation mesoscale model, the Weather Research and Forecasting (WRF) model version 3.1.1 (Skamarock, et al., 2008), has been implemented for the sub-polar Atlantic Ocean. The WRF model is a numerical tool used in theoretical and operational numerical weather prediction (NWP) and atmospheric simulation system. It was collaboratively developed by the National Center for Atmospheric Research's (NCAR) Mesoscale and Microscale Meteorology (MMM) Division, the National Oceanic and Atmospheric Administration's (NOAA) National Center for Environmental Prediction (NCEP) and many other scientific communities (Skamarock, et al., 2008).

The WRF system (Figure 2.1) includes three fundamental components: WRF Preprocessing System (WPS), WRF Software Framework (WSF) and Post-processing verification. The WPS prepares input files for the WRF; the WRF contains dynamics solvers, physics packages, WRF-Var data assimilation, and WRF-Chem components; the

WRF Post-processing (WPP) verification provides the tools which can be used to analyze and display the WRF outputs.

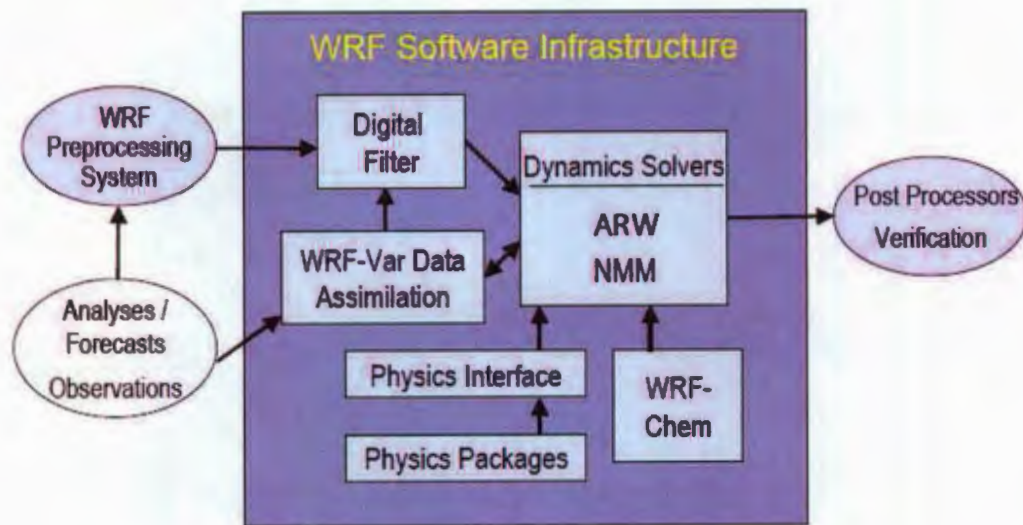


Figure 2.1 WRF system components (Skamarock, et al., 2008)

### 2.1.1 Governing equations

The WRF model is based on fully compressible, nonhydrostatic, and Euler equations of atmosphere in flux form which conserves mass, dry entropy, and scalars. The vertical coordinate used in the governing equations is a mass coordinate, i.e. a terrain-following, dry hydrostatic-pressure vertical coordinate  $\eta$  (Figure 2.2), and the top layer of the model is set as a constant pressure layer.

$$\eta = (p_{\text{at}} - p_{\text{at}_s}) / \mu_d \quad \text{where} \quad \mu_d = p_{\text{at}_s} - p_{\text{at}_t} \quad (2.1.1)$$

$p_{\bar{\sigma}}$  is the hydrostatic pressure of the dry atmosphere;  $p_{\bar{\sigma}_s}$  and  $p_{\bar{\sigma}_t}$  are the hydrostatic pressure along the surface and top of the dry atmosphere;  $\mu_d$  is the mass of the dry air in the column (Skamarock et al., 2008).

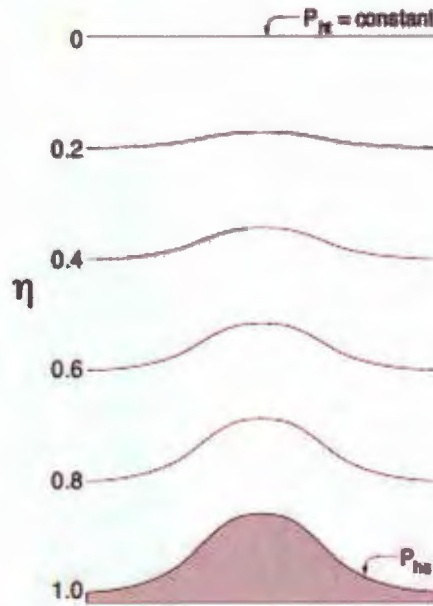


Figure 2.2 ARW  $\eta$  coordinate. (Skamarock, et al., 2008)

The governing equations include the conservation of momentum, potential temperature, mass, and moisture.

$$\partial_t U + m_x [\partial_x (Uu) + \partial_y (Vu)] + \partial_\eta (\Omega u) + \mu_d \alpha \partial_x p + (\alpha/\alpha_d) \partial_\eta p \partial_x \phi = F_U \quad (2.1.2)$$

$$\partial_t V + m_y [\partial_x (Uv) + \partial_y (Vv)] + (m_y/m_x) \partial_\eta (\Omega v) + \mu_d \alpha \partial_y p + (\alpha/\alpha_d) \partial_\eta p \partial_y \phi = F_V \quad (2.1.3)$$

$$\partial_t W + (m_x m_y / m_y) [\partial_x (Uw) + \partial_y (Vw)] + \partial_\eta (\Omega w) - m_y^{-1} g [(\alpha/\alpha_d) \partial_\eta p - \mu_d] = F_W \quad (2.1.4)$$

$$\partial_t \Theta + m_x m_y [\partial_x (U\theta) + \partial_y (V\theta)] + m_y \partial_\eta (\Omega \theta) = F_\Theta \quad (2.1.5)$$

$$\partial_t \mu_d + m_x m_y [U_x + V_y] + m_y \partial_\eta (\Omega) = 0 \quad (2.1.6)$$

$$\partial_t \phi + \mu_d^{-1} [m_x m_y (U \partial_x \phi + V \partial_y \phi) + m_y \Omega \partial_\eta \phi - m_y g W] = 0 \quad (2.1.7)$$

$$\partial_t Q_m + m_x m_y [\partial_x (U q_m) + \partial_y (V q_m)] + m_y \partial_\eta (\Omega q_m) = F_{Q_m} \quad (2.1.8)$$

$$\partial_\eta \phi = -\alpha_d \mu_d \quad (2.1.9)$$

$$p = p_0 (R_d \theta_m / p_0 \alpha_d) \quad (2.1.10)$$

Here  $g$ ,  $p_0$ ,  $R_d$ , and  $\gamma$  are constants:  $g$  is gravity,  $p_0 = 10^5$  Pascals is a reference pressure,  $R_d$  is the gas constant for dry air, and  $\gamma = c_p / c_v = 1.4$  is the ratio of the heat capacities of dry air.  $\alpha$  and  $\alpha_d$  are the specific volumes of the air and the dry air, respectively.  $m_x$  and  $m_y$  are map-scale factors: the ratio of the distance in computational space to the corresponding distance on the earth's surface.  $u$ ,  $v$ , and  $w$  are velocities in the two horizontal and vertical directions,  $p$  is pressure,  $\phi = gz$  is geopotential,  $q_m$  is the mixing ratio (mass per mass of dry air) for water vapour, cloud, rain, ice, etc,  $\theta$  is the potential temperature,  $\theta_m \approx \theta(1 + 1.61q_v)$ , and  $q_v$  is the mixing ratio for water vapour.  $U = \mu_d u / m_y$ ,  $V = \mu_d v / m_x$ ,  $W = \mu_d w / m_y$ ,  $\Omega = \mu_d \dot{\eta} / m_y$ ,  $\Theta = \mu_d \theta$ , and  $Q_m = \mu_d q_m$  are the flux form of  $u$ ,  $v$ ,  $w$ ,  $\dot{\eta}$ ,  $\theta$ , and  $q_m$ , respectively.  $F_U$ ,  $F_V$ ,  $F_W$ ,  $F_\Theta$ , and  $F_{Q_m}$  are terms due to the Coriolis force, curvature, turbulent mixing, and model physics. The Lambert conformal projection is utilized in this study to map the model equations from physical to computational spaces. (Skamarock et al., 2008)

The Advanced Research WRF (ARW) solver is employed to solve the governing equations (ARW version 3 modeling system User's Guide, 2009). The governing equations solved by the ARW are written into a perturbation form based on a

hydrostatically-balanced reference state. The discretization is then done using a finite difference method.

For temporal discretization, the ARW solver employs a third-order Runge-Kutta (RK3) time integration scheme combining with a time-splitting method to integrate a group of differential equations. Assuming that  $\Phi$  is any prognostic variable in the ARW solver and the model equations are written in the form of  $\partial_t \Phi = R(\Phi)$ , there are 3 steps in the RK3 scheme to advance a solution one timestep forward.

$$\Phi^{\circ} = \Phi^t + \frac{\Delta t}{3} R(\Phi^t) \quad (2.1.11)$$

$$\Phi^{\infty} = \Phi^t + \frac{\Delta t}{2} R(\Phi^{\circ}) \quad (2.1.12)$$

$$\Phi^{t+\Delta t} = \Phi^t + \Delta t R(\Phi^{\infty}) \quad (2.1.13)$$

where  $\Delta t$  is the time step, and  $\Phi^t$  and  $\Phi^{t+\Delta t}$  are the values of  $\Phi$  at the time  $t$  and  $t + \Delta t$ , respectively (Skamarock et al., 2008).

Atmospheric motion can be divided into two main components: slow, low-frequency modes and fast, high-frequency acoustic modes. The equations for the two modes are solved in the WRF model. This approach while beneficial from dynamic point of view imposes some limitations on computational efficiency. According to the Courant-Friedrichs-Lewy (CFL) condition, the fast modes would severely limit the time step in the time integration. In order to reduce the impact of this limitation and meanwhile to ensure the numerical stability and retain the fast acoustic modes, a time-splitting method is implemented in the WRF. In this approach, the RK3 scheme is applied to the slow modes with a large time step (namely, the model timestep). Within the RK3 sequences, a

forward-backward time integration scheme and a vertically implicit scheme are used to integrate the equations of fast acoustic and gravity-wave modes by using a small time step (namely, the acoustic time step). Typically, the model time step in seconds must be an even integer times the acoustic time step.

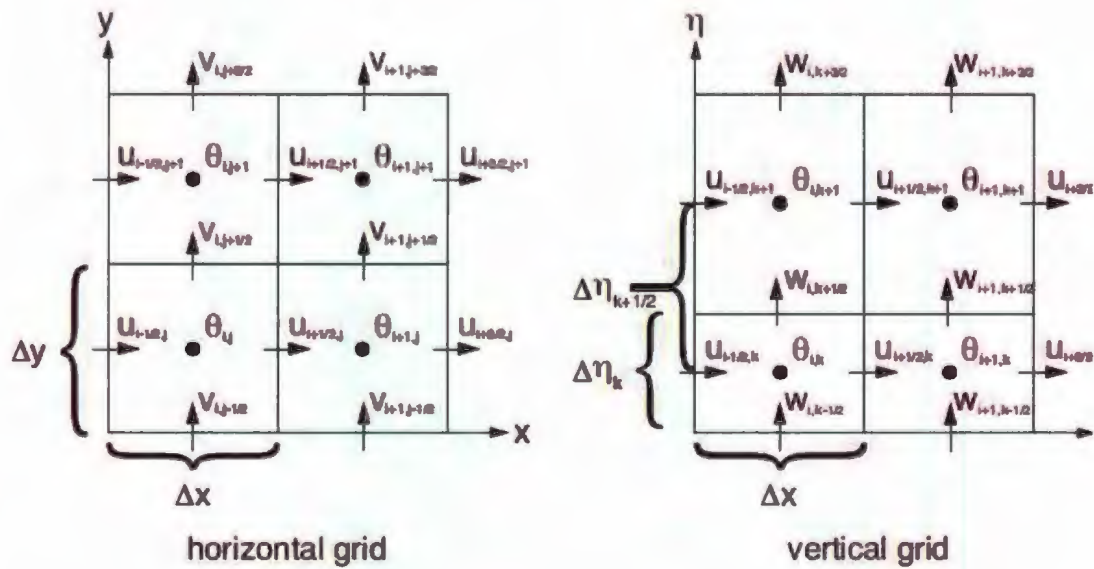


Figure 2.3 Horizontal and vertical grids of the ARW. (Skamarock, et al., 2008)

For spatial discretization, a staggered C grid is used in the ARW (Figure 2.3), which maintains accuracy in fine-resolution simulations. The diagnostic variables, such as  $\theta$ ,  $p$ ,  $\mu$ ,  $\alpha$ , and  $q_m$ , are calculated at the mass point;  $u$  and  $v$  are computed at the  $u$  and  $v$  points, respectively;  $w$  and  $\phi$  are at the  $w$  point. The horizontal grid lengths  $\Delta x$  and  $\Delta y$  are set as constants in the computational domain, which corresponds to variable spacing in the physical domain defined by the map-scale factors. The vertical grid length  $\Delta \eta_k$  is

not fixed and varies with  $k$ . Normally, a given horizontal grid length in kilometers is approximately 1/6 of the model time step in seconds.

In the finite difference method, the longitude scale converges towards the polar areas. This results in the decrease of the longitudinal grid length and the time step as well. A polar filter in the ARW is used to reduce the impact of this phenomenon on the model solution during the integration sequences.

For real simulations, the lateral boundary conditions are specified as two components (see Figure 2.4): a single row and column for a specified zone (*SpecZone*) determined entirely by temporal interpolation from an external forecast or analysis and four rows and columns for a relaxation zone (*RelaxZone*) where the model is nudged or relaxed towards the large-scale forecast.

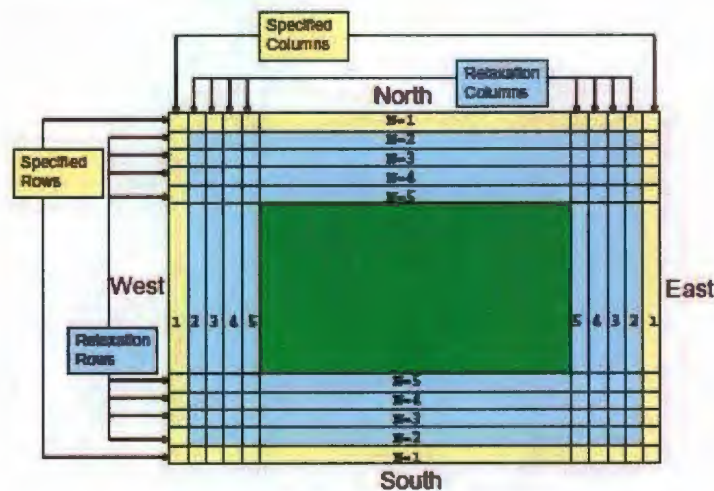


Figure 2.4 A Specified lateral boundary condition for a real-data case.

(It is comprised of specified and relaxation zones: a single row and column for the specified zone and four rows and columns for the relaxation zone. (Skamarock, et al., 2008))

Assume  $\Phi$  is any prognostic variable having a lateral boundary entry. The specified lateral boundary condition is then defined by

$$\partial_t \Phi|_n = W_1(\Phi_{LS} - \Phi) - W_2 \Delta^2 (\Phi_{LS} - \Phi), \quad (2.13)$$

where  $n$  is the number of grid points from the outer row or column along the boundary ( $SpecZone + 1 \leq n \leq SpecZone + RelaxZone - 1$ ) and  $\Phi_{LS}$  is the large-scale value obtained by spatial and temporal interpolation from the external analysis.  $\Delta^2$  is a 5-point horizontal smoother applied along  $\eta$ -surface. The weighting function coefficients  $W_1$  and  $W_2$  in (2.13) are given by

$$W_1 = \frac{1}{10\Delta t} \frac{SpecZone + RelaxZone - n}{RelaxZone - 1} \quad (2.14)$$

$$W_2 = \frac{1}{50\Delta t} \frac{SpecZone + RelaxZone - n}{RelaxZone - 1} \quad (2.15)$$

where  $n$  extends only through the relaxation zone ( $SpecZone + 1 \leq n \leq SpecZone + RelaxZone - 1$ ).  $W_1$  and  $W_2$  are linear ramping functions with a maximum at the first relaxation row or column near the coarse grid boundary (just inside the specified zone). (Skamarock et al., 2008)

At the top of the model, the pressure can be specified constant by users, such as 50 hPa in our experiments. A spatial filter, standard Rayleigh damping, or implicit Rayleigh damping is utilized to absorb vertically-propagating gravity waves to prevent unphysical wave reflection off the upper boundary.

### 2.1.2 Sub-scale physical parameterizations

Numerical integration of the governing equations can be used to resolve the dominant scales of atmospheric motions. The interaction between the resolved large-scale patterns and truncated scales of motion is resolved by the parameterizations of the nonresolvable smaller scale physical processes. The WRF parameterizations of these processes, i.e. the Physics Packages and Interfaces on the Figure 2.1, are briefly introduced as follows.

<b>Physics Parameterization</b>	<b>Options</b>
Microphysics	WRF Single-Moment 3-class (WSM3) scheme
Longwave radiation	Rapid Radiative Transfer Model (RRTM) scheme
Shortwave radiation	Dudhia scheme
Surface layer	MM5 similarity scheme
Land surface	Noah Land Surface Model
Urban Surface	None
Planetary boundary layer	Yonsei University scheme
Cumulus parameterization	Kain-Fritsch scheme

Table 2.1 The WRF physics parameterizations that are chosen in the WRF simulation.

Microphysics includes explicitly resolved water vapour, cloud, and precipitation processes. The WRF single- moment 3-class (WSM3) scheme based on Hong et al. (2004) is chosen for our simulations. This is a simple and computationally efficient scheme that

predicts three categories of hydrometers: vapour, cloud water/ice, and rain/snow. It assumes ice concentration to be a function of ice amount and improves ice microphysics.

The radiative quantities used in atmospheric models are the net (up and down) radiative fluxes at the top of the atmosphere and surface, and internal atmospheric heating rates. The purpose of a radiative transfer parameterization is to calculate the net radiative fluxes of solar and longwave radiation. However, the two radiations are considered separately, since the sources of the two radiations are different. Shortwave radiation comes from solar radiation with visible and surrounding wavelength, and longwave radiation consists of infrared or thermal radiation absorbed and emitted by gases and surfaces.

For the shortwave radiation, the MM5 (Dudhia) shortwave scheme (Dudhia, 1989) is used in the present study. It integrates downward, efficiently allowing for clear-air scattering, water vapour absorption, and cloud albedo and absorption. For the longwave radiation, the rapid radiative transfer model (RRTM) longwave scheme (Mlawer et al., 1997) is applied. It computes fluxes and cooling rates for the longwave spectrum and accounts for longwave processes arising from water vapour, ozone, carbon dioxide, trace gases, and microphysics species.

Cumulus parameterizations are used to resolve the sub-grid-scale effects of convective and/or shallow cloud. The physical processes and scales of the convective process range from microns to a few kilometres, and the corresponding parameterizations should be utilized when the model resolution is greater than their scales. On the contrary, if the model is fine enough ( $\leq 5$  km grid) to resolve the convective eddies itself, these schemes should not be activated. The Kain-Fritsch scheme is employed in our simulations.

This scheme follows Kain and Fritsch (1990, 1993) with some modification. It is a cloud model which calculates the exchanges of mass between clouds and their environment considering moist updrafts and downdrafts and the effects of detrainment, entrainment, and simple microphysics.

The planetary boundary layer (PBL) schemes calculate vertical sub-grid-scale fluxes profiles arising from eddy transports within the boundary layer and stable layer. Yonsei University (YSU) PBL based on Hong et al. (2006) is utilized in our simulations.

The land-surface models (LSM) estimate heat and moisture fluxes at land points and sea-ice points based on internal information on the land's state variables and land-surface properties and atmospheric information from the surface layer scheme, radiative forcing from the radiation schemes, and precipitation forcing from the microphysics and convective schemes. In this study, the Noah LSM is employed, which is based on the Oregon State University (OSU) LSM (Chen and Dudhia, 2001) and then developed by NCAR and NCEP. It diagnoses soil temperature and moisture in four layers and fractional snow cover considering vegetation processes, improved urban treatment, and surface emissivity properties. It computes surface sensible and latent heat fluxes as well.

The surface layer schemes provide friction velocities and exchange coefficients to the LSMs to calculate surface heat and moisture fluxes and to the PBL schemes to calculate surface stress. Each surface layer scheme is currently associated with a particular PBL scheme. The similarity theory (MM5) is the scheme tied to the YSU PBL scheme we choose. It calculates surface exchange coefficients for heat, moisture, and momentum using stability functions from Paulson (1970), Dyer and Hicks (1970), and Webb (1970), and convective velocity according to Beljaars (1994).

### 2.1.3 Model setup and implementation

The WRF model completes a real simulation through a series of steps (Figure 2.5).

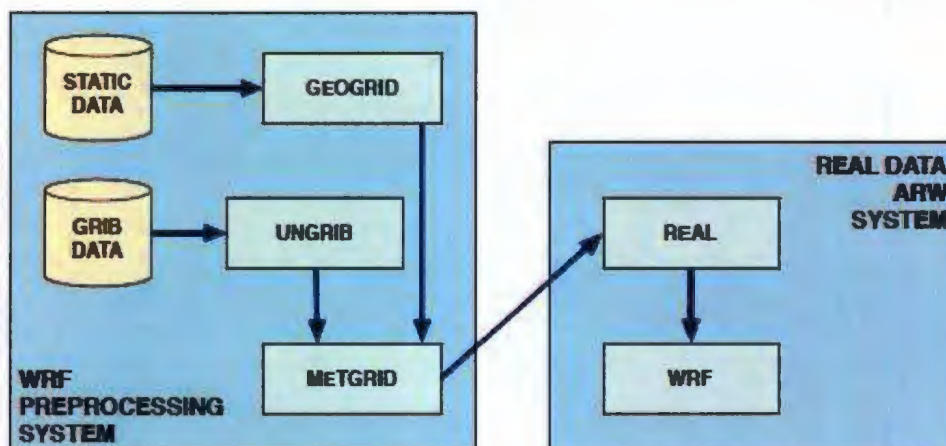


Figure 2.5 Schematic showing the data flow and program components in the WPS, and how the WPS feeds its outputs to the ARW. Letters in the rectangular boxes indicate program names. (Skamarock, et al., 2008)

The WPS is firstly executed. It is responsible for providing input files for real simulations. The WPS consists of three independent programs-- *geogrid*, *ungrib*, and *metgrid*. The “*geogrid*” defines the parameters of model domains (location, number of grid points, grid lengths, and the projection type) and interpolates static data, such as terrain, landuse, and soil types, to the model grids. Meanwhile, the “*ungrib*” de-grips input meteorological fields (u, v, T, q, surface pressure, soil data, snow data, and sea-surface temperature) from GriB-formatted files. Subsequently, the “*metgrid*” horizontally interpolates the meteorological fields extracted by the “*ungrib*” onto the specified domain defined by the

*“geogrid”* and generates input files for real simulations (ARW Version 3 Modeling System User's Guide, 2008). The *“geogrid”* and the *“ungrib”* can be run simultaneously, and the *“metgrid”* is then run to produce files containing three-dimensional meteorological variables and two-dimensional static fields into a suitable format.

At the second step, initial and lateral boundary conditions are created by a pre-processor program (i.e. *“real”* on the Figure 2.5) in the ARW solver. It vertically interpolates a topographically defined reference state in the free atmosphere or extrapolates near the model surface, and finally computes the perturbation fields. A digital low-pass filtering initialization (DFI) might then be applied to the output of the pre-processor before real simulations so as to remove high frequency noise arising from imbalances between mass and wind fields. Two external files respectively representing initial and lateral boundary conditions for real simulations are ultimately obtained. The lateral boundary file consists of meteorological fields-- horizontal velocities, potential temperature, moisture, and geopotential-- at the initial time of the lateral boundary time and their tendencies to the next boundary time along the north, south, east, and west sides of a rectangular grid.

The WRF model (i.e. *“wrf”* on the Figure 2.5) is ultimately run by using the initial and lateral boundary files computed at the second step. In our simulation, the WRF domain (Figure 2.6) covers the Northwest Atlantic Ocean with a center point at (58°N, 47.5°W). The model resolution is 30 km by 30 km in the horizontal and 28 layers in the vertical. The Lambert projection is used. Moreover, the upper boundary of the model is specified as 50 hPa. The model time step is chosen to be 180 s to meet the CFL condition, in terms of the relationship between the grid size and the model time step.

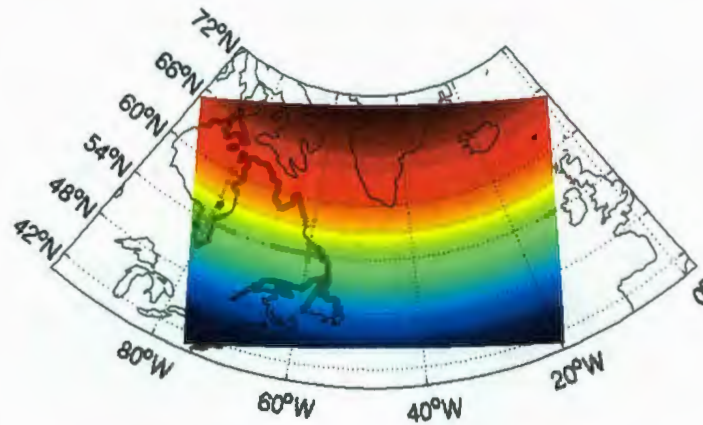


Figure 2.6 The WRF simulation domain.

## 2.2 The Ocean Model

The ocean model used in this study is the Nucleus for European Models of the Ocean modeling system (NEMO, Madec, 2008) coupled with the multilayered sea-ice code Louvain-la-Neuve Ice Model (LIM2) (Fichefet and Morales Maqueda, 1997).

### 2.2.1 Governing equations

The equations of the NEMO model are the incompressible, Boussinesq, thin-shell, hydrostatic primitive equations with the conservation of momentum, mass and energy for the ocean on spherical coordinates.

$$\frac{\partial \mathbf{U}_h}{\partial t} = -[(\nabla \times \mathbf{U}) \times \mathbf{U} + \frac{1}{2} \nabla(U^2)]_h - f \mathbf{k} \times \mathbf{U}_h - \frac{1}{\rho_0} \nabla_h p + \mathbf{D}^u + \mathbf{F}^u \quad (2.2.1)$$

$$\frac{\partial p}{\partial z} = -\rho g \quad (2.2.2)$$

$$\nabla \cdot \mathbf{U} = 0 \quad (2.2.3)$$

$$\frac{\partial T}{\partial t} = -\nabla \cdot (T\mathbf{U}) + D^T + F^T \quad (2.2.4)$$

$$\frac{\partial S}{\partial t} = -\nabla \cdot (S\mathbf{U}) + D^S + F^S \quad (2.2.5)$$

$$\rho = \rho(T, S, p) \quad (2.2.6)$$

Here  $\mathbf{k}$  is the local upward vector to the earth;  $z$  is the vertical coordinate;  $\mathbf{U}$  is the vector velocity,  $\mathbf{U} = \mathbf{U}_h + w\mathbf{k}$  (the subscript  $h$  denotes the local horizontal vector ( $\mathbf{i}, \mathbf{j}$ ) orthogonal to  $\mathbf{k}$ ;  $T$  is the potential temperature;  $S$  is the salinity;  $\rho$  is the *in situ* density;  $\rho_0$  is a reference density;  $p$  is the pressure;  $f$  is the Coriolis acceleration;  $g$  is the gravitational acceleration. In addition,  $\mathbf{D}^U$ ,  $D^T$  and  $D^S$  are the parameterizations of small-scale physics for momentum, temperature and salinity, and  $\mathbf{F}^U$ ,  $F^T$ , and  $F^S$  are surface forcing terms.

The kinematic surface and bottom boundary conditions are

$$\frac{\partial \eta}{\partial t} + u \frac{\partial \eta}{\partial x} + v \frac{\partial \eta}{\partial y} = w \text{ at } z = 0 \quad (2.2.7)$$

$$w = u \frac{\partial H}{\partial x} + v \frac{\partial H}{\partial y} \text{ at } z = -H \quad (2.2.8)$$

The dynamic boundary conditions are

$$\frac{\tau_x^s}{\rho_0} = K \frac{\partial u}{\partial z}, \quad \frac{\tau_y^s}{\rho_0} = K \frac{\partial v}{\partial z}, \text{ at } z = 0 \quad (2.2.9)$$

$$u = v = 0, \text{ at } z = -H \quad (2.2.10)$$

Here  $\eta$  is the height of the sea surface referenced to a given surface ( $z = 0$ ) and  $H$  is the depth of the ocean bottom from the referenced surface. The model allows the ocean exchange momentum, heat, and fresh water with the atmosphere.

A free-slip boundary condition is used at land boundaries. The radiative open boundary conditions (OBC) based on the formulation by Tréguier et al. (2001) and Marchesiello et al. (2001) are defined with constrain of the long-term variability of model quantities at the northern and southern open boundaries by their climatological values.

The discretization of the governing equations is based on the finite difference method. A three-level, leap-frog scheme is used for the temporal discretization, which involves values at the current time step, one time step before and one time step after. The leapfrog scheme is applied in combination with an Asselin time filter (Robert, 1966; Asselin 1972) to control the computational time-splitting noise.

The Arakawa C grid is utilized for the spatial discretization. Temperature, salinity, density, pressure, and horizontal divergence are calculated at the “mass” point or T point. The three components of velocity on each dimension are calculated at u, v, and w points, respectively. Both relative and planetary vorticities are defined at the vorticity point or f point. A central differencing scheme is operated to discretise the primitive equations.

### **2.2.2 Model setup and implementation**

The model is set up by Zhu and Demirov (2010). The model parameters are shown in Table 2.2. The model domain covers the North Atlantic from 7°N to 67°N (Figure 2.7) with  $\frac{1}{4}^\circ$  in longitude and  $\frac{1}{4}^\circ \cdot \cos\phi$  in latitude in the horizontal and 46 levels in the

vertical. This horizontal resolution corresponds to model grid spacing of about 28 km at 7°N and 11 km at 67°N. Vertical grid spacing is irregular with 8-m resolution at the surface and smoothly increasing to 280-m at the bottom. The maximum model depth is 5600 m. The radiative open boundary conditions (OBC) at the northern and southern boundaries are controlled by the Simple Ocean Data Assimilation (SODA) data (Carton et al., 2005). A spectral nudging technique is used in the model (Thompson et al., 2006).

<b>NEMO Parameters</b>	<b>Values</b>
Horizontal resolution	$\frac{1}{4}^{\circ} \times \frac{1}{4}^{\circ} \cos\theta$
Horizontal dimensions	544 × 336
Time step (seconds)	1800
Max. Biharmonic viscosity (m <sup>4</sup> /s)	-1.5E+11
Max. Laplacian diffusivity (m <sup>2</sup> /s)	300

Table 2.2 The NEMO model parameters used in the ocean simulation.

The partial step (Adcroft et al. 1997) method is applied to represent topography. The energy-entropy conserving scheme (Arakawa and Lamb 1981), which conserves total energy for general flow and potential enstrophy for flows with no mass flux divergence is used in the momentum equations. These options were found to give the best performance in simulations of the North Atlantic through the previous studies by Barnier et al. (2006) and Penduff et al. (2007).

The vertical mixing is parameterized by the 1.5 turbulent closure model of Gaspar et al. (1990), adapted to OPA by Blanke and Delecluse (1993). In case of static instability, a viscosity/ diffusivity enhancement of  $10 \text{ m}^2/\text{s}$  is used. A Laplacian lateral isopycnal diffusion on tracers is used ( $300 \text{ m}^2/\text{s}$  at  $7^\circ\text{N}$ , and decreasing poleward proportionally to the grid size), while a horizontal biharmonic viscosity is used for momentum ( $-1.5 \times 10^{11} \text{ m}^4/\text{s}$  at  $7^\circ\text{N}$ , and decreasing poleward as the cube of the grid size).

The model is initialized with climatological temperature and salinity and zero velocities. Initial conditions for temperature and salinity are derived from the World Ocean Atlas 2005 (WOA05) dataset (Locarnini et al., 2006; Antonov et al., 2006) for the North Atlantic and Baltic Sea and from the Mediterranean Data Archaeology and Rescue (MEDAR) dataset (Brankart and Brasseur, 1998) for the Mediterranean Sea. The model is run for 30 years with climatological forcing. After this spin-up period, it is forced with NCEP/WRF forcings as described in the next section.

## **2.3 Experimental Design**

In this study, we discuss results from two model experiments. In the first one, the NEMO model is forced by 6-hourly NCEP/NCAR reanalysis (Kalnay et al., 1996). This experiment is called the Exp\_SPNCEP experiment (Table 2.3). In the second experiment, the NEMO model is forced by fine-resolution atmospheric fields obtained from the WRF model and this run is called the Exp\_SPWRF experiment (Table 2.3).

The WRF model is first run to create fine-resolution atmospheric forcing for the ocean model. The NCEP/NCAR reanalysis (Kalnay et al., 1996) in GriB1 format with a

horizontal resolution of 2.5 degrees provides the initial and lateral boundary conditions for the WRF model. The simulations cover the Northwest Atlantic Ocean (Figure 2.6) and start from 12:00 pm December 31, 1979, and end at 00:00 January 04, 2006. Our first test runs of the WRF model with the chosen parameterizations demonstrated that if it ran for longer than a month, the model solution drifted away from the NCAR/NCAEP reanalysis. In order to overcome this drawback, the WRF model is re-initialized every two days. This period was proved to be optimal for our simulations.

<b>Experiment</b>	<b>Exp_SPNCEP</b>	<b>Exp_SPWRF</b>
precipitation	NCEP	WRF+NCEP*
2-m relative humidity	NCEP	WRF+NCEP
2-m temperature	NCEP	WRF+NCEP
10-m zonal wind stress	NCEP	WRF+NCEP
10-m meridional wind stress	NCEP	WRF+NCEP
10-m wind speed	NCEP	WRF+NCEP
cloud	NCEP	NCEP

Table 2.3 Numerical experiments.

\*(WRF+NCEP means the NEMO model is forced by the WRF outputs over the Northwest Atlantic Ocean (the area inside of the black rectangular in Figure 2.7 and by the NCEP/NCAR reanalysis data over the rest of the North Atlantic Ocean (the area outside of the black rectangular in Figure 2.7).

During these 26 years, the model is integrated for 60 hours, outputs every 6 hours, and re-initialized at 12:00 every two days. For each run, only the last 48-hour outputs are retained and the first 12-hour adjustment is discarded (See Figure 2.8). The WRF high-resolution 6-hourly atmospheric forcing is generated over the Northwest Atlantic Ocean from 00:00 January 1, 1980 to 18:00 January 3, 2006.

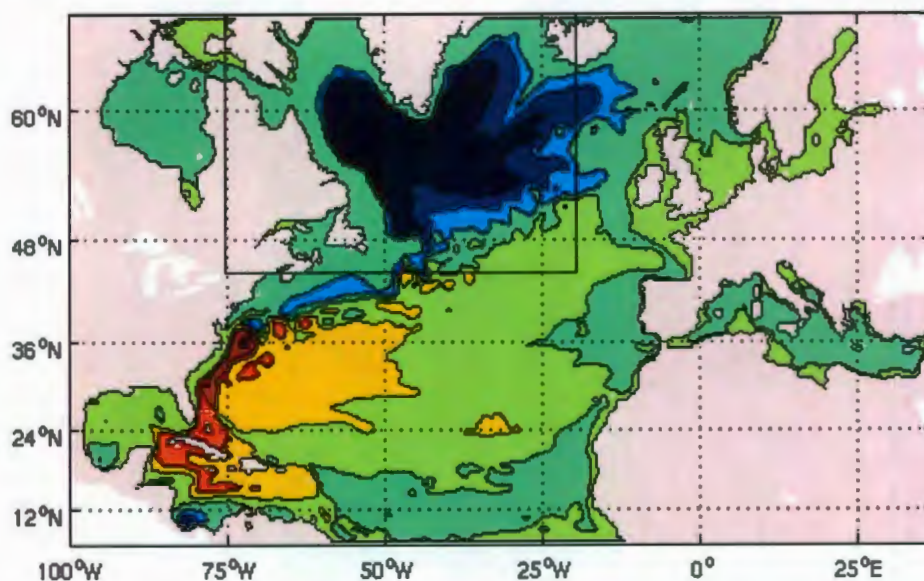


Figure 2.7 The NEMO simulation domain covering the entire North Atlantic Ocean. (Solid color and contours represent barotropic stream function (BSF, Sv) averaged in 2005 from the results of Exp\_SPNCEP)

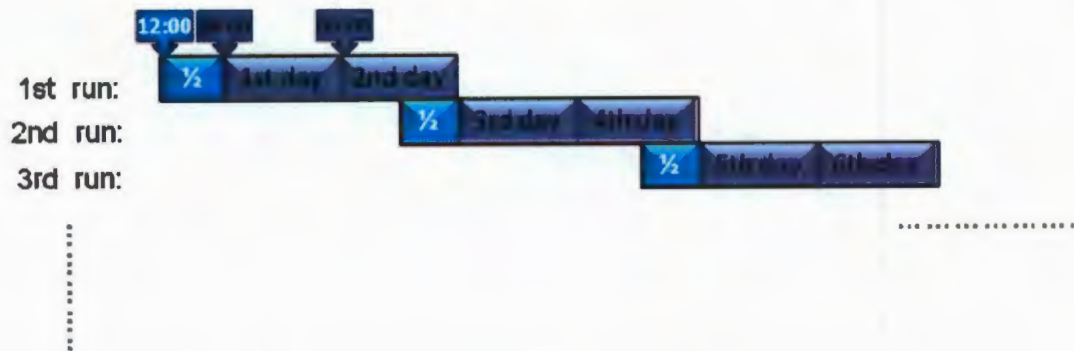


Figure 2.8 A schematic figure of the first three runs of the atmospheric experiment.

(Light blue shows the first 12 hours of each run which is discarded and dark blue shows the last 48 hours of each run which is retained to output.)

The atmospheric forcing fields are interpolated onto the NEMO model mesh. The NEMO model is then forced by the WRF-derived fine-resolution forcing over the Northwest Atlantic (the area inside of the black rectangular in Figure 2.7) and by the NCEP/NCAR reanalysis data (Kalnay et al., 1996) over the rest of the North Atlantic (the area outside of the black rectangular in Figure 2.7).

## **Chapter 3: Model Simulations of Climatological Characteristics and Interannual Variability of Subpolar North Atlantic Atmosphere**

This chapter presents the climatological characteristics and interannual variability of the subpolar atmosphere over the North Atlantic Ocean from two datasets: the NCEP/NCAR reanalysis data (Kalnay et al., 1996) and the WRF-derived data.

(i) The NCEP/NCAR reanalysis data (Kalnay et al., 1996) is produced by a global atmospheric model with the assimilation of observations for the period 1948-present. The data assimilated in the North Atlantic, North America, Europe and Asia include observations from land surface, ship, rawinsonde, and satellites. While these data constrain many variables in the reanalysis, Kalnay et al. (1996) mentioned that the other variables are less influenced by the data assimilation and are computed by the model only. Hence, they conclude that scalar data like precipitation and surface fluxes should be used with caution. Another important aspect for the discussion in this chapter is that NCEP/NCAR reanalysis data (Kalnay et al., 1996) are of coarse resolution of about  $2.5^{\circ} \times 2.5^{\circ}$ . They do not well resolve some weather patterns that are important for the subpolar North Atlantic.

(ii) The WRF-derived data with 30-km resolution is produced by the WRF model that was described in the Chapter 2. The initial and lateral boundary conditions of the WRF model are provided by the NCEP/NCAR reanalysis data (Kalnay et al., 1996). Thus the gross features of the atmospheric flow in the two datasets are the same, and the fine-resolution representation of sub-scale physical processes and orography improves the spatial and temporal atmospheric variability in the WRF.

This chapter discusses the differences in the climatological characteristics and interannual variability over the subpolar North Atlantic Ocean between the two datasets.

### **3.1 Climatological Features of Atmosphere**

Figures 3.1- 3.6 show precipitation, 2-m relative humidity, 2-m air temperature, 10-m zonal wind stress, 10-m meridional wind stress and 10-m wind speed averaged during the winter and summer months of the 26 years (1980-2005) from the two datasets and the differences between the two, respectively. These variables influence the freshwater, heat, and momentum fields of atmosphere over the Northwest Atlantic Ocean. The winter months are January, February, and March (JFM). The summer months are July, August, and September (JAS). Since the NCEP/NCAR reanalysis data has much coarser horizontal resolution than the WRF-derived data, the NCEP/NCAR data looks smoother than the WRF data as expected.

Overall speaking, the patterns of the winter and the summer precipitation (Figure 3.1) in each dataset are very similar. In winter, the NCEP precipitation (Figure 3.1a) has a local maximum amount up to 15 mm along the east coast of Greenland at about 65°N and

about 7 mm along the west coast. In the open ocean, precipitation is around 4 mm with two large centers at (46°N, 40°W) and (60°N, 24°W). The southern Davis Strait, the western Labrador Sea and the central Irminger Sea have lower than 2 mm precipitation, which are relatively less than that over the rest part of the sub-polar North Atlantic Ocean.

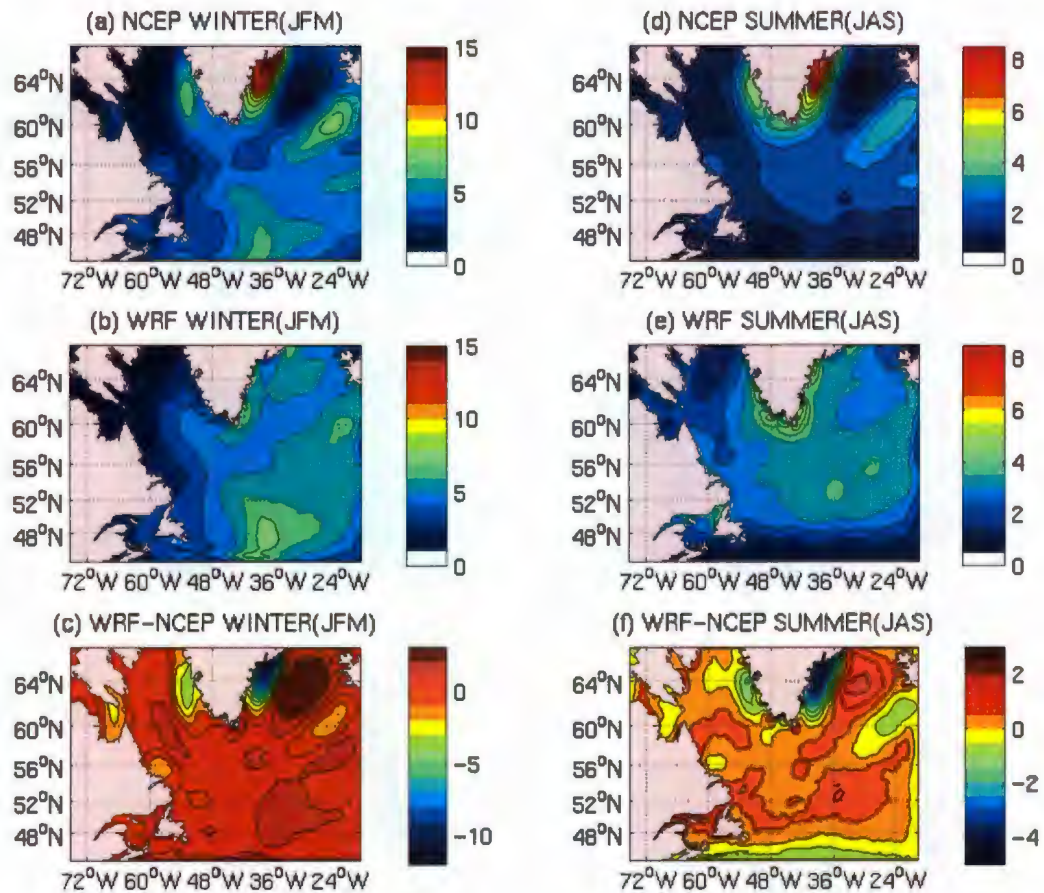


Figure 3.1 Precipitation (mm/day) from the NCEP/NCAR reanalysis data and the WRF outputs averaged in the winter months (JFM) and summer months (JAS) during the whole experimental time (1980-2005) and differences between the two datasets in the two seasons.

The WRF winter precipitation (Figure 3.1b) presents similar features but has also some distinct differences from the NCEP data. Similar to the NCEP features occur over the southern Davis Strait and the western Labrador Sea where precipitation is around 1 mm, less than the rest area of the Northwest Atlantic Ocean. In the western Labrador Sea and the open sea of North Atlantic Ocean, the WRF simulation shows have similar pattern of precipitation to the NCEP data but at larger magnitude. The most evident differences (Figure 3.1c) appear the coastal area of Greenland. The center along the west coast in the NCEP winter precipitation disappears and the maximum area (up to 15 mm) along the east coast in the NCEP is replaced by an area that has approximate amount of 6 mm and a center over the northeast of Cape Farewell. The summer precipitation of the two datasets (Figure 3.1d, e) shows similar features, except over the open ocean south of 50°N. There, the summer precipitations from the both data do not have local maximum centers but areas with precipitation of less than 2 mm. In general, we can conclude that the major differences in the winter and summer precipitations occur along the coastal area of Greenland which also covered by seaice during the cold seasons. In the deep ocean area, precipitation shows similar patterns with higher precipitation in the WRF simulation.

2-m relative humidities from the two datasets (Figure 3.2) display distinct differences in winter as well as in summer. The NCEP winter 2-m relative humidity (Figure 3.2a) has two relatively dry areas over the northern Labrador Sea ( $< 0.6\%$ ) and the central Irminger Sea ( $< 0.7\%$ ) and a large wet area ( $> 0.86\%$ ) over the Northwest Atlantic Ocean with local maximum centers over the coasts of Labrador and Greenland. However, the WRF winter 2-m relative humidity (Figure 3.2b) shows more homogeneous

features than the NCEP data does. It does not have the wet areas in Figure 3-1(a), but a relatively wet areas (about 0.84) over the western Labrador Sea and a dry area (about 0.80) over the rest of sub-polar North Atlantic with a local minimum center at (60°N, 24°W). The driest area in the WRF is still over the northern Davis Strait but has much larger magnitude (around 0.72%) than the NCEP.

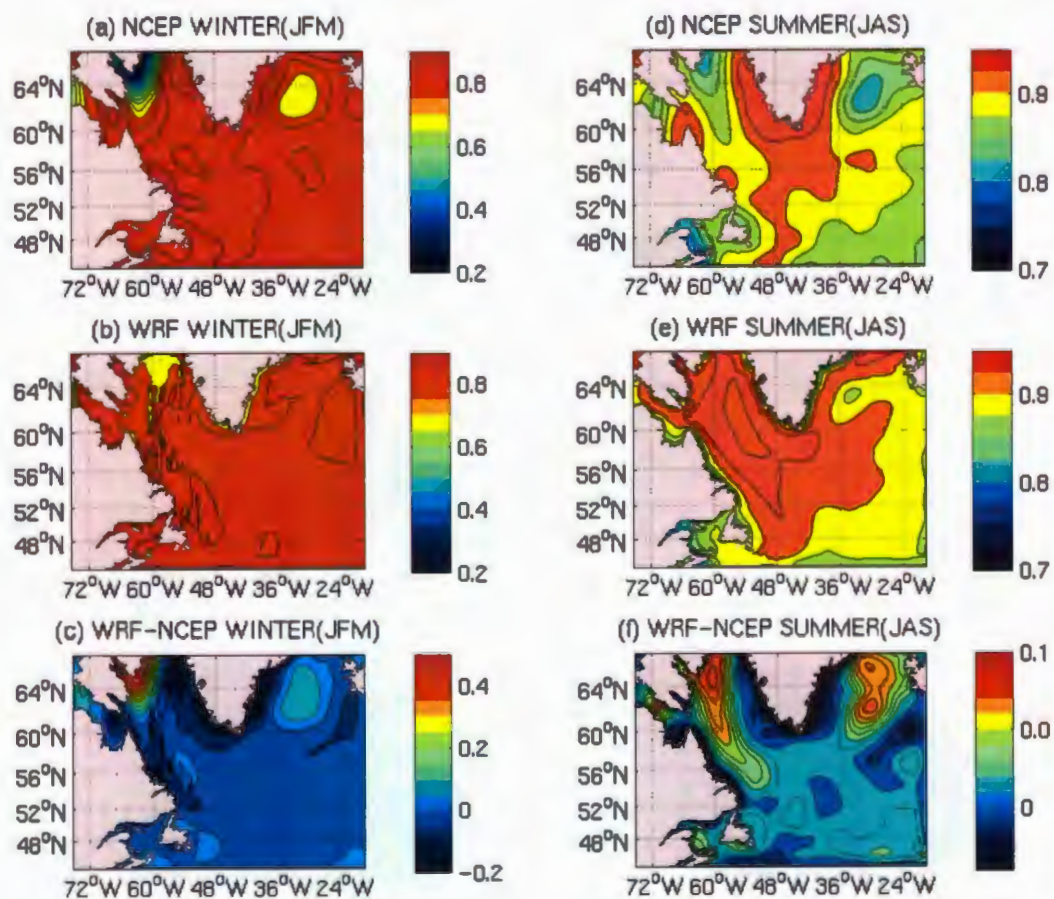


Figure 3.2 Same as Figure 3.1, but for 2-m relative humidity.

The NCEP summer 2-m relative humidity (Figure 3.2d) has similar features to the winter but larger amounts over the driest (0.84%) and wettest (0.94%) areas in the winter season. Over the deep ocean, the NCEP summer 2-m relative humidity shows larger zonal gradient and magnitude than the winter does. The WRF summer 2-m relative humidity (Figure 3.2e) is totally different from the NCEP summer humidity. It distributes wet (0.94%) to dry (0.88%) from west to east with a small dry center (0.92%) over the northern Labrador Sea.

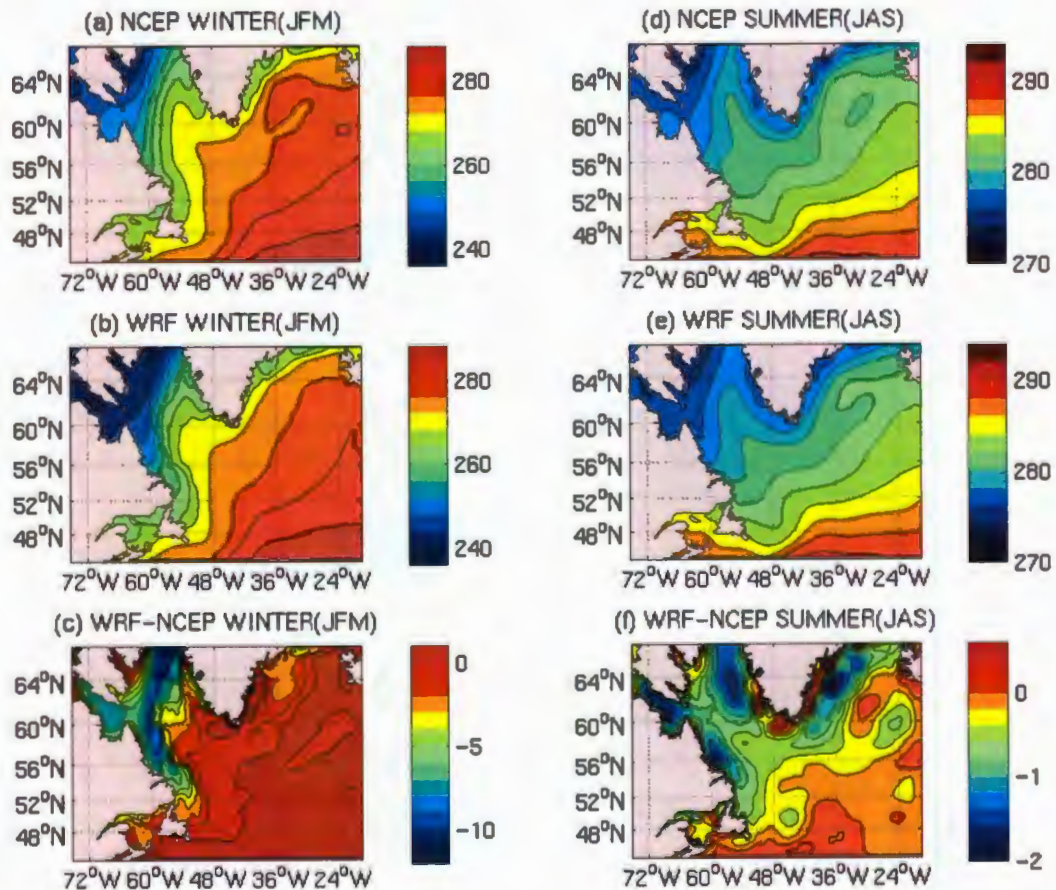


Figure 3.3 Same as Figure 3.1, but for 2-m air temperature (K).

The NCEP and WRF 2-m air temperature fields (Figure 3.3) exhibit similar patterns and values in winter and in summer. The coldest areas (around 240°K in winter and 275°K in summer) in both datasets occur over the Hudson Strait and the coastal line of Baffin Island and the warmest area ( $> 280$  °K in winter and  $> 290$  °K in summer) over the open Northeast Atlantic Ocean. A warm tongue is located over the eastern Labrador Sea and a ridge over the North Atlantic Ocean at the southwest (in winter) and south (in summer) of Iceland. In summer, there is a small cold area along the east coast of Greenland. Besides these similar characteristics in both datasets, there still exist slightly differences. For example, the winter warm tongue (Figure 3.3c) over the eastern Labrador Sea of the WRF outputs is warmer than the NCEP data. Temperature in the coast of Labrador from the WRF data is colder than the NCEP data.

The winter and summer surface zonal wind stress of both the NCEP and the WRF data (Figure 3.4) display a meridional bi-polar pattern along approximate 59°N: eastward (negative) over the north of 59°N excluding the western Labrador Sea and westward (positive) over the south including the western Labrador Sea. In winter, the strongest easterlies are located over the east coast of Greenland at 66°N and the strong western wind stress over the east of Grand Bank. In summer, the strongest easterlies appear southwest coast of Greenland and the east coast of Greenland at 66°N and the strongest westerlies over the deep Northeast Atlantic Ocean. The WRF surface zonal wind stress is, however, not as smooth as that of the NCEP/NCAR reanalysis (Kalnay et al., 1996) data over the coastal area of Greenland, especially in the cold season. Moreover, the WRF

wind flow in both seasons is obviously distorted and much stronger than the NCEP data over the vicinity of Cape Farewell and Kulusuk (65.5°N, 37.2°W).

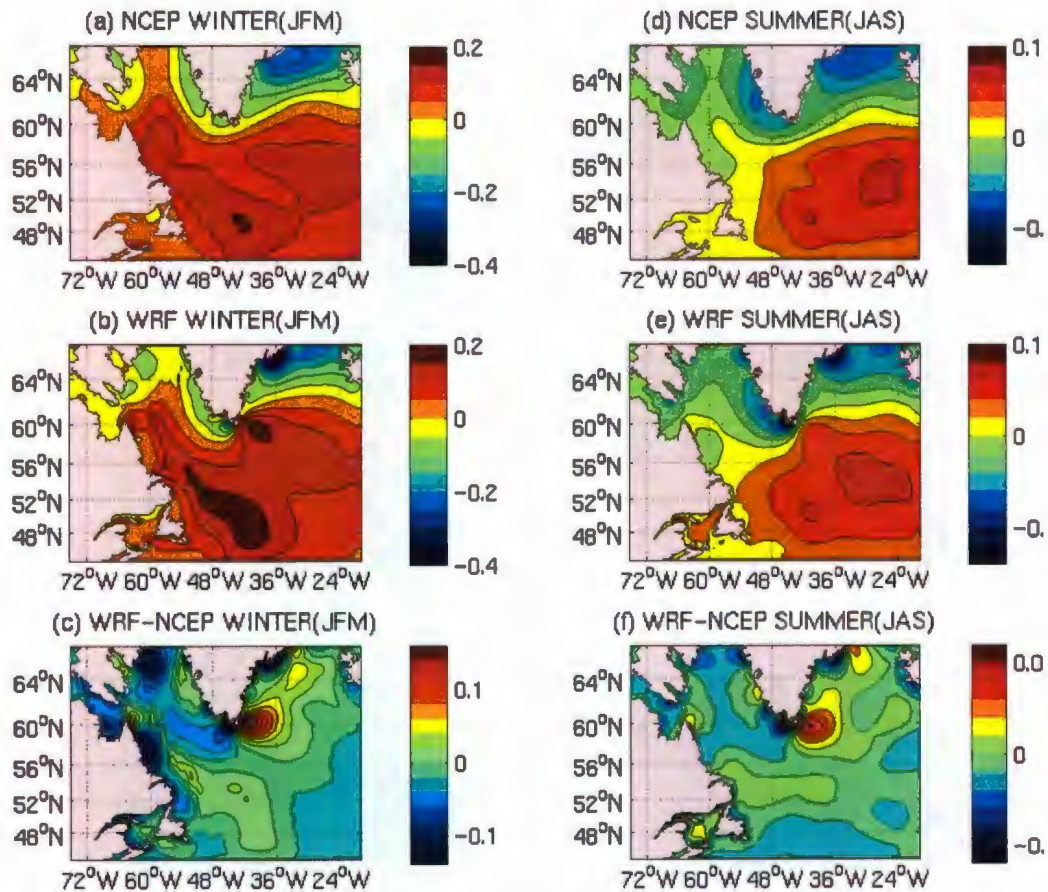


Figure 3.4 Same as Figure 3.1, but for surface zonal wind stress (N/m<sup>2</sup>).

The NCEP and WRF winter surface meridional wind stresses (Figure 3.5) display a slope bi-polar pattern along the northeast-southwest section (approximately from (64°N, 24°W) to (48°N, 54°W)). In winter (Figure 3.5a, b), the NCEP and WRF northerlies blow over the north of the slope, and the southerlies blow over the south. The strong northerlies

appear over the east coast of Greenland and the northern Labrador Sea, and the strongest southerlies in the two data exist over the deep ocean southwest of Iceland.

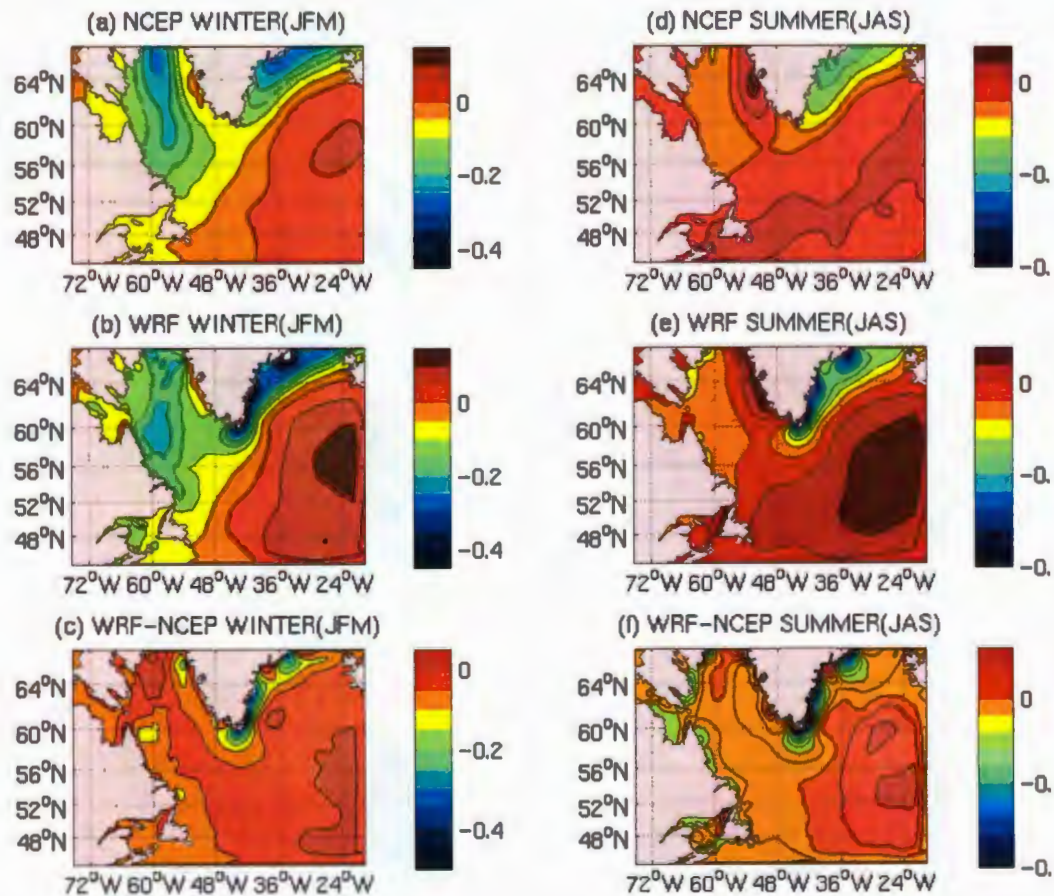


Figure 3.5 Same as Figure 3.1, but for surface meridional wind stress ( $N/m^2$ ).

The NCEP and WRF summer surface meridional wind stress (Figure 3.5d, e) is positive over most parts of the sub-polar North Atlantic Ocean except the western Labrador Sea and the east coast of Greenland. The strongest southerlies occur over the Northeast Atlantic at the south of Iceland and the west coast of Greenland; the strongest northerlies over the east coast of Greenland. The peak southerlies and northerlies of the WRF data in

both seasons are larger than the corresponding values of the NCEP data. In addition, the WRF flow is distorted over the surrounding region of Cape Farewell.

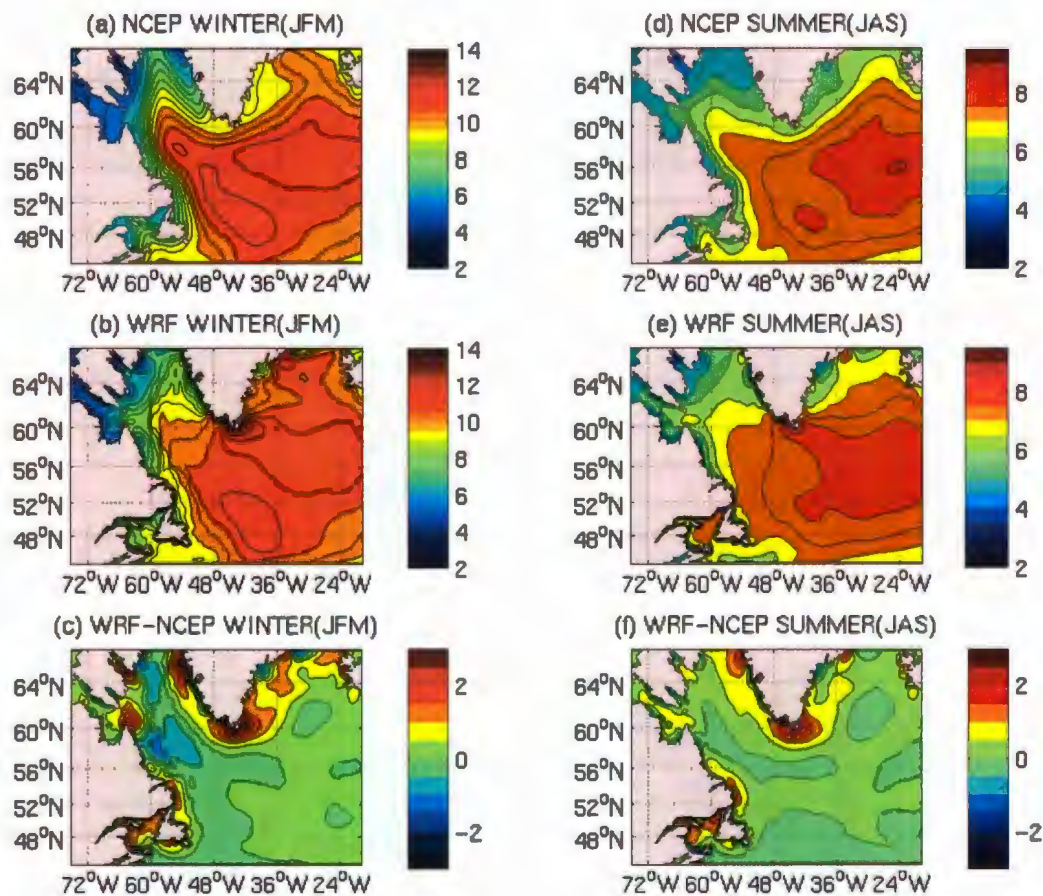


Figure 3.6 Same as Figure 3.1, but for 10-m wind speed (m/s).

The last variable compared is winter and summer mean 10-m wind speed (Figure 3.6). For each data, 10-m wind speed in winter is overall larger than it in summer over the sub-polar North Atlantic Ocean. In winter, 10-m wind speeds exceed 10 m/s over the most parts of the North Atlantic – the central Labrador Sea, the Irminger Sea, the open

North Atlantic Ocean, while they are less than 9 m/s over the entire region in summer. The peak wind speed ( $>12$  m/s in winter and  $>7.5$  m/s in summer) occurs the open North Atlantic Ocean. Like the two components of wind stress, the WRF wind speed in both seasons exhibits distortion near the coastline of Greenland and reaches a peak over Cape Farewell. These features are absent in the NCEP data. Additionally, peak winds in the WRF data are larger than those in the NCEP data.

### **3.2 Dominant Modes of Atmospheric Variability**

Here, we examine the dominant patterns of atmospheric fields during the winter season (JFM) from 1980 to 2005. We focus on winter only because the Greenland tip jets over the subpolar Atlantic and the deep convection in Labrador Sea are the most common phenomena in winter (Moore, 2003). The Empirical orthogonal function (EOF) method is used to extract the dominant patterns of atmospheric forcing fields and comparisons between the corresponding patterns in the NCEP/NCAR reanalysis data and the WRF-derived data are then done.

The EOF analysis is a commonly-used method to find the spatial patterns of variability, their time variation, and measures the importance of each pattern of a scalar field (Bjornsson and Venegas, 1997). The EOF analysis extracts spatial patterns and time variation. We will refer to the patterns as the EOFs and the time series as principal components (PCs).

Table 3.1 lists the variances of the two leading modes of the total variance of each atmospheric field from the two datasets, which indicate how important the first two leading modes are.

Diagnostic	EOF1 (%)		EOF2 (%)	
	NCEP	WRF	NCEP	WRF
Precipitation	34.23	27.65	19.49	21.47
2-m relative humidity	72.10	35.21	9.98	20.38
2-m temperature	80.52	78.24	7.40	6.68
10-m zonal wind stress	53.23	54.63	31.38	30.06
10-m meridional wind stress	34.52	35.69	29.25	28.31
10-m wind speed	40.22	38.35	21.04	22.30

Table 3.1 Variances of the first and second EOF spatial patterns of atmospheric fields averaged in the winter months (JFM) during the 26 years from the NCEP/NCAR reanalysis data and the WRF outputs.

The spatial patterns (EOF1 and EOF2) and the temporal variation (PC1 and PC2) of the first two leading precipitation modes from the two datasets are shown in Figure 3.7 and 3.8. For the NCEP winter precipitation, the two leading EOF modes together account for 53.72% of the total precipitation variance. They individually explain 34.23% and 19.49% of the variance (see Table 3.1). Nearly, the two leading EOF modes of the WRF winter precipitation respectively explain 27.65% and 21.47% of the total variance, i.e. together 49.12% of the variance.

In the NCEP winter precipitation, the EOF1 (Figure 3.7a) exhibits an out-of-phase relationship between the western and eastern coast of Greenland at about 64°N and also another out-of-phase relationship between the Labrador Sea and the open sub-polar northeastern Atlantic Ocean. In the WRF winter precipitation, the EOF1 (Figure 3.7b) displays the similar out-of-phase between the Labrador Sea and the open sub-polar northeastern Atlantic Ocean, and an in-phase relationship between the western and eastern coastal Greenland.

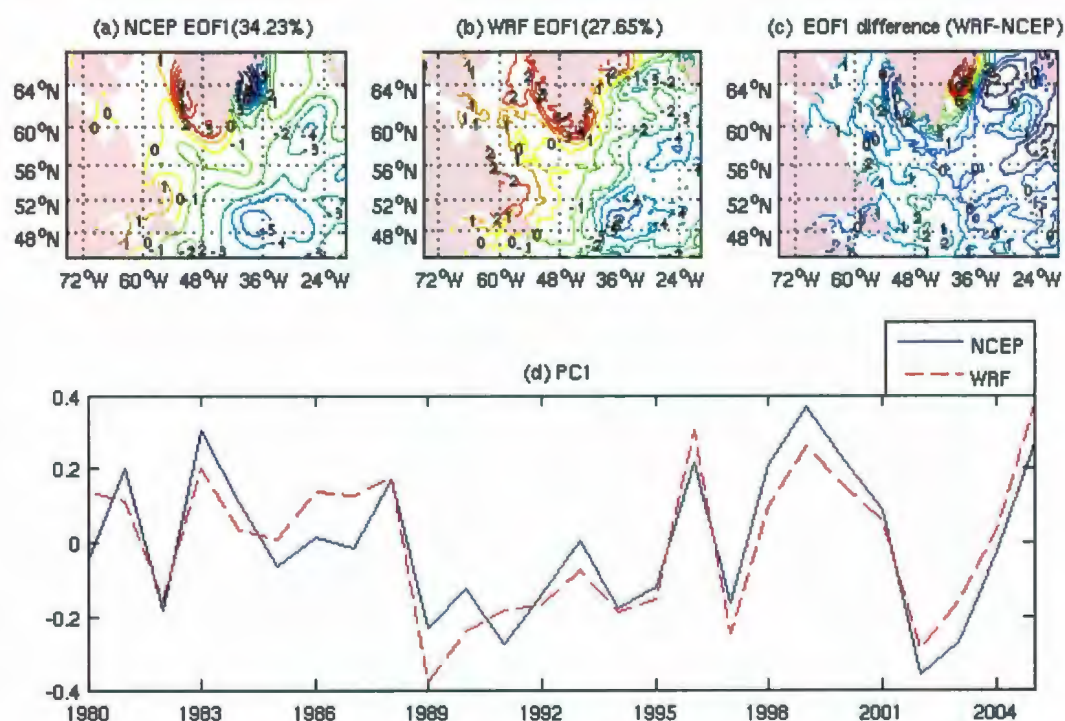


Figure 3.7 The first EOF mode of precipitation averaged in the winter months (JFM) during the 26 years from the NCEP/NCAR reanalysis data and the WRF

outputs.

At the southernmost tip of Greenland, the WRF winter precipitation EOF1 shows a local positive center which is not presented in the NCEP precipitation EOF1. The time series (PC1) (Figure 3.7d) associated with this spatial pattern is dominated by a mixture of inter-annual and decadal variation. Two PC1s are significantly correlated with correlation coefficient of 0.88. The WRF PC1 well captures the main variability displayed by the NCEP PC1, although it has differences in individual years. Before 1988, the PC1s from the both datasets are predominantly at a positive stage; between 1989 and 1995, the PC1 at negative stage; after the year of 1996, the PC1 fluctuates with larger amplitudes with period of 5-6 years.

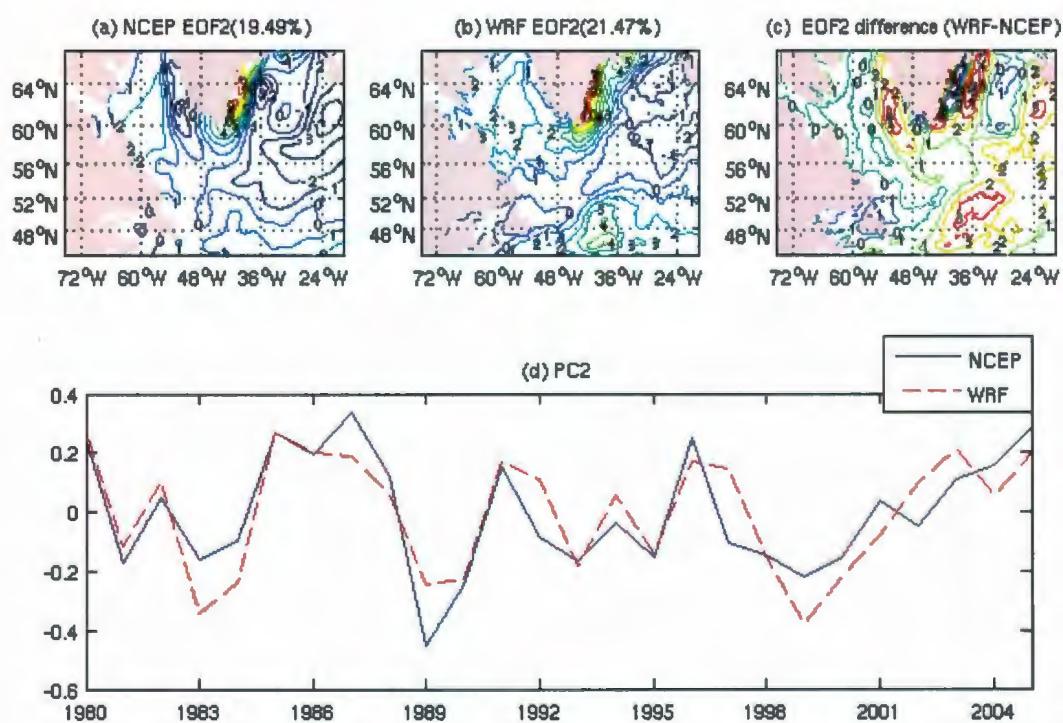


Figure 3.8 The second EOF mode of precipitation averaged in the winter months (JFM) during the 26 years from the NCEP/NCAR reanalysis data and the WRF outputs.

The EOF2 of the NCEP winter precipitation (Figure 3.8a) shows an out-of-phase relationship between the western and eastern coastal Greenland. This relationship is more asymmetric than the EOF1 (Figure 3.7a) with the positive center along the eastern coast stronger than the negative center along the western coast. There is a positive area over the Labrador Sea, a large negative area over the Irminger Sea-- the north of 52°N, and a positive area over the south of 52°N. For the WRF precipitation, the EOF2 (Figure 3.8b) has only a positive center along eastern coastal Greenland and reproduces the positive area in the Labrador Sea, the negative area with a weaker center in the Irminger Sea and the positive area with a stronger center south of 52°N. The time series (PC2, Figure 3.8d) associated with EOF2 mainly represents inter-annual variation. The correlation coefficient of two PC2 is 0.83 with confidence level above 99.9%. The WRF PC2 catches the dominant trend of the NCEP PC2 in spite of differences in individual years.

The winter 2-m relative humidity of the WRF data is the least similar field to that of the NCEP data, both the pattern and the magnitude. The two leading modes of the WRF winter 2-m relative humidity individually account for 35.21% and 20.38% of the total variance, compared with 72.10% and 9.98% of the corresponding values from the NCEP winter 2-m relative humidity (see Table 3.1). The spatial patterns (EOF1 and EOF2) and the temporal variation (PC1 and PC2) associated with the NCEP and WRF winter 2-m relative humidity modes are shown on Figure 3.9 and 3.10.

The main feature of the NCEP winter 2-m relative humidity EOF1 (Figure 3.9a) is the coexistence of a strong positive center oriented almost south-north over south of the Davis Strait and the northern Labrador Sea and a much weak negative area over the rest

of the sub-polar North Atlantic Ocean. The WRF winter 2-m relative humidity EOF1 (Figure 3.9b) does not show either the strong positive area or the weak negative area in the NCEP EOF1, but a weak, positive area over the entire region. The time series associated with this mode (PC1) (Figure 3.9d) of the WRF has a correlation coefficient of 0.60 with the NCEP PC1, with confidence level above 99%. The WRF PC1 more or less captures the decadal variability in the NCEP PC1. After the year 1995, the WRF PC1 fluctuates more rapidly than the NCEP PC1 does.

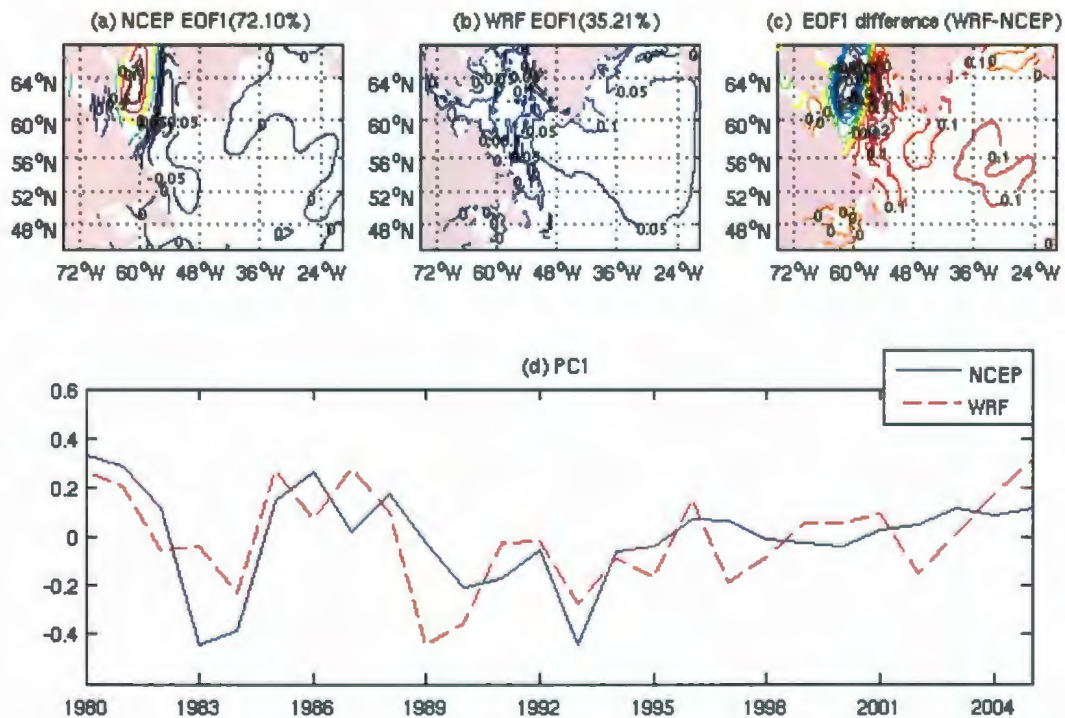


Figure 3.9 The first EOF mode of 2-m relative humidity averaged in the winter months (JFM) during the 26 years from the NCEP/NCAR reanalysis data and the WRF outputs.

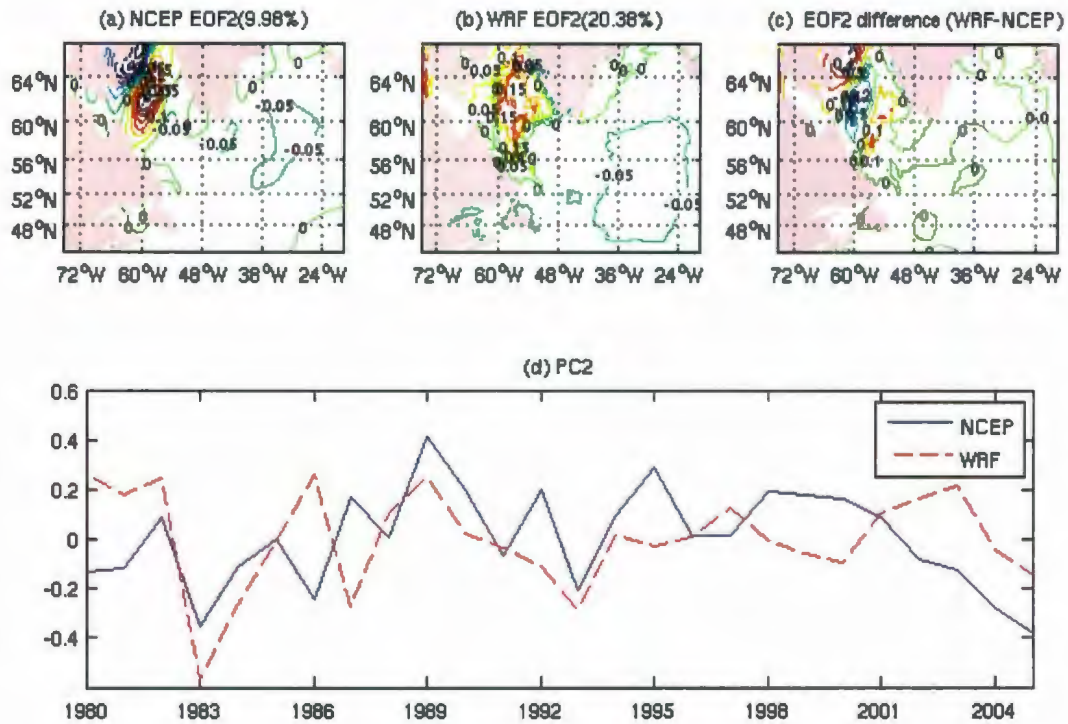


Figure 3.10 The second EOF mode of 2-m relative humidity averaged in the winter months (JFM) during the 26 years from the NCEP/NCAR reanalysis data and the WRF outputs.

The second mode (EOF2) of the NCEP winter 2-m relative humidity (Figure 3.10a) exhibits a strong positive center over the central Davis Strait and northern Labrador Sea and this positive area is surrounded by negative areas along the western Davis Strait, the southeastern Labrador Sea and the open ocean. Although the WRF winter 2-m relative humidity EOF2 (Figure 3.10b) misses the small negative area along the western Davis Strait in the NCEP EOF2, it still has the positive and the other negative areas in the NCEP EOF2. The positive area in the WRF EOF2, which is weaker than that in the NCEP EOF2 extends to the west coast of Greenland. For the time variation associated with this mode

(Figure 3.10d), the PC2 of the WRF data is not quite similar to that of the NCEP data with discrepancies in most years. The correlation coefficient of the two PC1 is only 0.24 with confidence level below 90%.

The EOFs and PCs of the two leading modes of the NCEP and WRF winter 2-m temperatures are shown on Figure 3.11 and 3.12. The two leading modes of the NCEP winter 2-m temperature account for 80.52% and 7.40% of the total variance, respectively, and the two leading modes of the WRF severally account for 78.24% and 6.68% of the total variance.

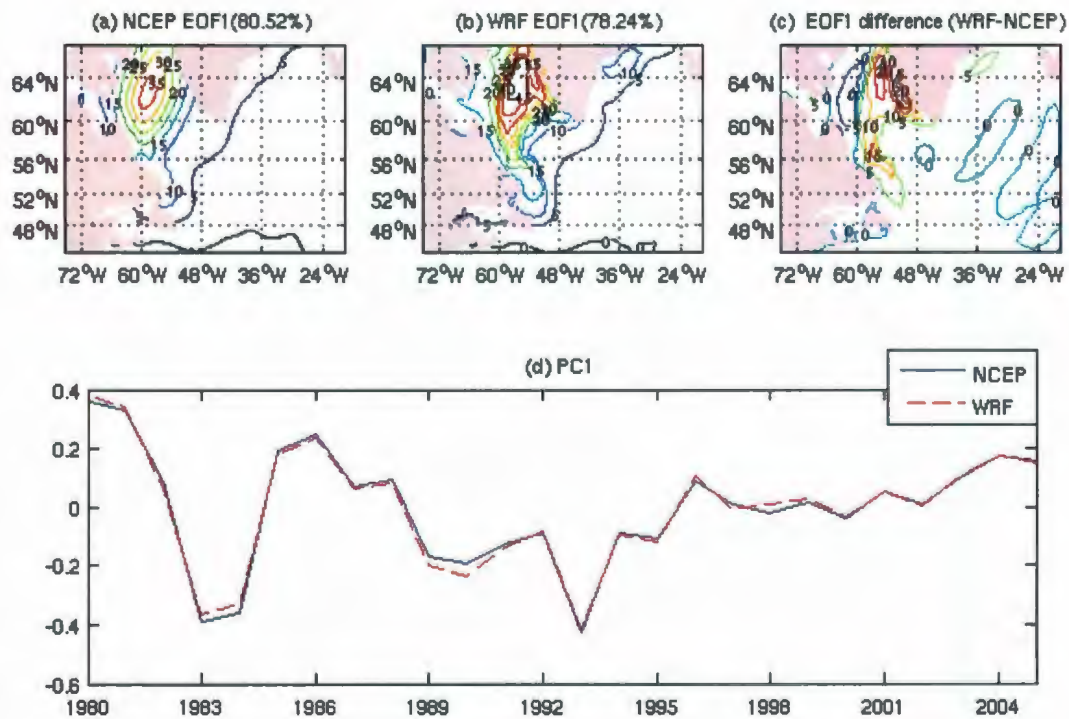


Figure 3.11 The first EOF mode of 2-m air temperature averaged in the winter months (JFM) during the 26 years from the NCEP/NCAR reanalysis data and the WRF outputs.

The EOF1 of the NCEP winter 2-m temperature (Figure 3.11a) displays a strong positive center over south of the Davis Strait. Similarly, the WRF winter 2-m temperature EOF1 (Figure 3.11b) shows the same pattern as the NCEP EOF1. The positive area of the WRF EOF1 has a larger value at its center than that of the NCEP and it extends along the Labrador coast and the west coast of Greenland. Compared with the NCEP EOF1, the WRF EOF1 is larger over the west coast of Greenland and the northwestern Labrador Sea, but smaller over the southern Davis Strait. The PC1s of two datasets are almost identical. The lowest temperature in the 26 years occurs in the year of 1983 and 1993.

Comparing the PC1s with the approximation of area mean air temperature anomaly (Nahed, 2007), the PC1s show the similar variability to the air temperature anomaly: high values in 1980, 1986 and 2004, and low values in 1983 and 1993. The EOF1s has similar pattern to the first and second Canonical correlation patterns for air temperature over the Labrador Sea. This indicates the first mode of winter 2-m air temperature is predominated by the NAO and East Atlantic (EA) pattern.

The second spatial pattern (EOF2, Figure 3.12(a), (b)) of the NCEP and WRF 2-m temperature both display a positive area over south of the Davis Strait with a center along the west coast of Greenland and a negative area over the rest of the northwestern Atlantic with a center along the coastal Labrador and Newfoundland. The WRF EOF2 has stronger positive and negative centers over those areas than the NCEP EOF2 does. The WRF PC2 has similar variability to the NCEP PC2. The correlation coefficient of them is 0.96. Both of them are in a positive status during 1985- 1996.

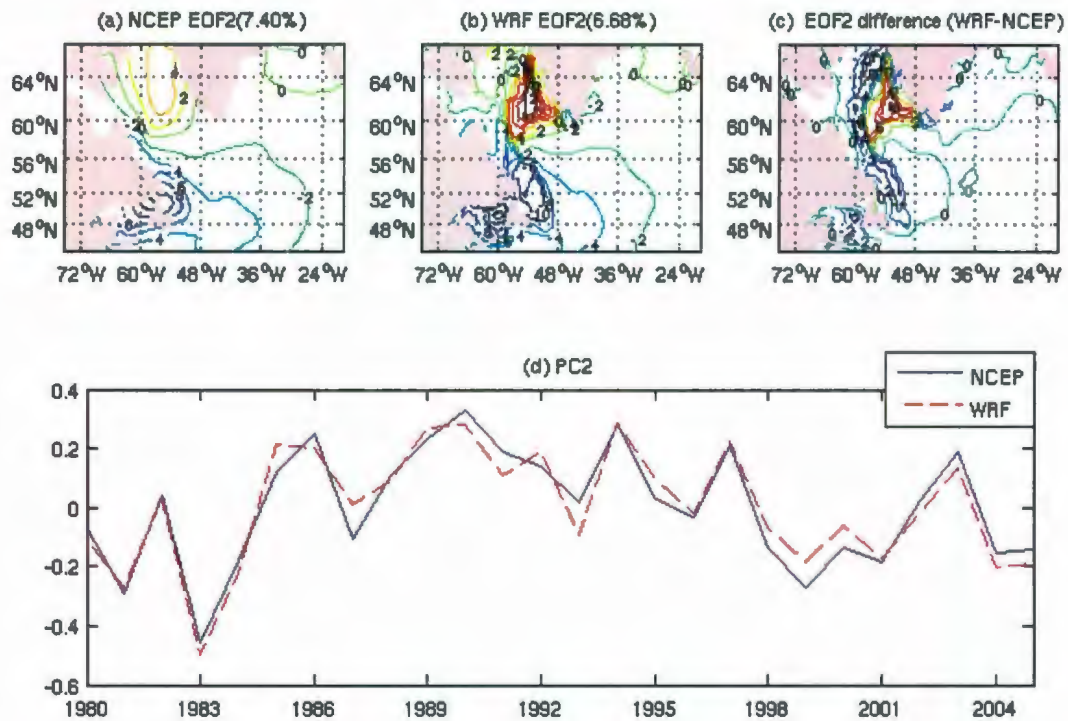


Figure 3.12 The second EOF mode of 2-m air temperature averaged in the winter months (JFM) during the 26 years from the NCEP/NCAR reanalysis data and the WRF outputs.

Figure 3.13 and 3.14 respectively show the first and second modes of the NCEP and WRF winter surface zonal wind stress. The two modes together explain 84.61% of the total variance in the NCEP data and 84.69% in the WRF data.

The EOF1 of the NCEP winter surface zonal wind stress (Figure 3.13a) is covered largely by a west-east-oriented, 20° - wide negative zone with a maximum negative center at about (56°N, 20°W) and a small positive area over the southern Denmark Strait. The EOF1 of the WRF winter surface zonal wind stress (Figure 3.13b) likewise has a predominant negative area over the most sub-polar North Atlantic Ocean. They are,

however, dissimilar to each other over the coasts of Greenland and Labrador. The maximum negative center in the WRF data exists over the southernmost tip of Greenland, not at (56°N, 20°W) in the NCEP data. The WRF flow along the western and eastern coast of Greenland is distorted. This distortion which does not display on the NCEP EOF1 results from the high topography of Greenland. The NCEP and WRF PC1s (Figure 3.13d) have almost exactly the same variability with correlation coefficient of 0.99. They are in positive phase during 1984-1988 and 2001-2005 and in negative phase during 1988-2000.

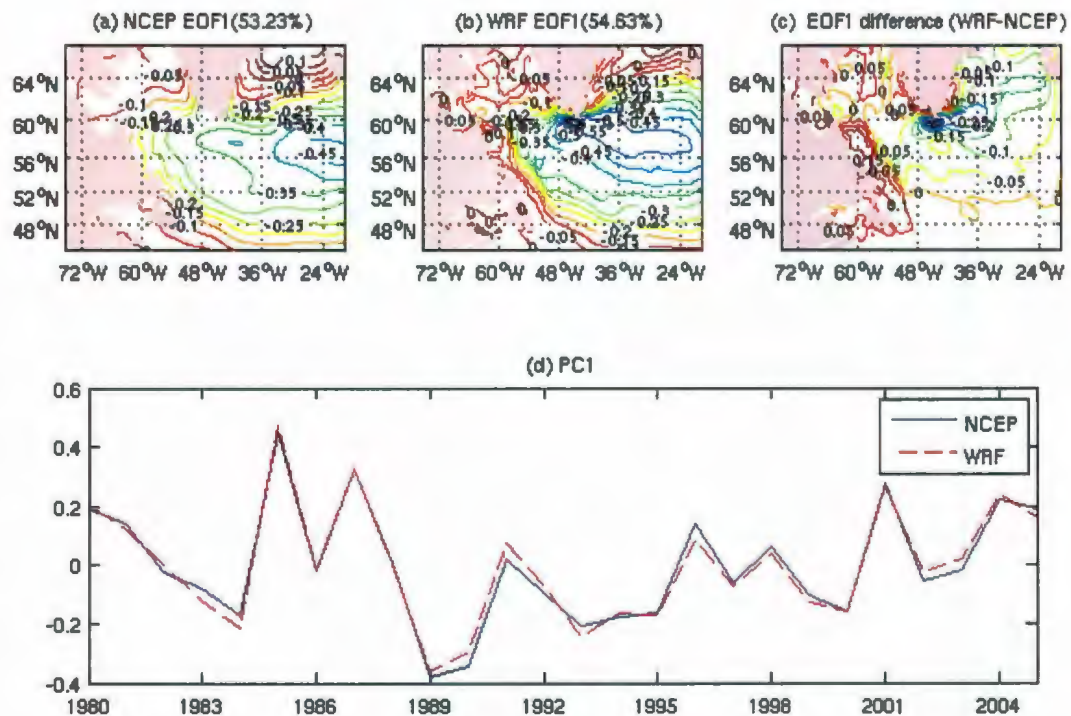


Figure 3.13 The first EOF mode of surface zonal wind stress averaged in the winter months (JFM) during the 26 years from the NCEP/NCAR reanalysis data and the WRF outputs.

The EOF2 of the NCEP winter surface zonal wind stress (Figure 3.14a) presents an out-of-phase relationship between the south and north of about 54°-56°N. The positive and negative centers are located at the Irminger Sea and (48°N, 40°W) in the open North Atlantic, respectively. This out-of-phase pattern also appears in the EOF2 of the WRF surface zonal wind stress (Figure 3.14b). At the same time, the positive area has more than one center at the Irminger Sea. It has a stronger center at Cape Farewell. PC2 (Figure 3.14d) shows inter-annual variability of winter surface zonal wind stress. The WRF PC2 follows exactly the variation of the NCEP PC2 and the correlation coefficient of them is about 0.99.

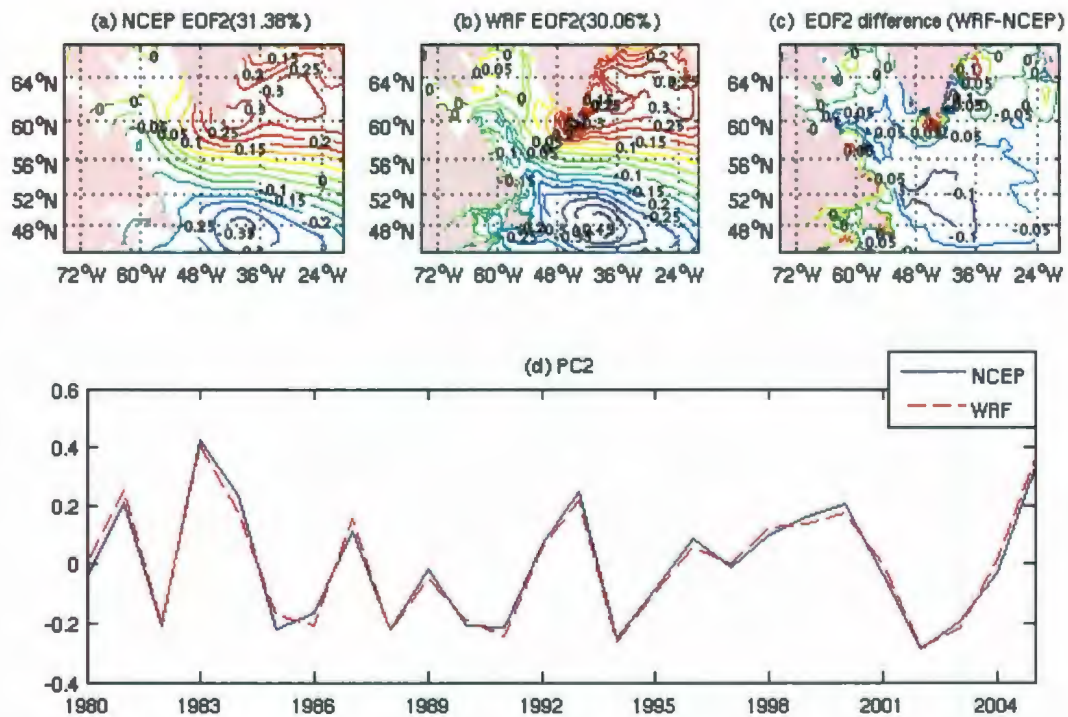


Figure 3.14 The second EOF mode of surface zonal wind stress averaged in the winter months (JFM) during the 26 years from the NCEP/NCAR reanalysis data and the WRF outputs.

Figure 3.15 and 3.16 show the first and second modes of the winter surface meridional wind stress, respectively. The two leading modes of the NCEP winter surface meridional wind stress together account for 63.77% of the total variance, and the two modes of the WRF data explain 64%.

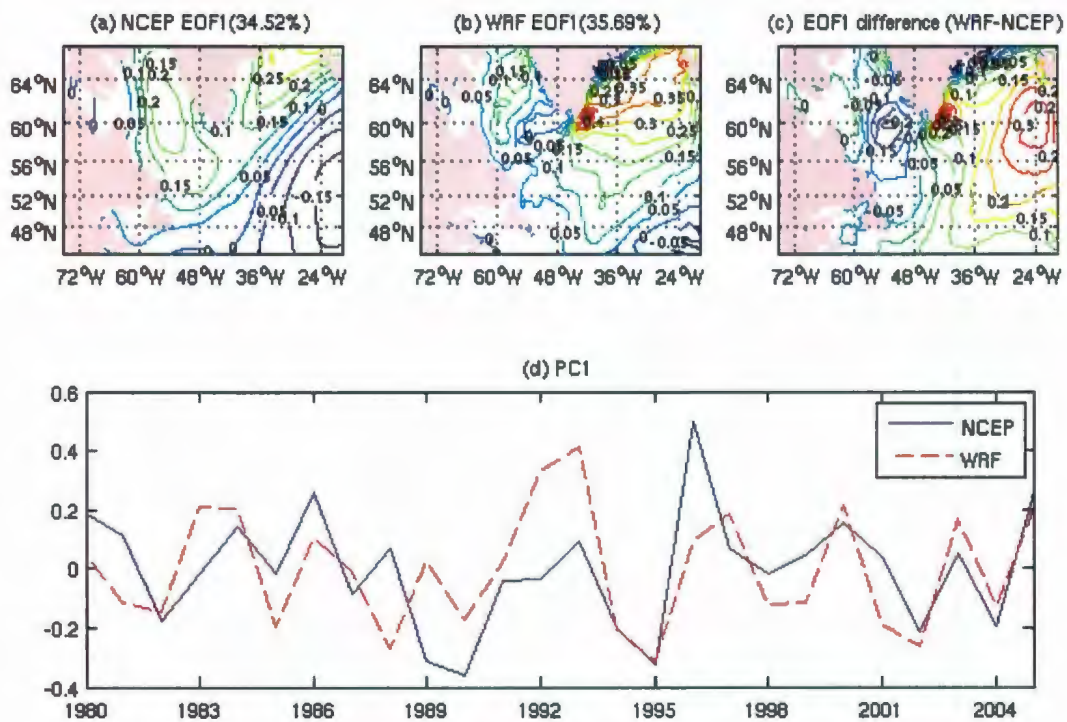


Figure 3.15 The first EOF mode of surface meridional wind stress averaged in the winter months (JFM) during the 26 years from the NCEP/NCAR reanalysis data and the WRF outputs.

The EOF1 of the NCEP winter surface meridional wind stress (Figure 3.15a) shows two positive areas over the Labrador and Irminger Seas and a negative area over the rest

of sub-polar North Atlantic Ocean. The positive centers are located over the northern Labrador Sea and the southern Denmark Strait. For the WRF winter surface meridional wind stress, EOF1 (Figure 3.15b) displays the similar pattern; however, the negative area shrinks southeastwards and the positive areas have another center at Cape Farewell. Although the PC1 of winter surface meridional wind stress (Figure 3.15d) of the WRF data is not identical to that of the NCEP data, the correlation coefficient of them is 0.50 still with confidence level of 99%. However, in 1993, the WRF PC1 is much larger (positive) than the NCEP PC1; and in 1996, the WRF PC1 is smaller (positive).

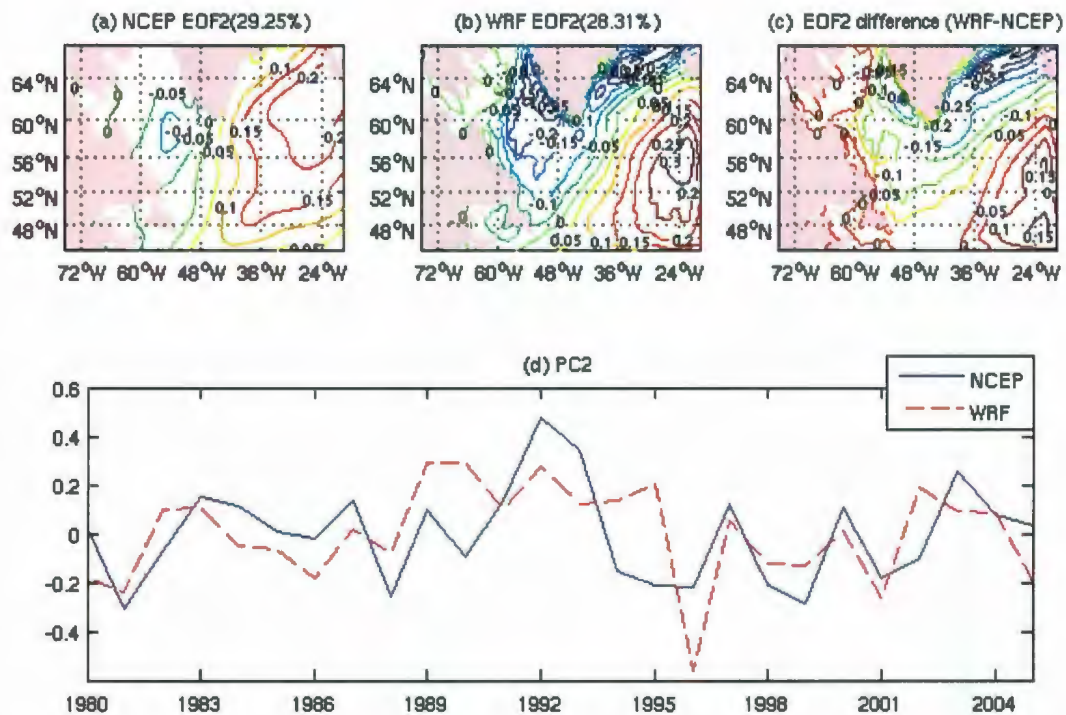


Figure 3.16 The second EOF mode of surface meridional wind stress averaged in the winter months (JFM) during the 26 years from the NCEP/NCAR reanalysis data and the WRF outputs.

The EOF2 of the NCEP winter surface meridional wind stress (Figure 3.16a) has an almost zonal out-of-phase relationship between the west and east of 48°-50°W with a negative center at the central Labrador Sea and a positive center southwest of Iceland. The interface of the bi-polar pattern in the EOF2 of the WRF winter surface meridional wind stress (Figure 3.16b) is not zonal but somewhat inclines northeastward-southwestward. Thus the negative area in the WRF EOF2 extends to the eastern coast of Greenland and Denmark Strait with another center over the southeastern coast of Greenland. Furthermore, the positive area narrows its influence to the North Atlantic south of Iceland. For the corresponding time series, the correlation coefficient of two PC2s is about 0.47 with confidence level of 95%. Basically, the WRF PC2 follows the fluctuation of the NCEP PC2 during 1980-1989 and 1997-2005, but quite differs from the NCEP PC2 during 1990-1996.

The two leading modes of the NCEP and WRF winter 10-m wind speed (Figure 3.17 and 3.18) explain 61.26% and 60.65% of the total variance in the NCEP and WRF data, respectively.

For the NCEP 10-m wind speed, EOF1 (Figure 3.17a) shows positive values only over the southern Davis Strait and the east coast of Greenland and a large negative area over the rest of sub-polar North Atlantic Ocean. The peak negative center is located in the east of Newfoundland. For the WRF 10-m wind speed, EOF1 (Figure 3.17b) presents the similar positive and negative areas. However, the positive area not only has stronger center but extends to the coast of Labrador. In addition, the negative flow is distorted when reaching the southern Greenland. This distortion is not presented in the NCEP

EOF1. The PC1s of the NCEP and the WRF data (Figure 3.17d) have similar variability during the most of the period except for small discrepancy in a few individual years. The correlation coefficient of them is 0.92 with confidence level of 99.9%.

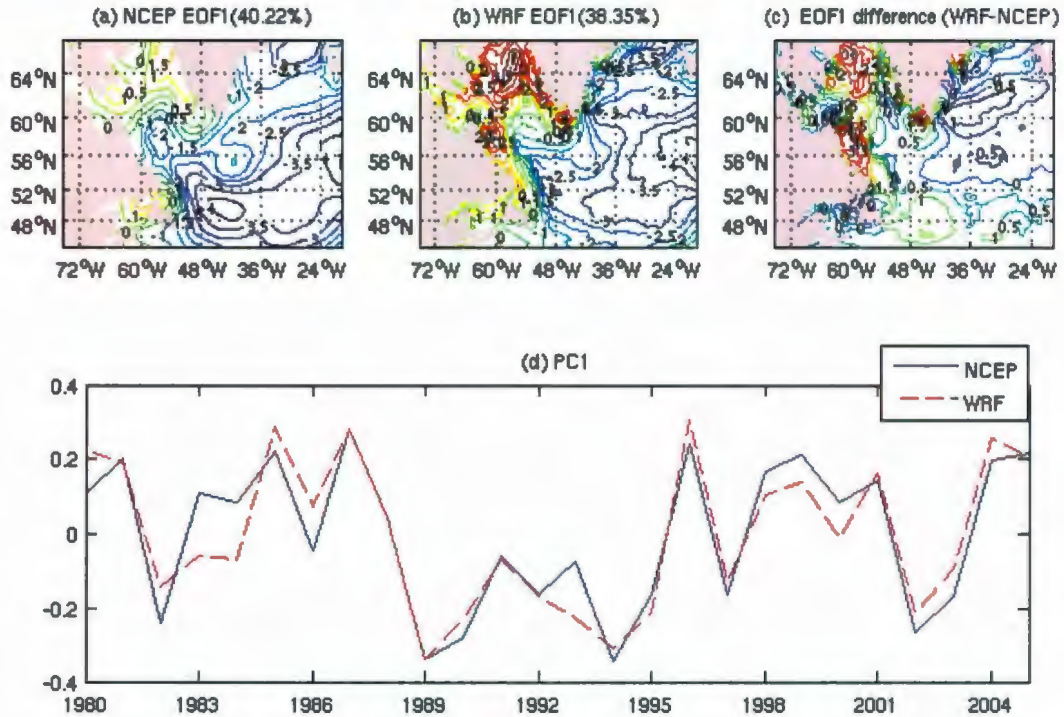


Figure 3.17 The first EOF mode of 10-m wind speed averaged in the winter months (JFM) during the 26 years from the NCEP/NCAR reanalysis data and the WRF outputs.

The EOF2 of the NCEP winter 10-m wind speed (Figure 3.18a) has a positive area over the Labrador Sea, the North Atlantic southeast of Newfoundland and the Denmark Strait, and a negative area over the eastern Irminger Sea and the North Atlantic southwest of Iceland. The positive and negative areas are located at the same regions in the EOF2 of

the WRF winter 10-m wind speed (Figure 3.19b). However, the positive and negative centers are somewhat remote between the two data. Moreover, the WRF EOF2 is smaller than the NCEP over the northwestern Labrador Sea and western coast of Greenland (see Figure 3.18c). The PC2s of the two data (Figure 3.18d) have similar variability to each other with correlation coefficient of 0.91.

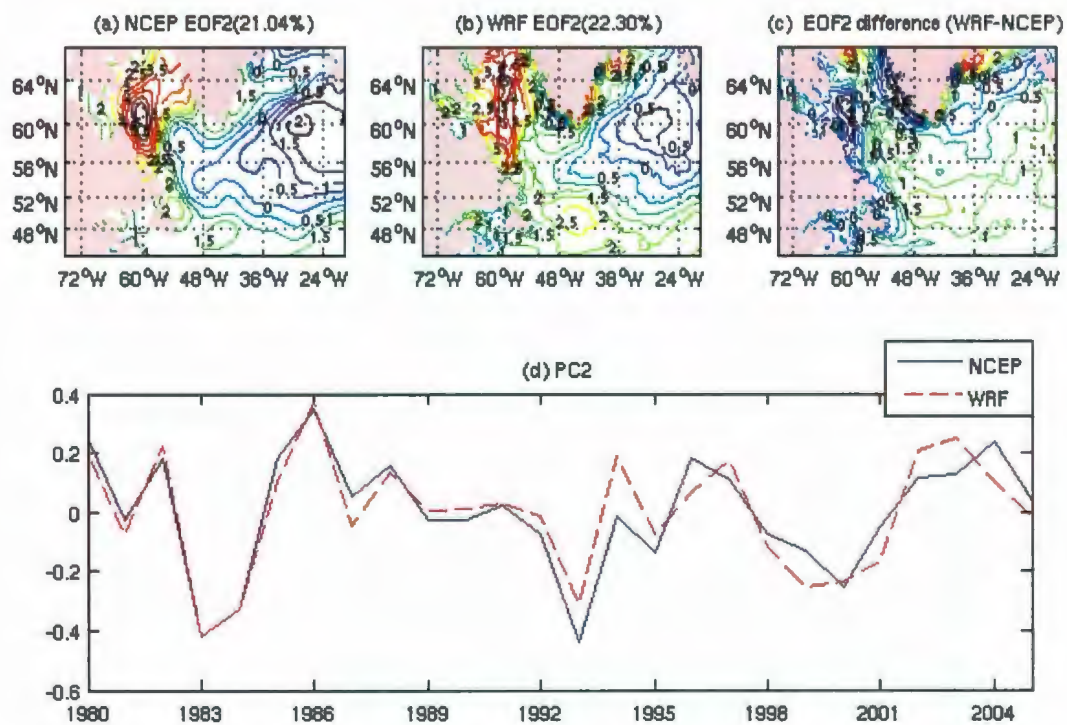


Figure 3.18 The second EOF mode of 10-m wind speed averaged in the winter months (JFM) during the 26 years from the NCEP/NCAR reanalysis data and the WRF outputs.

### 3.3 Discussion

This chapter presents the results from the WRF model and comparisons of each atmospheric forcing field from the NCEP/NCAR reanalysis data and the WRF-derived data.

Among these fields, the precipitation and 2-m relative humidity are the fields that have the least similarity between the two data. No data assimilation is done for these parameters in the NCEP reanalysis, and they should be used with caution (Kalnay et al., 1996). At the same time, humidity and surface precipitation control important processes of surface water exchange between the atmosphere and the ocean. The WRF simulations provide an alternative estimation of these parameters which can be used in the ocean model simulations. Direct comparisons of these simulations with atmosphere data are difficult due to the lack of data. In the Chapter 5, we will compare the surface fluxes computed with these data and their impact on the simulated characteristics of the ocean. In this case, the criterion of the quality of the WRF simulations is based on the analysis of the change of the ocean model simulation.

For surface wind stresses and 10-m wind speed, the WRF patterns and magnitudes are overall close to the corresponding NCEP data. The noticeable differences between the two datasets appear over the coastal areas of Greenland. The WRF-derived wind flow is apparently distorted and the peak magnitudes are strengthened over the coast of Greenland, especially over the east coast. These features arising from the high topography of Greenland (Doyle and Shaprio, 1999) are, however, absent in the NCEP/NCAR data.

Hence, it is believable that the WRF model is able to capture the dominant large-scale characteristics of both atmospheric momentum and heat fields and meanwhile reasonably resolve the effect of the high topography of Greenland as well.

## **Chapter 4: Orographic effects of Greenland on the Atmospheric Flow: Greenland Tip Jets**

This chapter discusses a case study of a forward Greenland tip jet. Observed 10-m wind field from the QuikSCAT daily wind field dataset are used to identify tip jets. The data are compared with the daily NCEP/NCAR and WRF 10-m wind fields. The dynamic features of tip jets are also discussed in detail through the 6-hourly NCEP/NCAR reanalysis data (Kalnay et al., 1996) and the WRF-derived data.

The QuikSCAT near surface wind field, measured by the Quick Scatterometer (QuikSCAT) satellite from 1999 provided by Jet Propulsion Laboratory (JPL), is adjusted to 10-m height, interpolated to  $0.5^{\circ} \times 0.5^{\circ}$  resolution grids, and averaged daily by Centre ERS d'Archivage et de Traitement (CERSAT). Moore and Renfrew (2005) investigated the wintertime climatological features of the QuikSCAT wind and found not only previously identified forward and reverse tip jets, but also barrier winds along the south and north location of the Denmark Strait.

### **4.1 The Forward Greenland Tip Jet: Case study, February 14-15, 2000**

The forward tip jet during the 14th and 15th day of February, 2000 is presented on Figure 4.1. The upper panel shows 10-m wind speeds on February 14, 2000 from the

three datasets—the QuikSCAT observations, the NCEP/NCAR reanalysis, and the WRF-derived data---- and the lower panel on February 15, 2000. On February 14, 2000, strong westerlies up to 30 m/s were observed blowing eastward from Cape Farewell to the Irminger Sea and westerlies exceeding 20 m/s spanned an area of 24° longitudes by 8° latitudes. A strong cyclonic system situated to the north and east of Cape Farewell with a center approximately half way to Iceland. Over the north of the cyclone, strong northeasterlies (about 24-26 m/s) just appeared in the middle of the Denmark Strait. This high wind area was not completely seen near the east coast of Greenland due to missing values in the QuikSCAT wind. These are so-called barrier winds at the Denmark Strait South Location which were identified by Moore and Renfrew (2005). Compared to the observation, the NCEP/NCAR 10-m westerlies on February 14, 2000 were strong at the Cape Farewell (about 22 m/s) and the area of these winds extended eastwards and northwards, and reached 26.71 m/s. This area with wind speed greater than 20 m/s was smaller and about 2/3 of that in the QuikSCAT data. A northeastern-southwestern oriented cyclone was located over the Irminger Sea with its center close to Greenland side. Strong northeasterly flow up to approximate 26 m/s occurred at the northern part of the cyclone and along the east coast of Greenland. The WRF 10-m wind field had more or less the same pattern of the QuikSCAT wind. At the same time, it had finer structure, larger peak winds, and broader range than the NCEP wind. The peak westerly in the WRF wind was about 28 m/s, and the peak northeasterly was 33.92 m/s.

On February 15, 2000, the tip jet was still located between Cape Farewell and Iceland in the QuikSCAT observation, but the peak westerly in the vicinity of Cape Fare slightly decreased to approximate 26 m/s and so did the northeasterly over the middle of

the Denmark Strait. The region with wind speed in excess of 20 m/s entirely moved southeastward. The associated cyclone spread somewhat eastward as well. The NCEP 10-m wind field displayed the decline of the tip jet and the northeast barrier wind and the eastward propagation of the tip jet and the cyclone. The NCEP tip jet and cyclone declined more rapidly and moved faster than the QuikSCAT. The NCEP peak westerly decreased to 22.30 m/s and the barrier wind to less than 20 m/s. The center of the NCEP cyclone moved to the south of Iceland. By contrast, the WRF wind on this day was more close to the observation. The peak westerly decreased to 25.87 m/s and the northeast barrier wind to less than 26 m/s. The whole system propagated a little bit eastward and the center of the cyclone still located between Cape Farewell and Iceland exactly as the QuikSCAT wind did.

The tip jet observed during February 14-15, 2000 was related to a cyclonic system. This result agrees with previous studies (e.g. Pickart et al., 2003). The comparisons between the observations and the model datasets shows that the WRF 10-m wind was closer to the QuikSCAT daily wind field than the NCEP wind and more realistic than the NCEP wind, not only in the detail structure and the peak magnitudes, but in its propagation and evolution as well.

The processes of the formation, development, and decay of the synoptic systems related to the Greenland tip jet during February 14-15, 2000 are then discussed. The atmospheric parameters on February 13, 2000 (at 00:00 and 12:00) defined the meteorological environment which was prior to the formation of the tip jet. February 14, 2000 (at 00:00 and 12:00) represented the moment of the formation and development of the tip jet and February 15, 2000 (at 18:00) showed the moment of the decay of the tip jet.

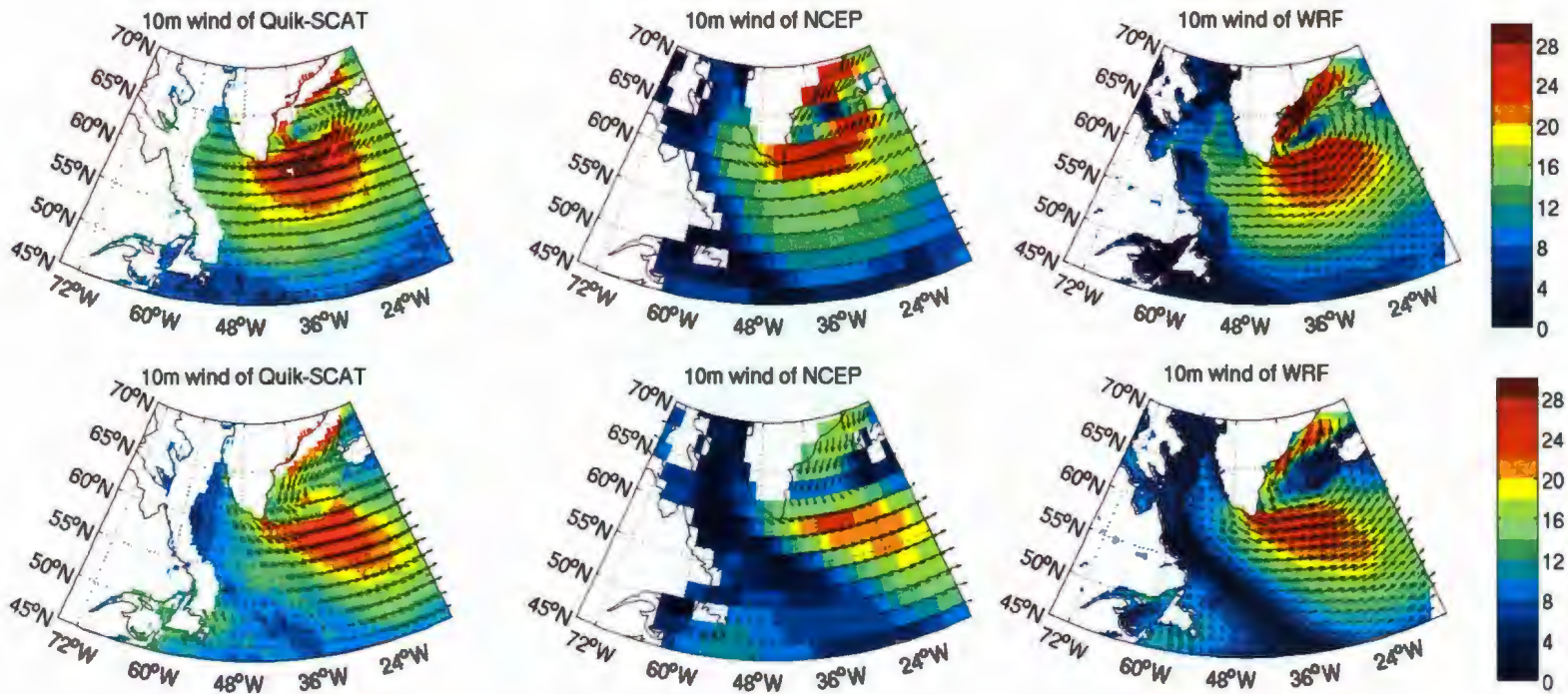


Figure 4.1 A forward Greenland tip jet during February 14-15, 2000

(The upper panel is on February 14 and the lower panel is on February 15; the left panel is 10-m wind speed (m/s) from the QuikSCAT satellite observation, the middle panel from the NCEP/NCAP reanalysis data, and the right panel from the WRF model results.)

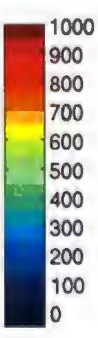
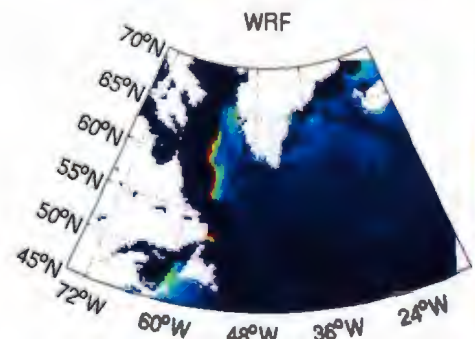
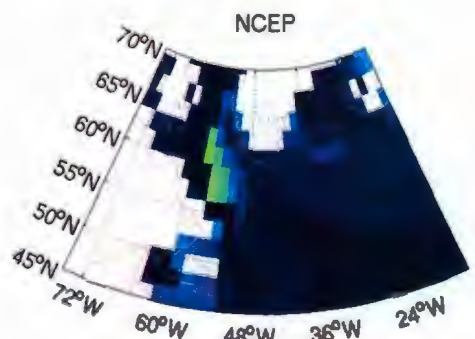
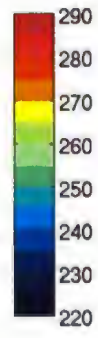
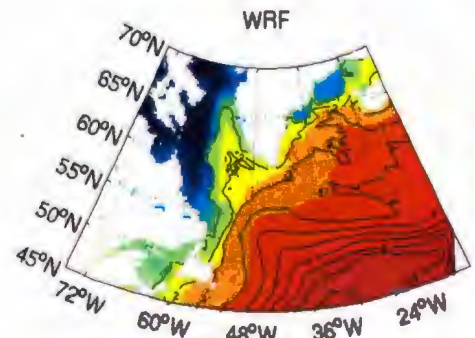
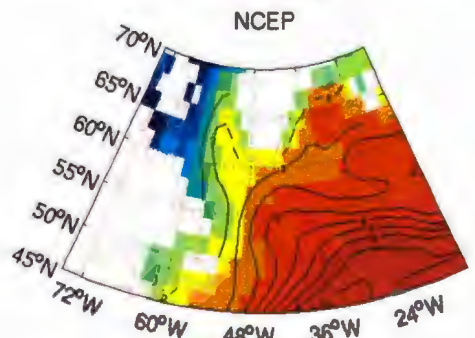
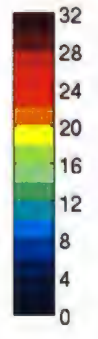
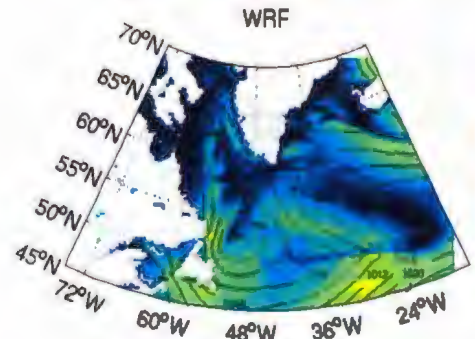
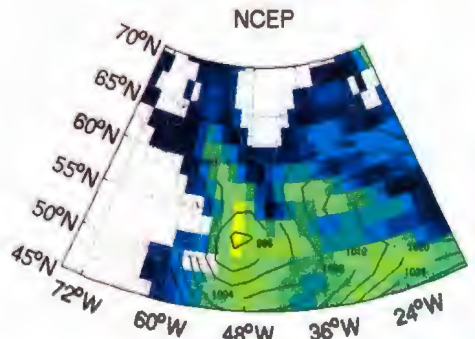
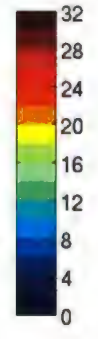
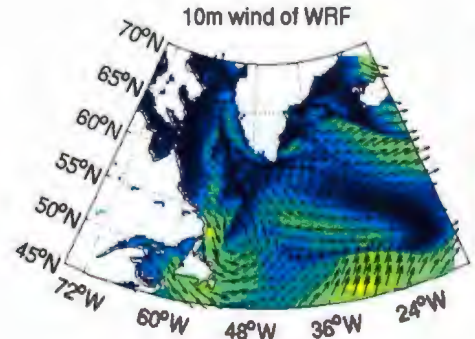
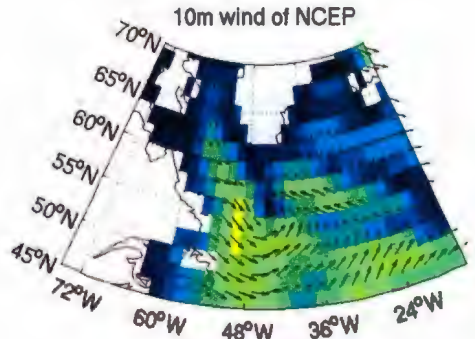
The sea level pressure, 2-m air temperature and specific humidity, and surface sensible and latent heat fluxes are diagnosed at these time periods. Those variables discussed here indicate in the large-scale circulation environment and the interaction between the atmosphere and the ocean as simulated by the NCEP/NCAR reanalysis and the WRF model.

Figure 4.2 – 4.6 shows the 10-m wind vector and speed (the first row), sea-level pressure (the second row), 2-m air temperature and specific humidity (the third row), surface sensible heat flux (the fourth row) and surface latent heat flux (the fifth row) at each moment respectively. The left panel is from the NCEP/NCAR reanalysis (Kalnay et al., 1996) and the right panel from the WRF-derived data.

At the very beginning of February 13, 2000 (Figure 4.2), i.e. 24 hours before the tip jet formed, a low pressure system emerged over the Labrador Sea northeast of Newfoundland. Combined the wind field with air temperature and specific humidity, a cold front appeared over the east of the low center, approximately along 48°W in the NCEP data and 48.5°- 49°W in the WRF data. There was a warm and moist air mass ahead (east) of this cold front and cold and dry air mass behind (west). This kind of pattern is related to genesis and deepening of the low. At this time, the low pressure in the WRF data (988 hPa at its center) was stronger than the NCEP data (992 hPa at its center) and the wind in the vicinity of the low pressure was very weak in the WRF. Surface sensible and latent heat fluxes were very small over the subpolar North Atlantic. High sensible heat fluxes occurred in the middle of Labrador Sea, mostly in the WRF data. This results from the horizontal contrast of the atmospheric and surface characteristics. The atmospheric flow over the sea ice and land snow was colder and drier than it is over the

ocean. When it reaches the ice-free ocean surface, the contrast of the temperature across the ocean surface was strong and fluxes were intensified. In WRF simulation, the air warmed quickly as propagated over the ice-free ocean. In this way, the sensible heat formed a strong pattern just near the ice edge (see the coverage of sea ice on Figure 4.7). The WRF data with fine resolution more realistically presented the sea ice coverage and thus spatial patterns of the surface sensible heat fluxes. The corresponding distribution of the surface sensible heat fluxes was smooth and much weaker in the NCEP/NCAR data (Kalnay et al., 1996).

At 12:00 of February 13, 2000 (Figure 4.3), i.e. 12 hours before the tip jet formed, the cold air mass behind the cold front and the warm air mass ahead of the cold front moved eastward. The low pressure propagated northeastward, its center reached over the south of Cape Farewell, and it was additionally strengthened (the center value: 976 hPa in the NCEP and 972 hPa in the WRF). The peak wind speed associated with this cyclone enhanced to approximately 26 m/s and appeared over the southwestern part of the cyclone where the greatest pressure gradient occurred. The surface sensible heat flux at this time increased along the interfaces between the ocean and sea ice (over the middle Labrador Sea and east coast of Greenland) resulting from the stronger wind across the sea-ice edge. This intensification of the surface sensible heat flux was pretty strong in the WRF data, but largely underestimated in the NCEP data, even though the wind speed along the sea-ice edge increased in both the datasets. The surface latent heat flux related to wind speed intensified as well over the peak wind area. The amplitude of the surface heat flux was larger in the WRF than in the NCEP.



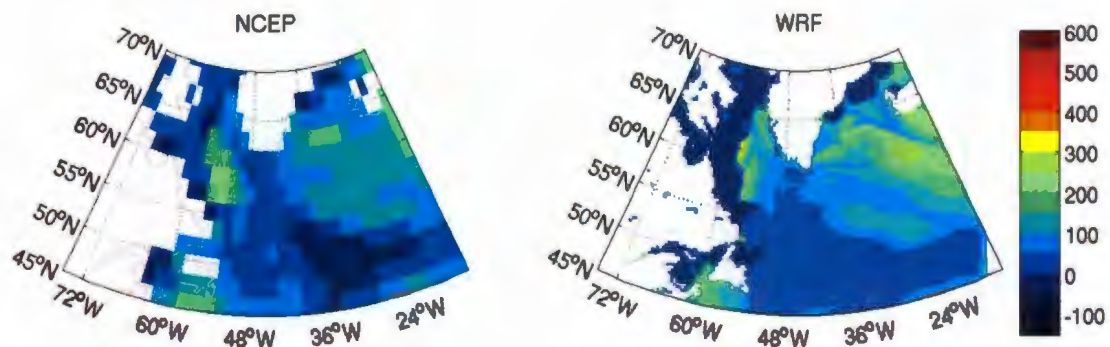
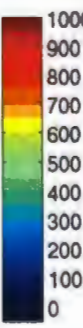
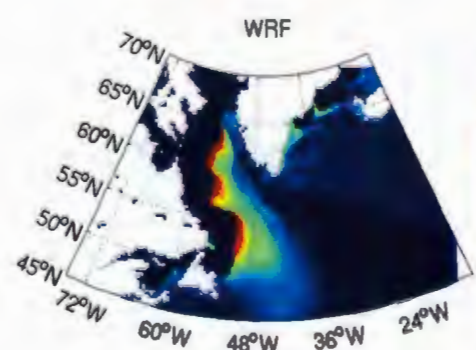
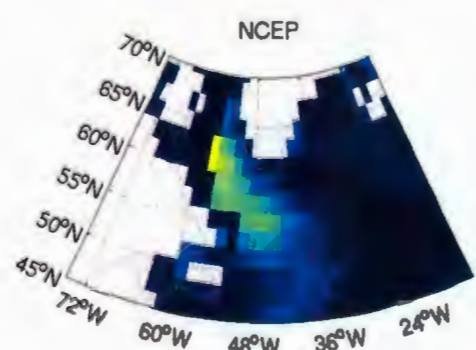
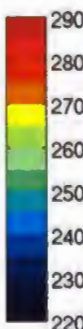
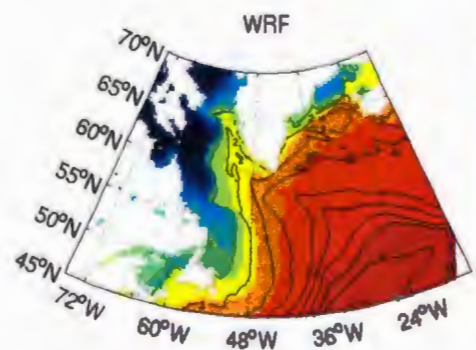
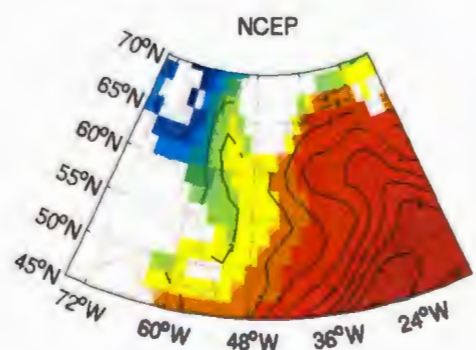
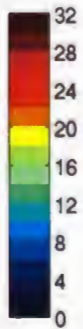
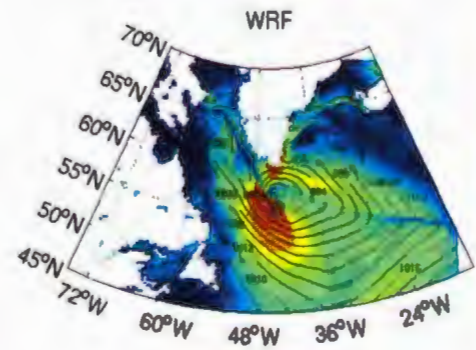
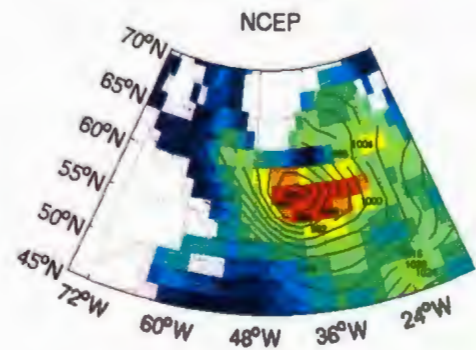
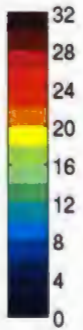
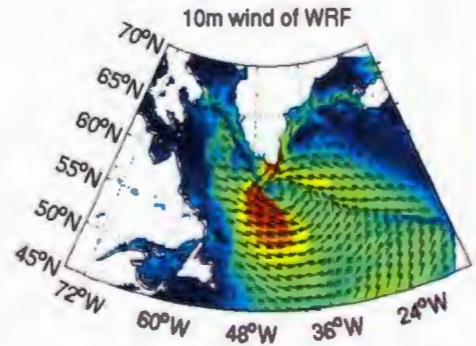
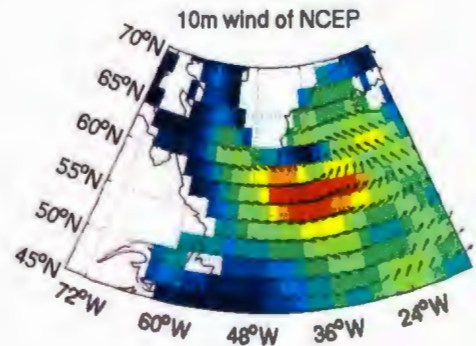


Figure 4.2 Meteorological features at 00:00 February 13, 2000.

(The left panel is the field from the 6-hourly NCEP/NCAR reanalysis data and the right panel from the WRF-derived data. The first row is 10-m wind (vector) and wind speed (m/s, color), the second row 10-m wind speed (m/s, color), and sea-level pressure (hPa, contours), the third row 2-m temperature ( $^{\circ}\text{K}$ , color) and 2-m specific humidity (g/Kg, contours), the fourth row surface sensible heat flux ( $\text{W}/\text{m}^2$ ), and the fifth row surface latent heat flux ( $\text{W}/\text{m}^2$ .)



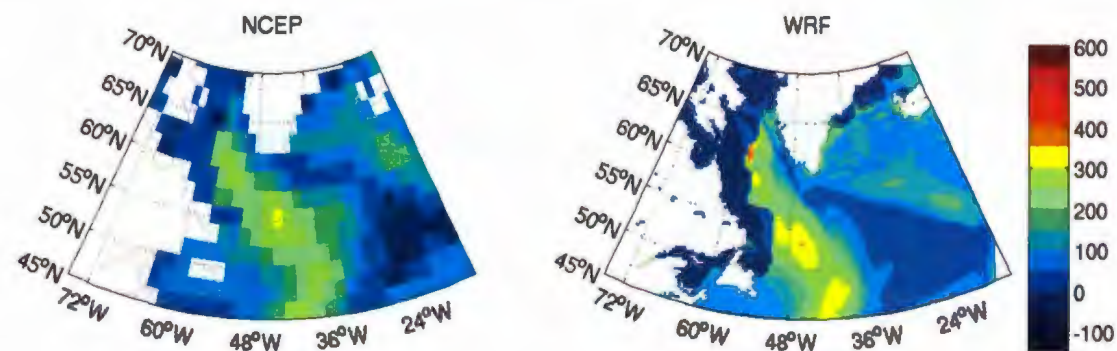
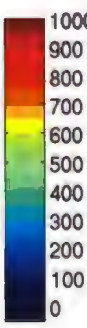
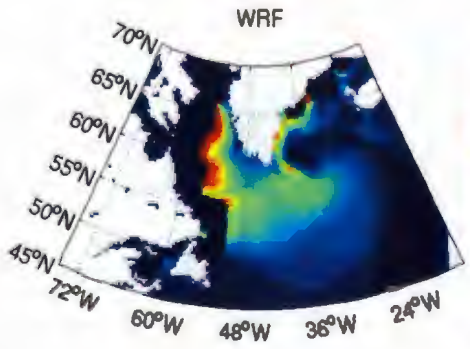
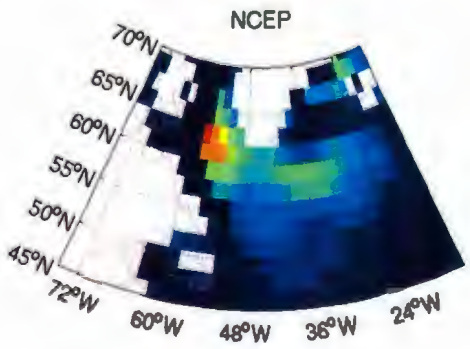
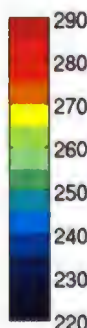
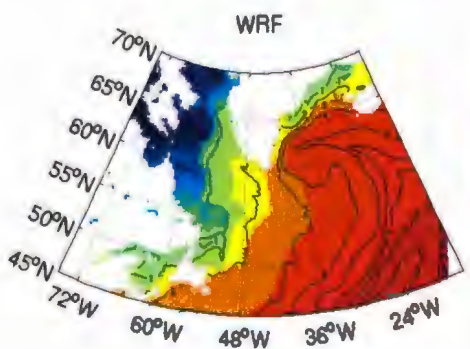
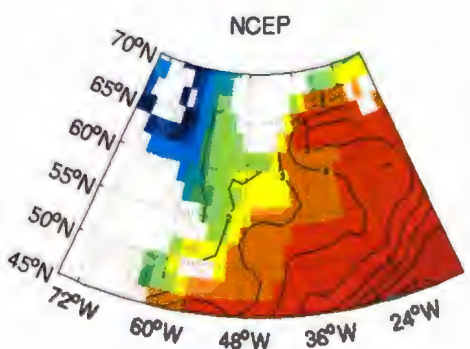
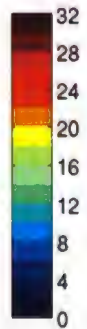
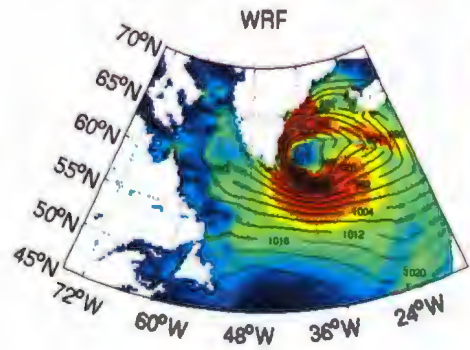
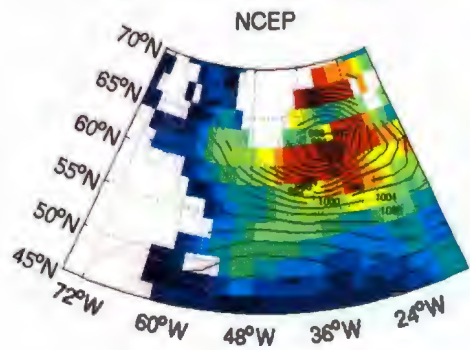
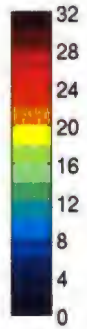
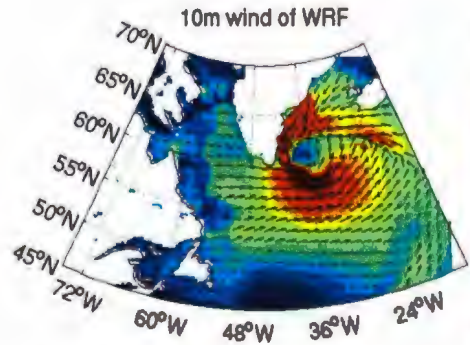
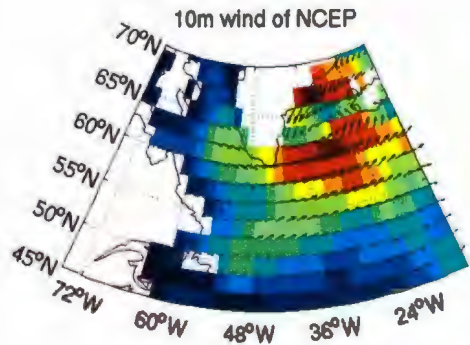


Figure 4.3 Same as Figure 4.2, but at 12:00 February 13, 2000.

12 hours after 12:00 February 13, 2000 (Figure 4.4) is the time of the formation of the tip jet. The two types of the air mass as well as the cold front continued moving eastward. The tip jet-generating low pressure spread northeastward with its center situated northeast of Cape Fare in the NCEP and east of Cape Fare in the WRF. The pressure at the center was 964 hPa in the NCEP and 960 hPa in the WRF, respectively. The warm air mass invaded the low center. The peak wind of the tip jet appeared over the southwest and south of its parent low pressure and reached 30.12 m/s in the NCEP and 35.56 m/s in the WRF. The high winds occurred over the northwest of the low pressure. The wind speed and surface sensible heat flux over the edge of sea ice increased. The surface sensible heat flux had values up to about  $700\text{W/m}^2$  in the WRF over the peak wind area of the tip jet, i.e. the southeast of Cape Fare, but the corresponding value was pretty much smaller in the NCEP. The surface latent heat flux enhanced to  $450\text{W/m}^2$  over the peak wind area in both the datasets.



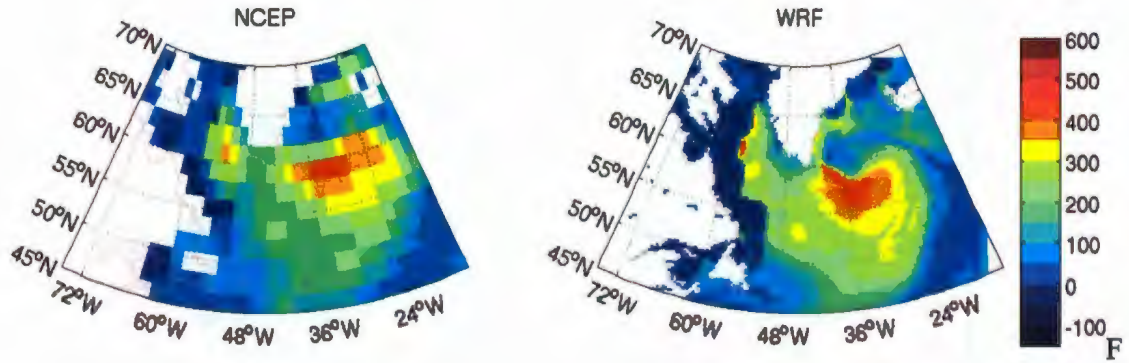
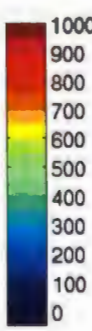
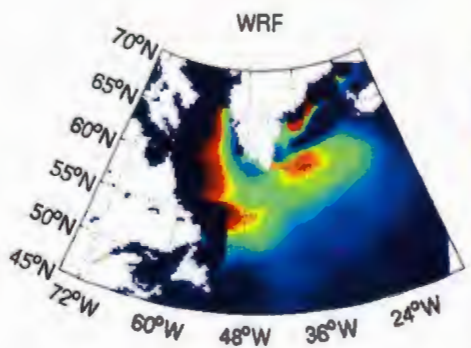
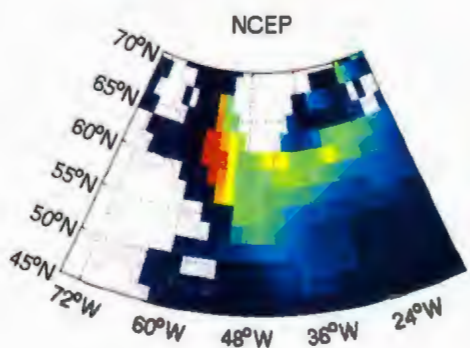
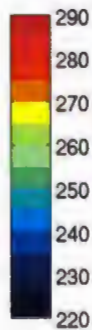
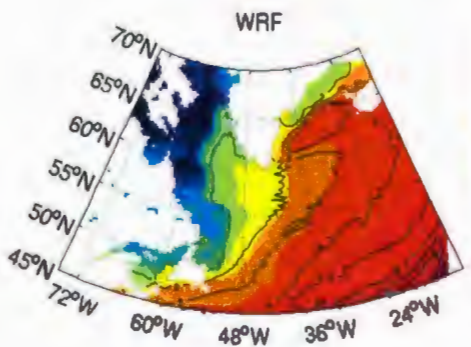
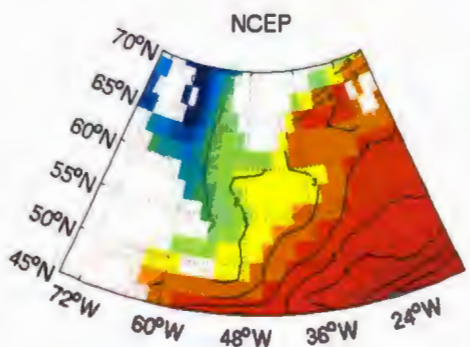
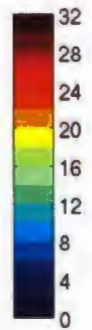
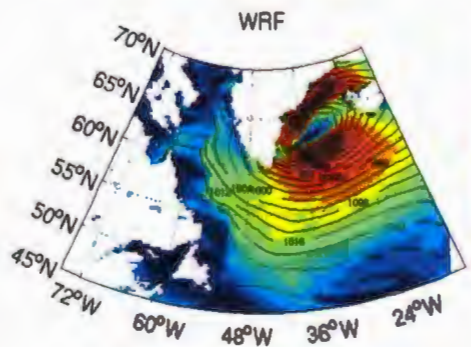
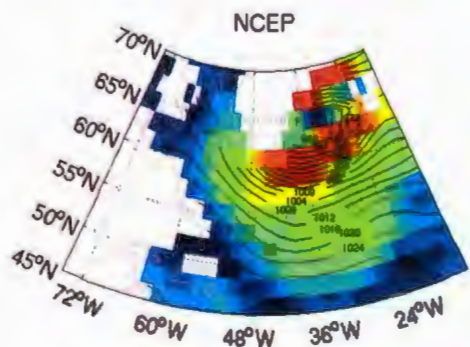
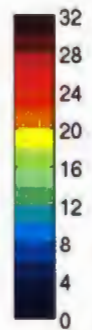
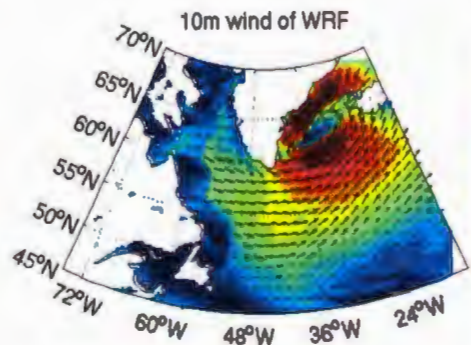
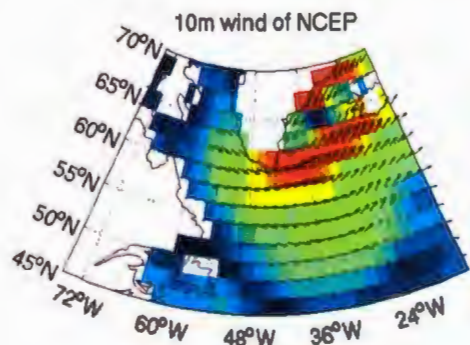


Figure 4.4 Same as Figure 4.2, but at 00:00 February 14, 2000.

The tip jet achieved its strongest phase at 12:00 February 15, 2000 (Figure 4.5). At this moment, the tip jet-generating low pressure reached its minimum. The center had the pressures of 960 hPa in the NCEP and 952 hPa in the WRF and moved to the location between Cape Farewell and Iceland. The peak wind of the tip jet over the southeast of the cyclone was 28.85 m/s in the NCEP and over 32 m/s in the WRF. The peak wind of the barrier wind over the Denmark Strait South location was about 36 m/s. The warm air mass over the center of the cyclone became slightly colder and drier. This indicated that the cold front and the tip jet-generating cyclone started to weaken after this moment. The surface sensible heat flux increased to its maximum 650 W/m<sup>2</sup> in the NCEP and 800 W/m<sup>2</sup> in the WRF over the peak wind area of the tip jet. It also increased over the sea-ice edge in the WRF data. The surface latent heat flux reached the strongest value of 550 W/m<sup>2</sup> in the NCEP and 600 W/m<sup>2</sup> in the WRF over the peak wind area of the tip jet.



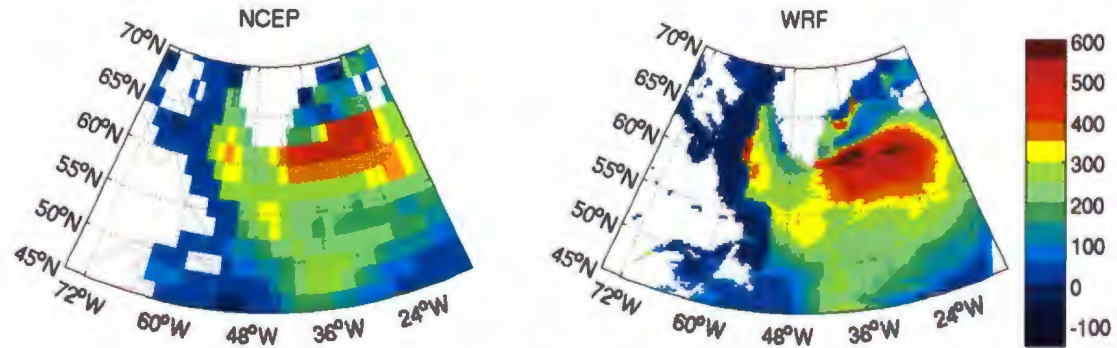
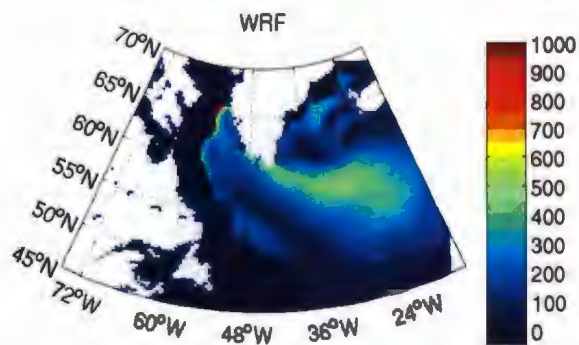
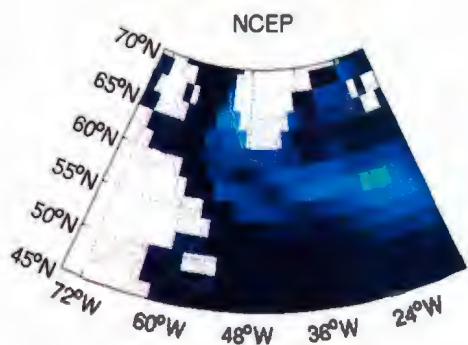
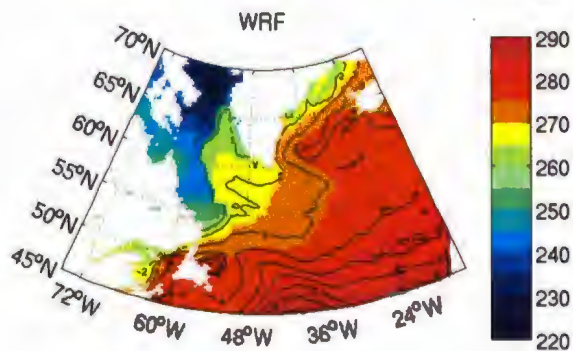
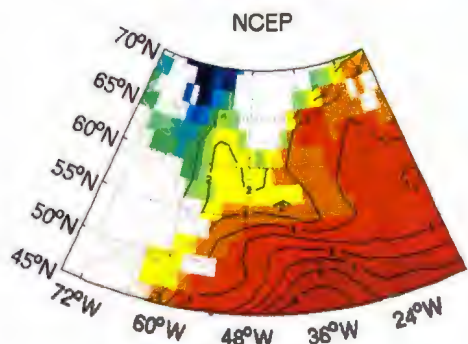
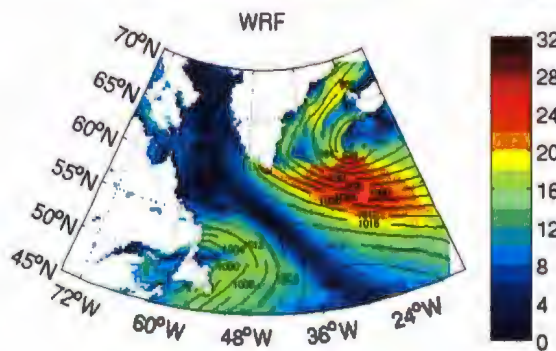
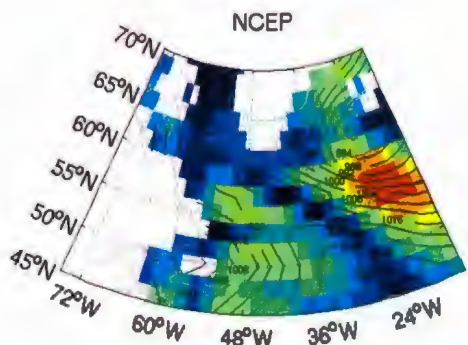
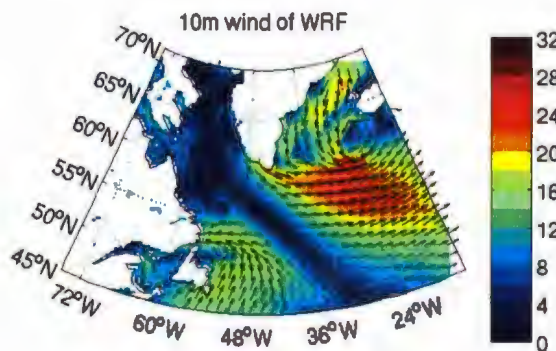
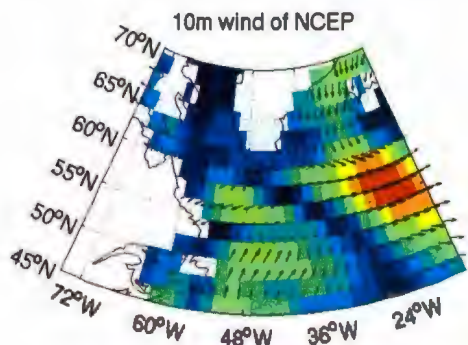


Figure 4.5 Same as Figure 4.2, but at 12:00 February 14, 2000.

After reaching the strongest phase, the tip jet started to weaken. At 18:00 February 15, 2000 (Figure 4.6), the warm air mass near the center of the cyclone became colder and drier, and resulted in the frontolysis of the cold front. Hence, the tip jet-generating low pressure, despite stay about two days over the Irminger Sea, started to weaken after 12:00 February 14, 2000. The pressure of its center increased to 980 hPa in the NCEP and 976 hPa in the WRF. The peak wind speed of the tip jet over the south of the cyclone decreased to approximate 26 m/s in the NCEP and 28 m/s in the WRF and the barrier wind over the northwest of the cyclone disappeared in the NCEP and decreased to less than 20 m/s in the WRF. The eastward displacement of the low was related to a decline of the surface sensible and latent heat fluxes. The surface sensible heat flux associated with the tip jet decreased to less than  $450 \text{ W/m}^2$ , and the latent heat flux to  $500 \text{ W/m}^2$ . On the plot of the surface sensible heat flux, the high value area over the interfaces between the ocean and seaice severely decreased arising from the decline of the wind over there.



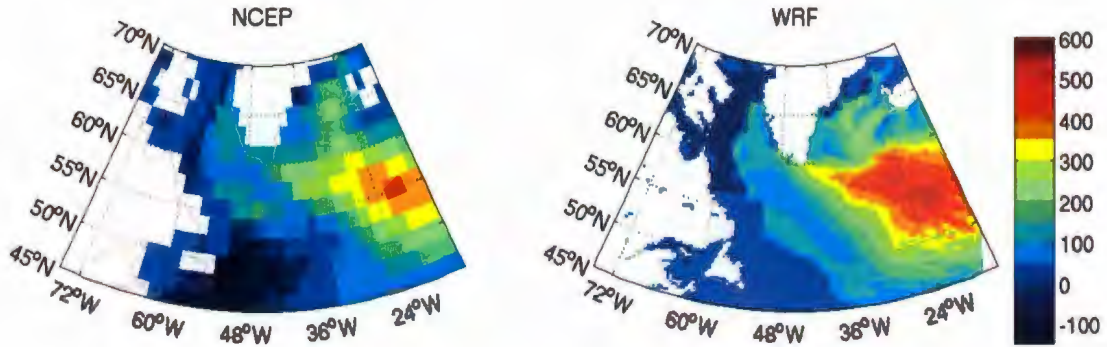


Figure 4.6 Same as Figure 4.2, but at 18:00 February 15, 2000.

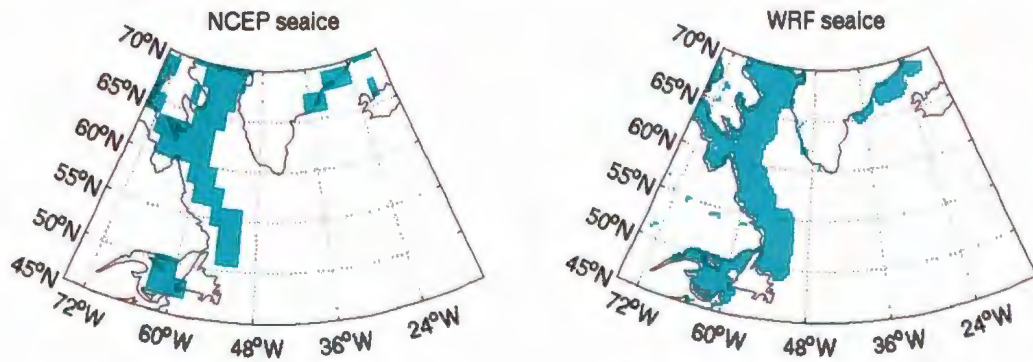


Figure 4.7 Sea ice coverage in February, 2000

(The left is from the NCEP/NCAR reanalysis data (Kalnay et al., 1996) and the right from the WRF-derived data.)

## 4.2 Discussion

The evolution of the forward tip jet in the analysis above was dominated by the tip jet-generating cyclone which followed the cold front ahead. The cyclonic system came

from the Labrador Sea northeast of Newfoundland, then rapidly progressed northeastward to the Irminger Sea, stayed over the Irminger Sea for two days, and finally moved eastward. When approaching to Greenland from the southwest, the cyclone deepened. While moving eastward out of the Irminger Sea, the cyclone filled. These evolution processes of the tip jet-generating cyclone were a typical demonstration of the mean behaviour of these kind cyclones (Vage et al., 2009). They also indicated that the high topography of Greenland combined with the synoptic-scale cyclonic system was the major mechanism of the formation of Greenland tip jets (Vage et al., 2009).

Compared to the behaviour of the NCEP data, the WRF data had a number of advantages due to the finer resolution. First of all, all the features in the WRF had more detailed structures. The peak wind speed and the high wind range in the WRF were much closer to the QuikSCAT observations. The cyclone associated with the tip jet was deeper in the WRF than in the NCEP. The match of the wind field and the sea-level pressure was more physical and realistic in the WRF data. The surface sensible and latent heat fluxes over the tip jet area were larger in the WRF data. Since the sea ice coverage was finely resolved, the represent of the surface sensible heat flux was more realistic along the sea-ice edge in the WRF data.

## **Chapter 5: Modeling Interannual Variability in the Subpolar North Atlantic Ocean**

The Subpolar North Atlantic (Figure 5.1) is an essential region for the global climate. The general cyclonic circulation, weak stratification, and strong oceanic winter heat loss create conditions in the Labrador Sea for open-ocean deep convection and formation of the Labrador Sea Water (LSW) (Marshall and Schott, 1999). Together with the Greenland-Scotland Overflow water which originates from mid-depths in the Nordic Seas, the LSW contributes to the North Atlantic Deep Water (NADW), which acts as the lower limb of the global Meridional Overturning Circulation (MOC) and has an important impact on the climate of the Earth.

Hydrographic observations have revealed that recently the Subpolar North Atlantic experienced significant changes on the interannual to interdecadal time scales, especially in the Labrador Sea (Dickson et al., 2002; Häkkinen and Rhines, 2004; Yashayaev, 2007; Lohmann et al., 2009). In particular, the Labrador Sea was extremely warm and salty between the mid-1960s and early 1970s, fresh and cold between the late 1980s and mid-1990s, and becoming warm and salty again between the late 1990s and early 2000s (Yashayaev, 2007). Satellite altimeter data suggested a considerable weakening of the subpolar gyre from the early 1990s to early 2000s (Häkkinen and Rhines, 2004).

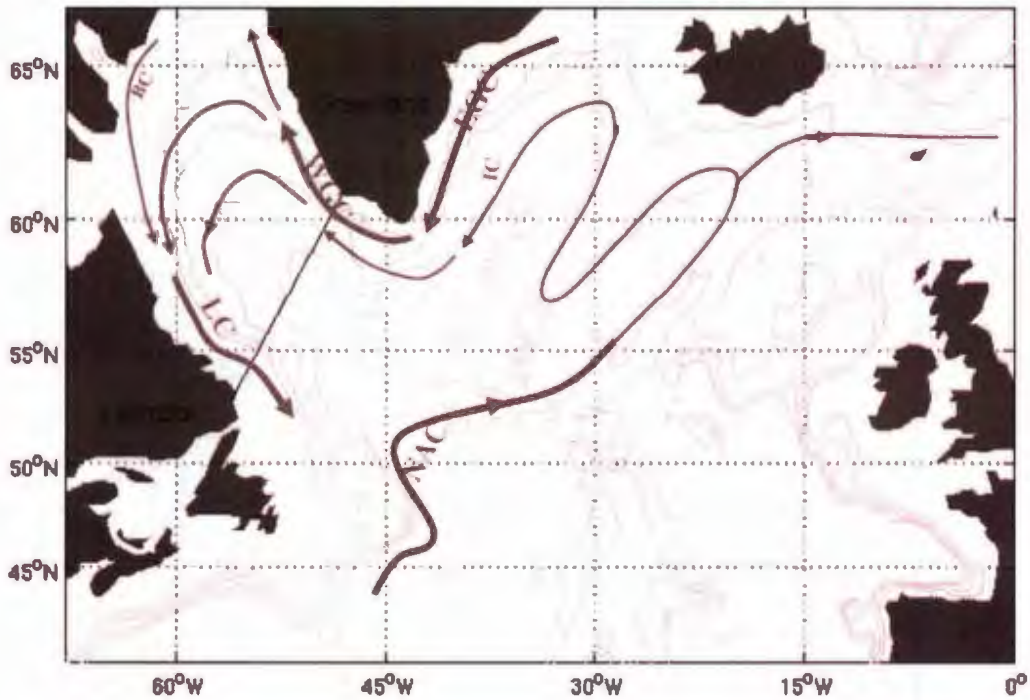


Figure 5.1 Map of the sub-polar North Atlantic.

(The isobaths are 700, 2000, 3000, 3500, 6000 m (light contours). Also marked are the locations of the WOCE AR7W hydrographic section (black line between Hamilton Bank, Labrador and Cape Desolation on the West Coast of Greenland). Arrows depict schematically the surface (or near surface) current system (NAC: North Atlantic Current; EGC: East Greenland Current; WGC: West Greenland Current; LC: Labrador Current; IC: Irminger Current; BC: Baffin Island Current).

This chapter presents the results from a model simulation of interannual variability of the Labrador Sea, forced with the WRF model-derived data over the subpolar North Atlantic (the Exp\_SPWRF simulation). The results are compared with the model simulation forced with NCEP/NCAR reanalysis data (the Exp\_SPNCEP simulation).

## 5.1 Simulations of Interannual Variability of North Atlantic

### Subpolar Gyre

In this section, the simulations of interannual variability of the Subpolar North Atlantic from the Exp\_SPWRF experiment are validated against the hydrographic observations. The vertical sections of simulated potential temperature and salinity along the WOCE AR7W section averaged in May and June of 1993 and 2005 are shown on Figure 5.2 and 5.3, respectively.

In 1993, the Exp\_SPWRF potential temperature (Figure 5.2b) is approximate 2.8 °C at the most part of depths above 2400 m and salinity (Figure 5.2d) less than 34.86 at depths above 1500 m. Compared to the observation (Yashayaev, 2007), the model potential temperature in the Exp\_SPWRF experiment has a warm bias of 0.1 °C at the from 1000-2000m depth and the salinity has a bias of about 0.02 at depths shallower than 1500 m and 0.03 at the depth of 1500-2000 m.

In 2005, the potential temperature and salinity are overall larger than those in 1993 over the upper layer. In the observation (Yashayaev, 2007), potential temperature along the AR7W section is about 3.4 °C and salinity is 34.85-34.86 at depths from 500 m to 1000 m. A surface cooling and freshening occurs over the depth shallower than 500 m. In the Exp\_SPWRF results, potential temperature (Figure 5.3c) is between 3.4-3.5°C in the depth range between 500 m and 1000 m; salinity (Figure 5.3d) is about 34.85 between 500 m and 750m and 34.86-34.88 between 750 m and 1000 m. Hence, the Exp\_SPWRF simulation has a warm bias less than 0.1 °C in the depth range between 500 m and 1000 m

and a salty bias less than 0.02 in the depth range between 750 m and 100m. The surface freshening on the Labrador side in the Exp\_SPWRF simulation (Figure 5.3d), but shifts eastward to the middle of the Labrador Sea (Figure 5.3c).

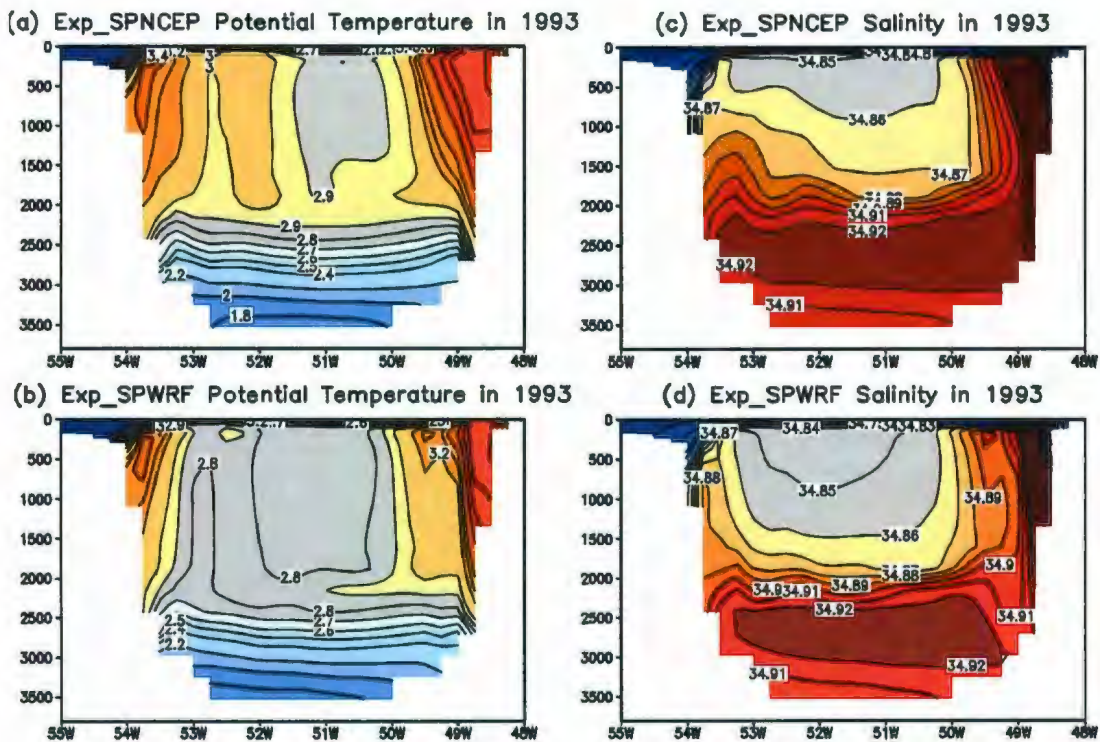


Figure 5.2 Potential temperature ( $^{\circ}\text{C}$ , left panel) and salinity (psu, right panel) averaged in May and June of 1993 along the AR7W section from the results of the Exp\_SPNCEP (upper panel) and Exp\_SPWRF (lower panel) experiments (Table 2.3), respectively.

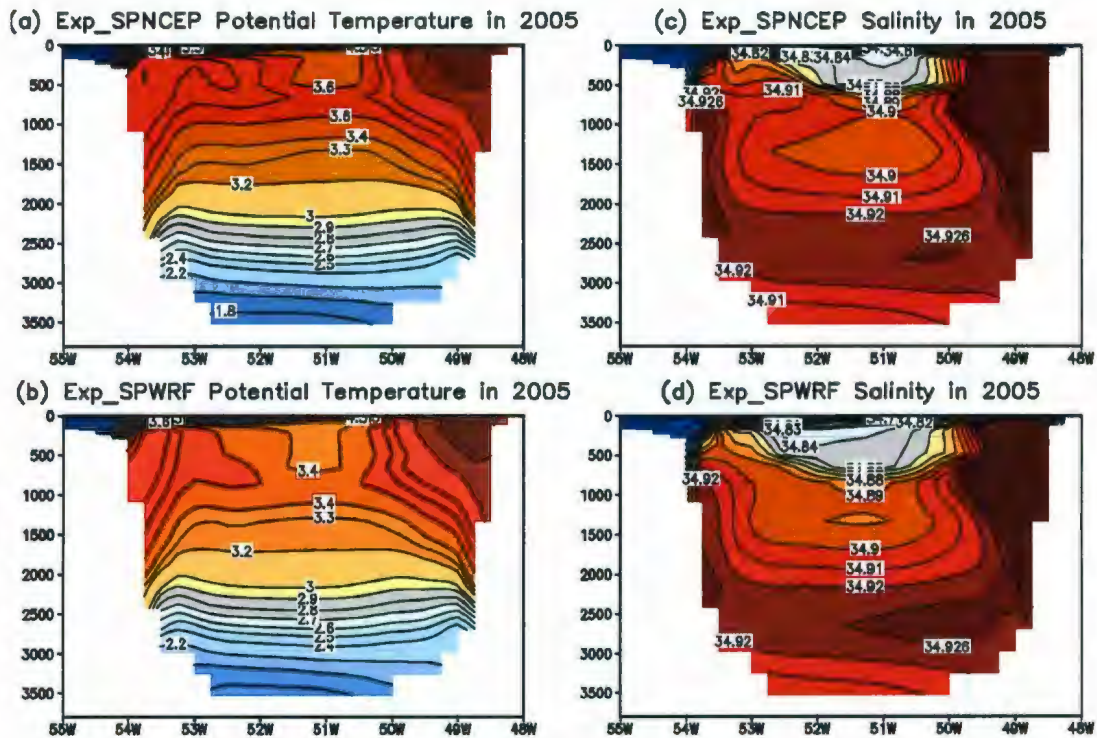


Figure 5.3 Same as the Figure 5.2, but in 2005.

Mixed layer depth at the end of March in 1993 and 2005 are shown on Figure 5.4. At the end of March, 1993, mixed layer depth from the WRF-forced simulation (i.e. Figure 5.4 (b)) in the central Labrador Sea exceeds 1800 m with a maximum 2600 m at (60°N, 54°W). This extremely deep mixed layer depth in the central Labrador Sea, as well as the results of the vertical section along the AR7W section (Figure 5.2 and 5.3, lower panel), shows that the deep convection in 1993 extends down to depths close to the observation (Yashayaev, 2007). The mixed layer depth in the central Irminger Sea is as deep as and 1800 m.

In the Exp\_SPWRF simulation, the mixed layer in the Labrador Sea at the end of March, 2005 (Figure 5.4e) is much shallower than that in 1993. Mixed layer depth had a

maximum depth about 1000 m in the central Labrador Sea (58°N, 54°W), which agrees with the observation.

From the different features of potential temperature, salinity and mixed layer depth in the Labrador Sea in 1993 and 2005, there exists the inter-annual variability of these quantities. The potential temperature and salinity from 1980 to 2005 over the central Labrador Sea are shown on Figure 5.5. Potential temperature and salinity from the Exp\_SPWRF simulation (Figure 5.5b, d) show strong interannual variabilities in the upper layer above 2300 m from 1980 to 2005. Sea water in the upper layer (above 2300 m) has large temperature (3.2-3.6 °C) and salinity (> 34.87) during 1980-1982 and 1997-2005 and lower temperature (2.7-3 °C) and salinity (< 34.86) during 1983-1984 and 1989-1994. Compared with the observation in the upper layer from 1987 to 2006 (Yashayaev, 2007), potential temperature is as low as 2.7-2.9 °C and salinity was 34.83-34.84 during 1989-1997; potential temperature is between 3.1 °C and 3.6 °C and salinity was in the range of 34.84 to 34.88 during 2003-2006. During the deep convection event in the Labrador Sea in 1993-1994, the Exp\_SPWRF simulation shows a bias of 0.2 °C in temperature and 0.03 in salinity. In the deep layer below 3000 m, the observation (Yashayaev, 2007) shows a freshening trend from the 1990s. This trend, however, is not presented in our Exp\_SPWRF simulation. The observational studies show that this trend was caused by change of the properties of the overflow through the Denmark Strait. These changes are underestimated in the dataset used to define the open boundary conditions in this study. Hence, the freshening effect is missed in the present simulation.

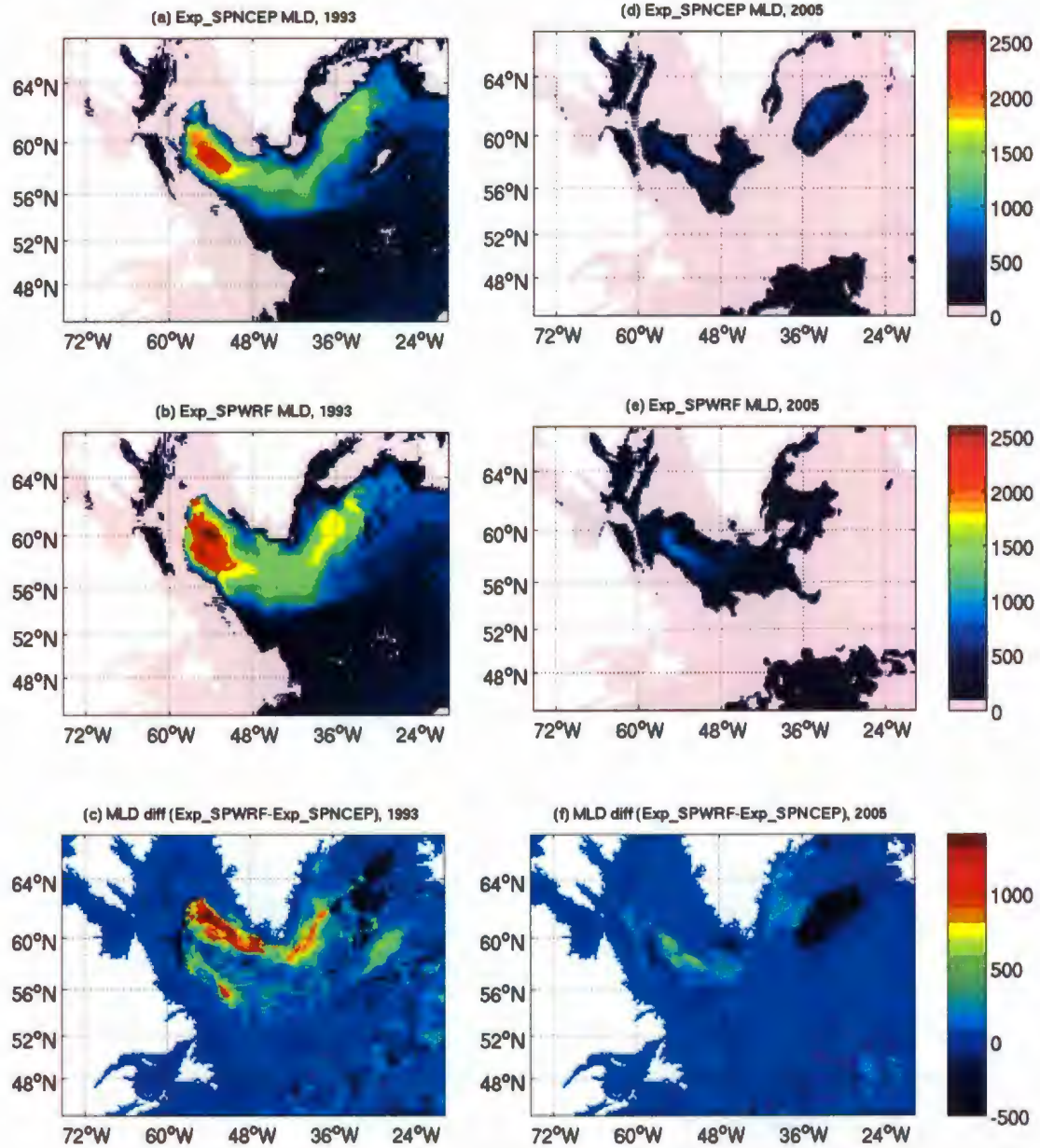


Figure 5.4 Mixed layer depth (m) at the end of March in 1993 (left panel) and 2005 (right panel).

(The upper panel is from the Exp\_SPNCEP simulation, the middle panel from the Exp\_SPWRF simulation, and the lower panel is the difference between the Exp\_SPWRF and Exp\_SPNCEP simulations.)

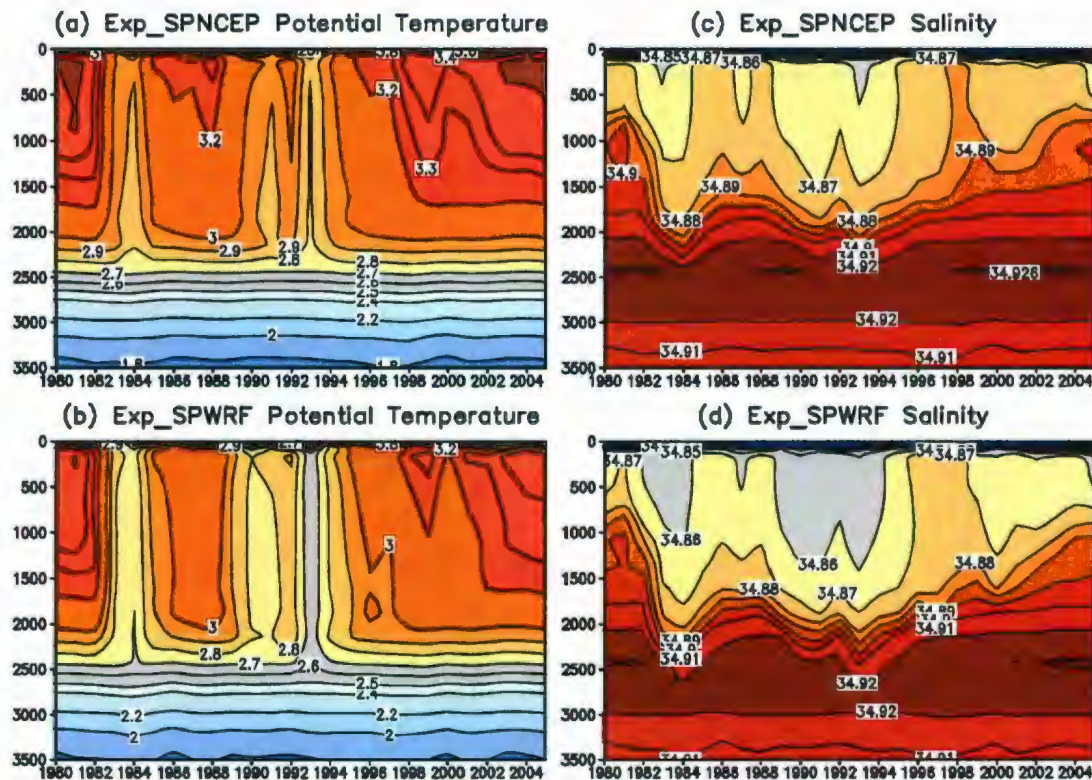


Figure 5.5 Potential temperature ( $^{\circ}\text{C}$ , left panel) and salinity (psu, right panel) averaged in May and June of each year during 1980-2005 over the central Labrador Sea from the results of the Exp\_SPNCEP (upper panel) and the Exp\_SPWRF (lower panel) experiments (Table 2.3), respectively.

The strength of the subpolar gyre in the North Atlantic Ocean can be represented by barotropic stream function. Barotropic stream function (BSF) represents the vertically integrated volume transports over the entire water column. Figure 5.6 shows the area mean BSF from 1980 to 2005 of the Exp\_SPNCEP (blue solid curves) and Exp\_SPWRF (red dashed curves) simulations and the first principle components of the observed

surface geostrophic velocity of Häkkinen et al. (2008) (black solid thick lines) and Häkkinen and Rhines (2004) (black dashed thick lines) from 1992 to 2005. Since the y-axis is reversed, the peaks in Figure 5.6 are minimum BSF, maximum transports and strongest subpolar gyre.

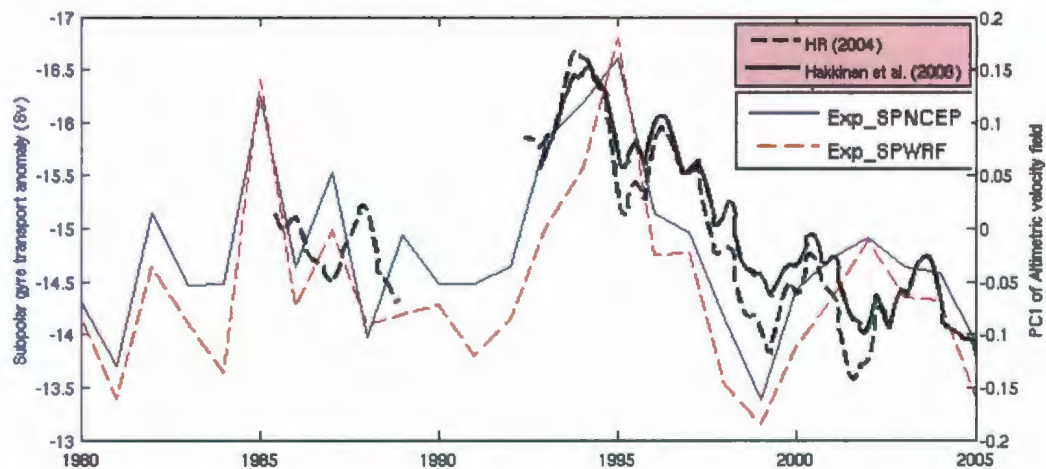


Figure 5.6 Yearly barotropic stream function (BSF, Sv) from averaged over the ocean area in (46.05°N – 65.70°N, 72.75°W – 22.25°W).

The blue, solid curves indicates the BSF from the Exp\_SPNCEP and the red, dashed curves from the Exp\_SPWRF simulation. The black solid and dashed thick lines indicate the first principal components of the observed sea level anomalies in Häkkinen et al. (2008) and Häkkinen and Rhines (2004), respectively.

The strength of the subpolar gyre in the Exp\_SPWRF simulation (red dashed curves) exhibits an interannual variability during the 26 years of the simulations. The red dashed curves detects a increasing trend of the subpolar gyre from the late 1980s to the mid-

1990s and a decline trend from the mid-1990s to 2005. This decline trend is consistent with the both observations which displays a weakening trend of the subpolar gyre from 1994 to 2005.

## **5.2 Impacts of High-Resolution Atmospheric Forcing on Subpolar North Atlantic Simulations**

In this section, the simulation of the subpolar North Atlantic Ocean in the ocean simulation forced with the WRF-derived data (i.e. Exp\_SPWRF) is compared with the results from the ocean simulation forced with the NCEP/NCAR reanalysis (i.e. Exp\_SPNCEP). In particular, we study the impact of the resolution of the atmospheric forcing on the subpolar North Atlantic simulation.

The upper panel on Figure 5.2 shows the vertical section of ocean potential temperature and salinity in the Exp\_SPNCEP experiment averaged in May and June along the AR7W section in 1993. In the upper layer (above 2400 m), the potential temperature in the Exp\_SPNCEP experiment is between 2.9° and 3°C, which is overall larger than the Exp\_SPWRF potential temperature by about 0.1 °C. The Exp\_SPNCEP salinity is 0.01 larger than the Exp\_SPWRF salinity. Hence, the warm and salty bias in the Exp\_SPNCEP simulation is higher than the Exp\_SPWRF one. Similar are the bias characteristics in 2005 (Figure 5.3). In 2005, the upper layer (above 1000 m) potential temperature in the Exp\_SPNCEP simulation (Figure 5.3a) is warmer (0.2 °C) than that in the Exp\_SPWRF one and the salinity (Figure 5.3c) was 0.01 saltier. The mixed layer depth in the Labrador

Sea and the Irminger Sea at the end of March, 1993 from the Exp\_SPNCEP simulation (Figure 5.4a) was shallower than that from the Exp\_SPWRF simulation (Figure 5.4c). In 2005, it is similar. The Exp\_SPNCEP mixed layer depth (Figure 5.4d) is much shallower in the central Labrador Sea than the Exp\_SPWRF one which is the same as the observation.

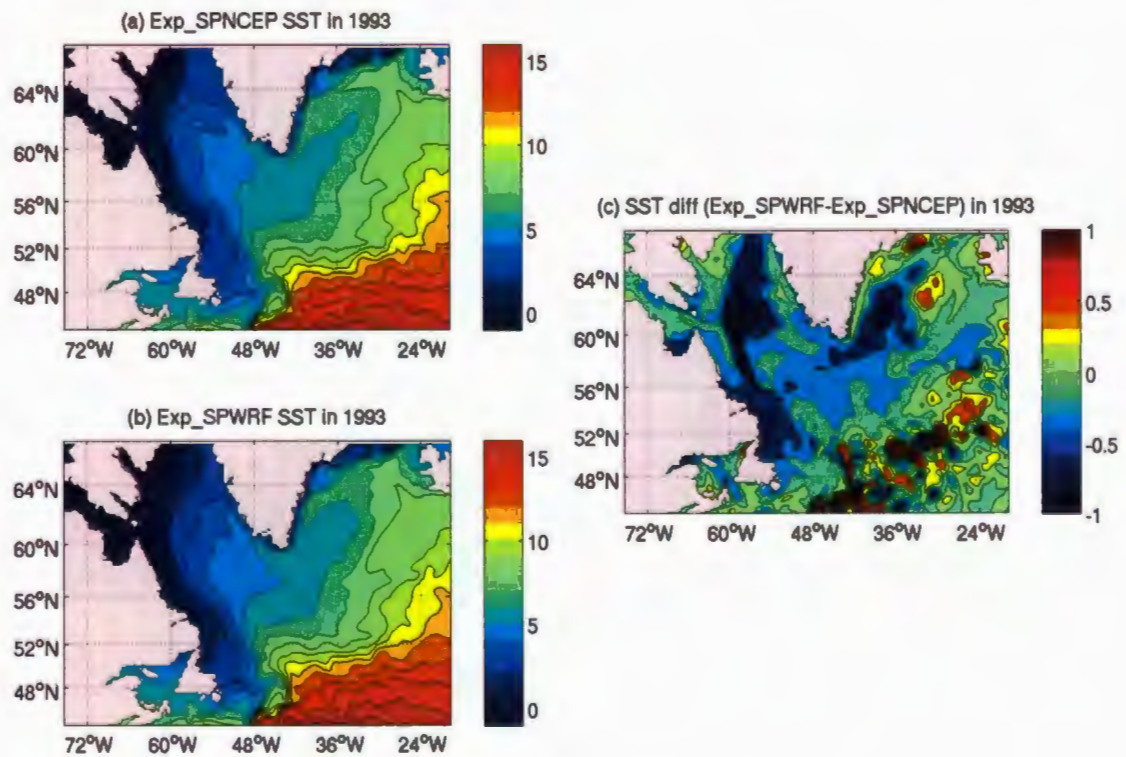


Figure 5.7 Sea surface temperature (SST, °C).

((a) is from the Exp\_SPNCEP simulation, (b) from the Exp\_SPWRF simulation, and (c) is the difference between the two simulations (Exp\_SPWRF-Exp\_SPNCEP)).

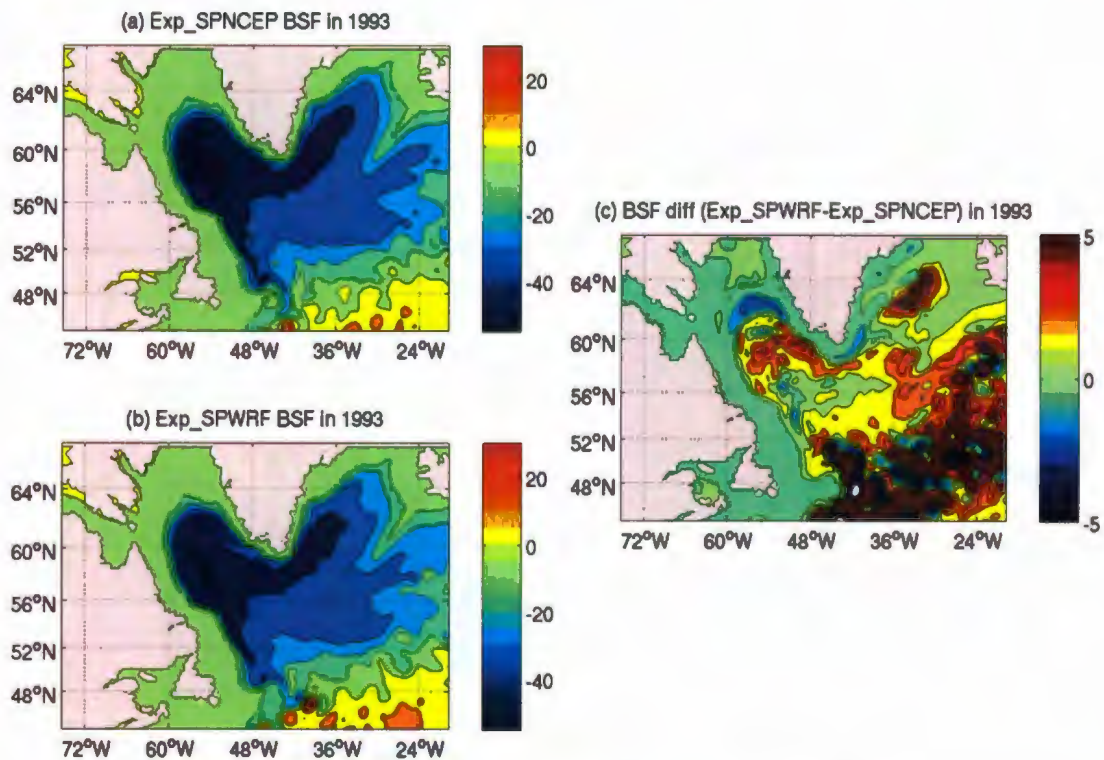


Figure 5.8 Barotropic stream function ( $S_v$ ) in 1993.

((a) is from the Exp\_SPNCEP simulation, (b) from the Exp\_SPWRF simulation, and (c) is the difference between the two simulations (Exp\_SPWRF-Exp\_SPNCEP)).

The improvements of the Exp\_SPWRF simulation of the subpolar North Atlantic are also seen in sea surface temperature (Figure 5.7) and barotropic stream function in 1993 (Figure 5.8). In 1993, sea surface temperature from the Exp\_SPWRF simulation is colder in the Labrador Sea and the Irminger Sea than the Exp\_SPNCEP result. The barotropic stream function is larger in the Exp\_SPWRF simulation, which indicates a weak subpolar gyre in this year.

The interannual variability of potential temperature and salinity in the central

Labrador Sea (Figure 5.5) also displays some differences between the Exp\_SPWRF and Exp\_SPNCEP simulations, although the overall trends of the interannual variability of potential temperature and salinity in the two simulations are similar. Sea water in the upper layer becomes colder and fresher in 1983 and 1993-1993 and warmer and saltier between 1984-1992 and after 1995. However, in the deep convection periods 1983 and 1993-1994, the differences are evident. During 1983 and 1993-1994, the Exp\_SPNCEP potential temperature was 0.1 - 0.2 °C warmer than the Exp\_SPWRF one and the Exp\_SPNCEP salinity is 0.01 saltier than the Exp\_SPWRF one. Hence, the Exp\_SPWRF simulation is closer to the observation (Yashayaev, 2007). We can also conclude that the bias in the new simulation is reduced by about 40-50% with respect to the Exp\_SPNCEP simulation.

The two experiments (Exp\_SPNCEP and Exp\_SPWRF) represent the declining trend in the circulation known from the observations (Häkkinen et al., 2008; Häkkinen and Rhines, 2004). There still exist some discrepancies between the two simulations. For example, the subpolar gyre in the Exp\_SPWRF simulation is weaker than that in the Exp\_SPNCEP simulation in 1993. This is consistent with the sign on Figure 5.8 (c). The maximum transports in the two simulations both are in 1995 and 1985, which are two years after the deep convection events in 1993 and 1983, respectively. In addition, the Exp\_SPWRF transport in 1995 is slightly stronger than the Exp\_SPNCEP results. The BSF differences between years with maximum (1995) and minimum (1999) transports of each result are shown in Figure 5.9. The Exp\_SPWRF transport difference displays about 3-4 Sv stronger than the Exp\_SPNCEP result in the Labrador and Irminger Sea. This analysis indicates that the Exp\_SPWRF simulation slightly strengthens the interannual

variability in the subpolar gyre transport. The major cause of the differences between the two runs produced with the same initial conditions, topography and lateral boundary conditions is the difference in the surface forcing. Here we study the characteristics of these differences.

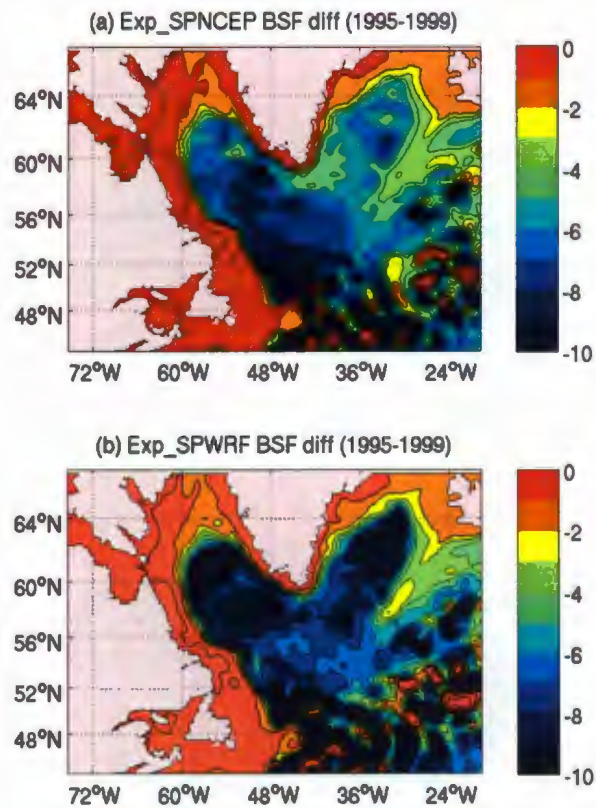


Figure 5.9 Yearly barotropic stream function (Sv) difference between 1995 and 1999.

The dominant EOFs of winter-averaged net downward heat flux are calculated and analyzed as follows. The spatial pattern and temporal variation of the two leading modes are shown in Figure 5.10-5.11. The importance of each mode is presented in Table 5.1.

The first EOF of the heat flux in the two experiments (Figure 5.10a, b) both account for over 50% of the total variance. A negative area only appears over the southern Davis Strait and a large positive area exists in the rest of the region with its center over the central Labrador Sea in both results. In the Exp\_SPWRF result, the contrast between the two centres is much stronger than in the Exp\_SPNCEP simulation. The time variability of the first EOF in the two experiments (Figure 5.10d) is similar.

Diagnostic	EOF1 (%)		EOF2 (%)	
	Exp_SPNCEP	Exp_SPWRF	Exp_SPNCEP	Exp_SPWRF
Net downward heat flux*	53.01	51.30	15.11	19.09

Table 5.1 Variances of the first and second EOF spatial patterns of oceanic fields averaged in winter months (JFM) during the 26 years from the old and new experiments. \*(positive net downward heat flux means warm surface temperature and the ocean gains heat; negative means cold surface temperature and the ocean loses heat)

The second leading modes of the two heat flux account for 15.11% and 19.09% of their total variance, respectively. The EOF2 of the heat fluxes in the two experiments (Figure 5.11a, b) defines a pattern with three areas of extreme values: a positive area in the Labrador Sea surrounded by two negative areas over the southern Davis Strait and the rest of the northern Atlantic. The Exp\_SPWRF EOF2 has stronger positive center near the west coast of Greenland and also stronger negative centers over the southern Davis Strait and the western Denmark Strait than the Exp\_SPNCEP EOF2. The temporal variations

associated with this EOF mode (Figure 5.11d) fluctuate in the similar frequency of both results.

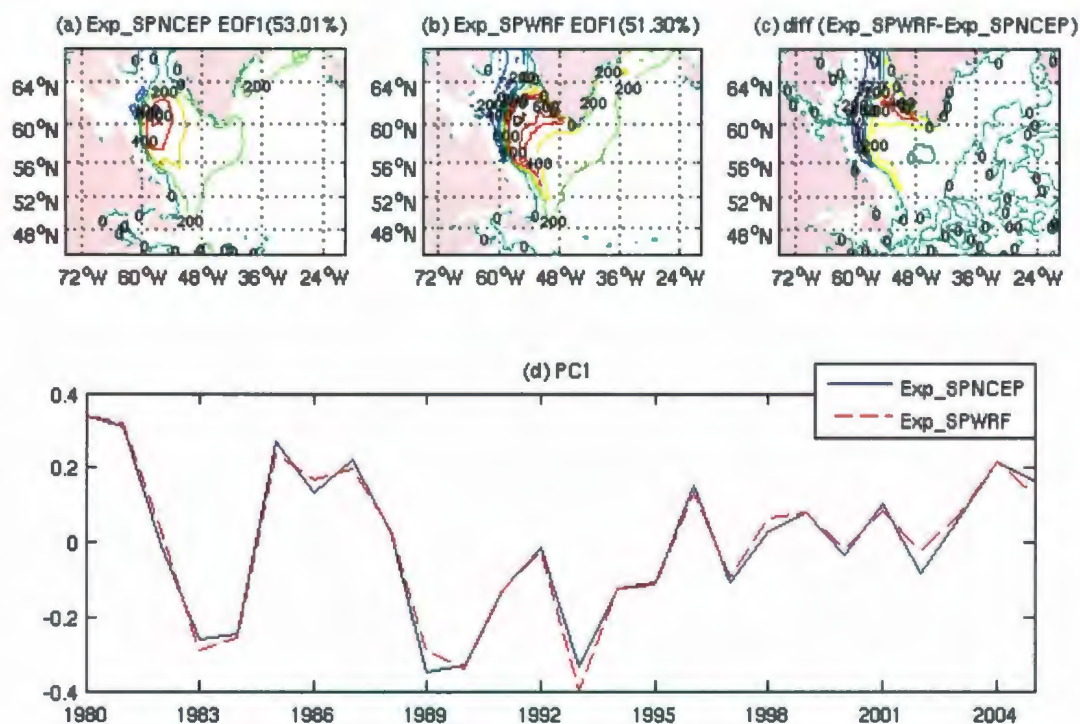


Figure 5.10 The first EOF mode of net downward heat flux averaged in winter month (JFM) during the 26 years from the results of the Exp\_SPNCEP and the EXP\_SPWRF experiments.

The comparison of the first two dominant modes of surface heat flux variability show similar spatial patterns and temporal variability. The major difference is the strong contrast between the maximum and minimum centers in the EOFs in the Labrador Sea. This stronger contrast is related to stronger cooling when the EOFs coefficients are negative in the Exp\_SPWRF simulation.

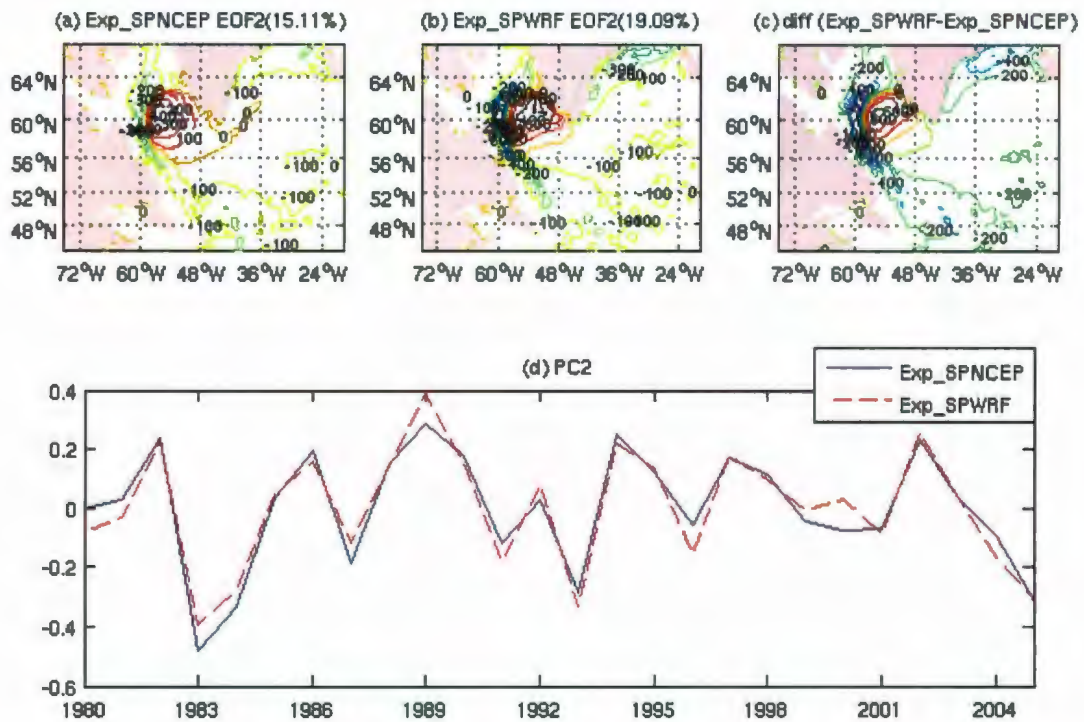


Figure 5.11 The second EOF mode of net downward heat flux averaged in winter month (JFM) during the 26 years from the results of the Exp\_SPNCEP and the Exp\_SPWRF experiments.

### 5.3 Discussion

The interannual variability of the subpolar North Atlantic Ocean is presented in the ocean simulations. Through the comparisons with the observations, the ocean simulation forced with the fine-resolution WRF-derived data (i.e. Exp\_SPWRF) is closer than the simulation forced with NCEP/NCAR reanalysis data (i.e. Exp\_SPNCEP). The Exp\_SPWRF simulation shows the reduced bias in potential temperature and salinity from surface to the mixed layer in the central Labrador Sea, especially during the deep

convection events. Mixed layer depth is deeper and sea surface temperature is colder in the Labrador Sea and the Irminger Sea, and the subpolar gyre is weaker in the Exp\_SPWRF simulation during the deep convection event in 1993. These improvements are arising from the stronger heat flux loss in the central Labrador Sea in the Exp\_SPWRF run.

## **Chapter 6: Conclusion**

### **6.1 Major findings**

The major findings and outcomes of this study are summarized.

- The WRF model version 3.1.1 is a useful and valid tool for downscaling the NCEP/NCAR reanalysis data over the subpolar North Atlantic.
- The fine-resolution atmospheric data derived by the WRF model captures the large-scale pattern and inter-annual variability of the NCEP/NCAR reanalysis data and also properly resolve the orographic effects of Greenland.
- Through the comparative analysis of a robust forward Greenland tip jet in February 2000, the WRF result is closer to the QuikSCAT observations in propagating velocity, peak wind speeds and high wind areas than the NCEP data. The study of the evolution processes of the tip jets shows the WRF results present more detailed and physical structures than the NCEP data and thus more realistic.
- The ocean simulation forced with the fine-resolution WRF atmospheric fields over the subpolar North Atlantic realistically represents the deep convection events in the Labrador Sea in 1983 and 1993-1994. It also represents the main elements of the inter-annual variability of potential temperature and salinity in the central Labrador Sea and subpolar gyre and improves the ocean simulation with respect to the same model forced with the coarse-resolution NCEP/NCAR reanalysis data.

## **6.2 Future work**

This study utilizes a fine-resolution atmospheric model which is suitable for regional downscaling. The future work will include following ideas:

- Detailed studies of Greenland tip jets
- Development of a coupled atmospheric-ocean model
- Study of regional climate of the subpolar North Atlantic Ocean

## References

- Adcroft, A., C. Hill, and J. Marshall, 1997: Representation of topography by shaved cells in a height coordinate ocean model. *Mon. Wea. Rev.*, **125**, 2293–2315.
- Angell, J. K. and J. Korshover, 1974: Quasi-biennial and long-term fluctuations in centers of action. *Mon. Wea. Rev.*, **102**, 669–678.
- Antonov, J. I., R. A. Locarnini, T. P. Boyer, A. V. Mishonov, and H. E. Garcia, 2006: World Ocean Atlas 2005, Volume 2: Salinity. S. Levitus, Ed. NOAA Atlas NESDIS 62, U.S. Government Printing Office, Washington, D.C., 182 pp.
- Arakawa A., V. R. Lamb, 1981: A potential enstrophy and energy conserving scheme for the shallow water equations. *Mon. Wea. Rev.*, **109**, 18–36.
- ARW version 3 modeling system User's Guide, July 2009, Mesoscale & Microscale Meteorology Division and National Center for Atmospheric Research, derived from [http://www.mmm.ucar.edu/wrf/users/docs/user\\_guide\\_V3/contents.html](http://www.mmm.ucar.edu/wrf/users/docs/user_guide_V3/contents.html).
- Asselin, R., 1972: Frequency filter for time integrations. *Mon. Wea. Rev.*, **100**(6), 487–490.
- Barnier, B., and coauthors, 2006: Impact of partial steps and momentum advection schemes in a global ocean circulation model at eddy-permitting resolution. *Ocean Dyn.*, doi:10.1007/s10236-006-0082-1.
- Beljaars, A. C. M., 1994: The parameterization of surface fluxes in large-scale models under free convection. *Quart. J. Roy. Meteor. Soc.*, **121**, 255–270.

- Blanke, B. and P. Delecluse, 1993: Low frequency variability of the tropical Atlantic Ocean simulated by a general circulation model with mixed layer physics. *J. Phys. Oceanogr.*, **23**, 1363–1388.
- Bower, A. S., M. S. Lozier, S. F. Gary, and C. W. Böning, 2009: Interior Pathways of the North Atlantic meridional overturning circulation. *Nature*, **459**, doi:10.1038/nature07979.
- Brankart, J. M., and P. Brasseur, 1998: The general circulation in the Mediterranean Sea: A climatological approach. *J. Mar. Syst.*, **18**, 41– 70.
- Carton, J. A., B. S. Giese, and S. A. Grodsky, 2005: Sea level rise and the warming of the oceans in the SODA ocean reanalysis. *J. Geophys. Res.*, **110**, doi: 10.1029/2004JC002817.
- Chen, F., and J. Dudhia, 2001: Coupling an advanced land-surface/ hydrology model with the Penn State/ NCAR MM5 modeling system. Part I: Model description and implementation. *Mon. Wea. Rev.*, **129**, 569–585.
- Dickson, B., I. Yashayaev, J. Meincke, B. Turrell, S. Dye, and J. Holfort, 2002: Rapid freshening of the deep North Atlantic over the past four decades. *Nature*, **416**, 832-837.
- Diez, E., C. Primo, J. A. Garcia-moya, J. M. Gutierrez, and B. Orfila, 2005: Statistical and dynamical downscaling of precipitation over Spain from DEMETER seasonal forecasts. *Tellus*, **57A**, 409-423.
- Doyle, J.D. and M.A. Shapiro, 1999: Flow response to large-scale topography: The Greenland tip jet. *Tellus*, **51A**, 728-748.

- Dudhia, J., 1989: Numerical study of convection observed during the winter monsoon experiment using a mesoscale two-dimensional model, *J. Atmos. Sci.*, **46**, 3077–3107.
- Dyer, A. J., and B. B. Hicks, 1970: Flux-gradient relationships in the constant flux layer. *Quart. J. Roy. Meteor. Soc.*, **96**, 715-721.
- Fichefet, T., and M. A. Morales Maqueda, 1997: Sensitivity of a global sea ice model to the treatment of ice thermodynamics and dynamics. *J. Geophys. Res.*, **102**, 12,609-12,646.
- Gaspar, P., Y. Grégoris, and J. M. Lefevre, 1990: A simple eddy kinetic energy model for simulations of the oceanic vertical mixing Tests at station papa and long-term upper ocean study site. *J. Geophys. Res.*, **95**: 16179-16193.
- Giorgi, F., B. Hewitson, J. Christensen, M. Hulme, H. Von Storch, and co-authors, 2001: Regional climate information-evaluation and projections. In: *Climate Change 2001: The scientific basis, Contribution of Working Group I to the Third Assessment Report of the Intergovernment Panel on Climate Chang (IPCC)* [J. T. Houghton, Y. Ding, D. J. Griggs, M. Noguer, P. J. van der Linden, and D. Xiaoxu (eds.)]. Chapter 10, Cambridge University Press, Cambridge, 583-638
- Häkkinen, S. and P. Rhines, 2004: Decline of the North Atlantic subpolar circulation in the 1990s. *Science*, **304**, 555-559.
- Häkkinen, S., H. Hatun, and P. Rhines, 2008: Satellite evidence of change in the Northern Gyre, In: R. R. Dickson, J. Meincke and P. Rhines Eds., *The subarctic seas as source of Arctic change*, Springer, 551-568.

- Haine, T. W. N., S. Zhang, G. W. K. Moore, and I. A. Renfrew, 2009: On the impact of high-resolution, high-frequency meteorological forcing on Denmark-Strait ocean circulation. *Quart. J. Roy. Meteor. Soc.*, **135**, 2067-2085.
- Halldor, B. and S. A. Venegas, 1997: A manual for EOF and SVD analyses of climate data. McGill University, *CCGCR Report No. 97-1*, Montréal, Québec, 52pp
- Hong, S. Y., J. Dudhia, and S. H. Chen, 2004: A Revised Approach to Ice Microphysical Processes for the Bulk Parameterization of Clouds and Precipitation. *Mon. Wea. Rev.*, **132**, 103-120.
- Hong, S. Y., and Y. Noh, and J. Dudhia, 2006: A new vertical diffusion package with an explicit treatment of entrainment processes. *Mon. Wea. Rev.*, **134**, 2318-2341.
- Hurrell, J. W., 1995: Decadal trends in the North Atlantic oscillation: Regional temperatures and precipitation. *Science*, **269**, 676-679.
- Hurrell, J.W., Y. Kushnir, G. Ottersen, and M. Visbeck Eds, 2003: *The North Atlantic Oscillation Climate Significance and Environmental Impacts*, Geophysical Monograph Series, **134**, 279 pp.
- Kain, J. S., and J. M. Fritsch, 1990: A one-dimensional entraining/ detraining plume model and its application in convective parameterization. *J. Atmos. Sci.*, **47**, 2784-2802.
- Kain, J. S., and J. M. Fritsch, 1993: Convective parameterization for mesoscale models: The Kain-Fritsch scheme. The representation of cumulus convection in numerical models, K. A. Emanuel and D.J. Raymond, Eds., *Amer. Meteor. Soc.*, 246 pp.
- Kalnay, E., M. Kanamitsu, R. Kistler, W. Collins, D. Deaven, L. Gandin, M. Iredell, S. Saha, G. White, J. Woollen, Y. Zhu, M. Chelliah, W. Ebisuzaki, W. Higgins, J.

- Janowiak, K. C. Mo, C. Ropelewski, J. Wang, A. Leetmaa, R. Reynolds, Roy Jenne, and Dennis Joseph, 1996: The NCEP/NCAR 40-Year Reanalysis Project. *Bulletin of the Amer. Meteor. Soc.*, **77**(3), 437-472.
- Lavender, K., R. E. Davis and W. B. Owens, 2000: Mid-depth recirculation observed in the interior Labrador and Irminger seas by direct velocity measurements. *Nature*, **407**, 66-69.
- Locarnini, R. A., A. V. Mishonov, J. I. Antonov, T. P. Boyer, and H. E. Garcia, 2006: World Ocean Atlas 2005, Volume 1: Temperature. S. Levitus, Ed. NOAA Atlas NESDIS 61, U.S. Government Printing Office, Washington, D.C., 182 pp.
- Lohmann, K., H. Drange, and M. Bentsen, 2009: A possible mechanism for the strong weakening of the North Atlantic subpolar gyre in the mid-1990s. *Geophys. Res. Lett.*, **36**, L15602, doi: 10.1029/2009GL039166.
- Madec G. 2008: "NEMO ocean engine". Note du Pole de modélisation, Institut Pierre-Simon Laplace (IPSL), France, No 27 ISSN No 1288-1619.
- Marchesiello, P., J. M. Williams, and A. Shchepetkin, 2001: Open boundary conditions for long-term integrations of regional oceanic models. *Ocean Modelling*, **3**, 1-20.
- Marshall, J., and F. Schott, 1999: Open-ocean convection: Observations, theory, and models. *Rev. Geophys.*, **37**, 1-64.
- Martin, Revekah and G. W. K. Moore, 2007: Air-sea interaction associated with a Greenland reverse tip jet. *Geophys. Res. Lett.*, **34**, L24802, doi: 10.1029/2007GL031093.
- McCartney, M. S., 1992: Recirculating components to the deep boundary current of the northern North Atlantic. *Prog. Oceanogr.*, **29**, 283-383.

- Mlawer, E. J., S. J. Taubman, P. D. Brown, M. J. Iacono, and S. A. Clough, 1997: Radiative transfer for inhomogeneous atmosphere: RRTM, a validated correlated-k model for the longwave. *J. Geophys. Res.*, **102** (D14), 16663–16682.
- Moore, G. W. K., 2003: Gale force winds over the Irminger Sea to the east of Cape Farewell, Greenland. *Geophys. Res. Lett.*, **30**(17), 1894, doi: 10.1029/2003GL018012.
- Moore, G. W. K., and I. A. Renfrew, 2005: Tip jets and barrier winds: A Quik-SCAT climatology of high wind speed events around Greenland. *J. Clim.*, **18**, 3713-3725.
- Nahed, F., 2007: Dominant patterns of interannual variability in the North Atlantic. Master's thesis, Memorial University of Newfoundland, 109pp.
- Ohigashi, Tadayasu and G. W. K. Moore, 2009: Fine structure of a Greenland reverse tip jet: a numerical simulation. *Tellus*, **61A**, 512-526.
- Paulson, C. A., 1970: The mathematical representation of wind speed and temperature profiles in the unstable atmospheric surface layer. *J. Appl. Meteor.*, **9**, 857-861.
- Penduff, T., J. Le Sommer, B. Barnier, A. M. Tréguier, J. M. Molines, and G. Madec, 2007: Influence of numerical schemes on current-topography interactions in 1/4° global ocean simulations. *Ocean Sci.*, **3**: 509-524.
- Petersen, G. N., H. Olafsson, and J. E. Kristjansson, 2003: Flow in the lee of idealized mountains and Greenland. *J. Atmos. Sci.*, **60**, 2183-2195.
- Pickart, Robert S., Michael A. Spall, Mads Hvid Ribergaard, G. W. K. Moore and Ralph F. Milliff, 2003: Deep convection in the Irminger Sea forced by the Greenland tip jet. *Nature*, **424**, 152-156.
- Rhein, M., 2000: Oceanography: Drifters reveal deep circulation. *Nature*, **407**, 30-31.

- Robert, A. J., 1966: The integration of a low order spectral form of the primitive meteorological equations. *J. Meteo. Soc. Japan*, **44**, 237-245.
- Serreze, Mark C., F. Carse, R. G. Barry, and J. C. Rogers, 1997: Icelandic low cyclone activity: Climatological features, linkages with the NAO, and relationships with recent changes in the Northern Hemisphere circulation. *J. Clim.*, **10**, 453-464.
- Skamarock, W.C., et al., 2008: A description of the advanced research WRF version 3. NCAR technical note, NCAR/TN-475+STR.
- Talley, L. D., and M. S. McCartney, 1982: Distribution and circulation of Labrador Sea Water. *J. Phys. Oceanogr.*, **12**, 1189-1205.
- Thompson, K. R., D. G. Wright, Y. Lu, and E. Demirov, 2006: A simple method for reducing seasonal bias and drift in eddy resolving ocean models. *Ocean Modelling*, **14**, 122-138.
- Tréguier, A., B. Barnier, A. de Miranda, J. Molines, N. Grima, M. Imbard, G. Madec, C. Messenger, T. Reynaud, and S. Michel, 2001: An eddy permitting model of the atlantic circulation: evaluating open boundary conditions. *J. Geophys. Res.*, **106**: 22115- 22129.
- Vage, Kjetil, T. Spengler, H. C. Davies and R. S. Pickart, 2009: Multi-event analysis of the westerly Greenland tip jet based upon 45 winters in ERA-40. *Quart. J. Roy. Meteor. Soc.*, doi: 10.1002/qj.488.
- Von Storch, H. 1995, Inconsistencies at the interface of climate impact studies and global climate research. *Meteor. Z.*, **4**, 72-80.

- Walker, G. T., 1924: Correlations in seasonal variations of weather IX, *Memoris India: Meteorology Department*, **24**: 687-692.
- Walker, G. T. and E. W. Bliss, 1932: World Weather V, *Mem. Roy. Meteorol. Soc.*, **4**, 53-84.
- Webb, E. K., 1970: Profile relationships: The log-linear range, and extension to strong stability. *Quart. J. Roy. Meteor. Soc.*, **96**, 67-90.
- Worthington, L. V., 1976: On the North Atlantic circulation, 6, The Johns Hopkins Oceanographic Studies, The Johns Hopkins University Press, Baltimore, MD, 110 pp.
- Wüst, G., 1935: Aschichtung und Zirkulation des Atlantischen Ozeans, Vol. 6:1st Part, Engl. Transl., in W. J. Emery (ed.), *The Stratosphere of the Atlantic Ocean*, Amerind, New Delhi, 1978, 112 pp.
- Yashayaev, Igor, 2007: Hydrographic changes in the Labrador Sea, 1960-2005. *Prog. Oceanogr.*, **73**: 242-276.
- Zhu, J and E. Demirov, 2010: On the mechanism of interannual variability of the Irminger Water in the Labrador Sea. *J. Geophys. Res.* (accepted after minor revision).





